Radiation from relativistic particles accelerated at shear layers in relativistic jets

TB Chand

orcid.org 0000-0002-1833-3749

Thesis accepted in fulfillment of the requirements for the degree *Doctor of Philosophy* in Space Physics at the North-West University

Promoter: Prof M Böttcher

To my beloved parents, Krit and Jaimati, my dear wife, Dipa, and my precious son, Dakshit, this work is lovingly dedicated

Acknowledgements

This thesis not only reflects the scientific endeavors undertaken throughout my Ph.D. journey but also serves as a testament to the life lessons and experiences that have deeply enriched my personal growth. I am profoundly grateful to all individuals, both acknowledged here and those unmentioned, whose guidance, support, and impactful moments have left an indelible mark on my journey.

First and foremost, I extend my deepest gratitude to my supervisor, Prof. Markus Böttcher, whose unwavering dedication, patience, and steadfast support have been instrumental in every step of my Ph.D. journey. I am particularly grateful for his prompt responsiveness to my queries and his compassionate nature. Throughout my Ph.D., he provided me with unparalleled freedom, fostering an environment conducive to developing my research skills and effective learning. From offering invaluable guidance during challenging situations to his unwavering encouragement during moments of doubt, his support has been truly remarkable. Working under his mentorship has profoundly shaped my professional trajectory, for which I am deeply thankful.

I extend my gratitude to Dr. Patrik Kilian for his invaluable assistance during the initial stages of my Ph.D. journey. As my assistant supervisor for a couple of years, he played a crucial role in guiding me through the learning process of the Particle-in-Cell (PiC) Simulation code and providing access to the PiC code (ACRONYM). I would also like to express my profound gratitude to Prof. Anatoly Spitkovsky for our initial discussions regarding the incorporation of shear-driven particle acceleration into the TRISTAN-MP code, a pivotal aspect of my Ph.D. research.

I would also like to seize this opportunity to extend my gratitude to the staff of CSR, with special thanks to Prof. Stefan Ferreira and Prof. Christo Venter, former directors of the CSR, as well as to Prof. Amare Abebe, the current CSR director. Additionally, I am deeply appreciative of the assistance provided by Ms. Petro Sieberhagen, Ms. Elanie Van Rooyen, Ms. Lee-Ann Van Wyk, and Mr. Lendl Fransman. Their efficient management of administrative tasks has been invaluable and greatly appreciated.

Without a doubt, I owe a debt of gratitude to my dear friend and former office mate, Dr. Hassan Abdalla. His unwavering inspiration and encouragement propelled me forward during moments of doubt and despair in my research endeavors. I would also like to

express my sincere gratitude to my friends and former colleagues, Dr. Sunil Chandra, Dr. Michael Zacharias, and Dr. Zorawar Wadiasingh, for engaging in enriching discussions on a wide range of topics, both academic and non-academic. I am grateful to my supportive friends in South Africa, including Dr. Sreejith P. Babu, Dr. Rukaiya Khatoon, Dr. Anu Kundu, Dr. Pranju Goswami, Dr. Anton Dmytriiev, Dr. Ephrem Tesfaye, and others not mentioned here, for organizing gatherings and providing a stress-free environment during challenging times. Their friendship and camaraderie helped alleviate the pressures of academic life. Additionally, I fondly remember the delightful braai gatherings hosted by my supervisor at his home, which brought together colleagues from our department in a warm and inviting atmosphere. I also recall the movie nights organized within our department, which contributed to a pleasant atmosphere that I will always cherish.

Words cannot adequately convey the depth of my gratitude to my beloved parents for their unwavering support and blessings throughout my journey. I am profoundly thankful to my siblings, Meena, Dropati, Prakash, Parwati, and Mahesh, for their constant affection and unwavering love, which have served as pillars of strength regardless of life's twists and turns. Last but certainly not least, I wish to extend my heartfelt appreciation to my beloved wife, Dipa, whose unwavering support has been my anchor throughout my Ph.D. journey, especially during the most challenging moments. Her empathy, affection, and encouragement have consistently propelled me forward. With boundless love and gratitude, I want to express my deepest appreciation to my cherished son, Dakshit. His radiant presence has illuminated my path, offering solace and joy during the most demanding stretches of my Ph.D. journey.

Abstract

Relativistic jets, highly collimated and high-velocity outflows of particles and electromagnetic radiation, are a common phenomenon associated with various astrophysical objects including stellar-mass compact objects such as white dwarfs, neutron stars, and black holes, as well as supermassive black holes residing in the centers of active galaxies. Relativistic jets have been observed to propagate over immense distances, ranging from parsecs to kiloparsecs, while maintaining their momentum and kinetic energy. Despite extensive ongoing research, several unsolved problems persist in the study of relativistic jets. These include comprehending the processes of jet formation, collimation, particle acceleration, long-range stability, interactions with the surrounding environment, and complex radiative mechanisms. Mechanisms such as Fermi-type acceleration, magnetic reconnection, and plasma instabilities have been proposed to explain particle acceleration within relativistic jets. These mechanisms involve the interaction of particles with magnetic fields, resulting in the transfer of energy and acceleration to relativistic speeds. Blazars, a type of Active Galactic Nuclei (AGNs), exhibit distinctive Spectral Energy Distributions (SEDs) consisting of two broad, non-thermal components. The lower energy bump originates from synchrotron emission by relativistic leptons and extends from radio to optical/UV or X-rays in the case of High-frequency-peaked BL Lacs (HBLs). In leptonic models, the higher energy bump is attributed to inverse Compton scattering, where the same leptons scatter synchrotron or external photons.

Empirical observations and theoretical analyses, incorporating Magneto-hydrodynamic (MHD) simulations, substantiate the presence of radial stratification within jets emitted from AGNs. This stratification manifests as an inner spine, characterized by high velocities, encompassed by an outer sheath with comparably slower motion. The interface between these distinct regions engenders SBLs, resulting from the velocity shear and disparate hydrodynamic characteristics observed between the spine and sheath. Those SBLs within jets from AGNs and GRBs hold promising prospects as sites for relativistic particle acceleration.

This thesis centers on investigating the acceleration mechanism and radiation output from relativistic particles that are accelerated within SBLs present in relativistic jets originating from AGNs and GRBs. Particle-in-Cell (PiC) simulations were employed to investigate the self-generation of electric and magnetic fields, as well as particle acceleration within the SBLs of relativistic jets. The influence of inverse Compton cooling on relativistic par-

ticles accelerated in SBLs is examined, incorporating the self-consistent calculation of the radiation spectrum resulting from inverse Compton scattering of relativistic electrons with an isotropic external soft photon field. Notably, the Compton emission produced exhibits high anisotropy, displaying stronger beaming along the direction of the jet compared to the anticipated $1/\Gamma$ pattern that arises from intrinsically isotropic emission within the comoving frame of an emission region moving along the jet with a bulk Lorentz factor Γ. These findings offer a potential resolution to the long-standing problem known as the Doppler Factor Crisis.

Keywords: Supermassive black holes; active galactic nuclei; relativistic jets; particle-in-cell simulations; relativistic shear boundary layers; relativistic particle acceleration; radiative processes:inverse Compton cooling

Contents

List of Figures

List of Tables

List of Abbreviations

AGNs Active Galactic Nuclei. v, x, 1, 2, 5, 6, 8, 27

CMB Cosmic Microwave Background. 70

CPS Cells Per Skin depth. 51

DSA Diffusive Shock Acceleration. 2

EC External Compton. 70

ECCI electron counter-current instability. 63

ELF Equal Lorentz factor Frame of reference. 49, 59

ERF Electron Rest Frame. 34

GRBs Gamma-ray Bursts. v, 1, 2, 5, 27

GRMHD General Relativistic Magnetohydrodynamic. 13

HBLs High-frequency-peaked BL Lacs. v

IC Inverse Compton. 3, 4

KHI Kelvin-Helmholtz Instability. 3

LF Laboratory Frame. 36

LTE local thermodynamic equilibrium. 29

MHD Magneto-hydrodynamic. v, 44

NCI Numerical Cerenkov Instability. 52

PiC Particle-in-Cell. v, 2–4, 44

PPC Particles Per Cell. 51

PQS Piecewise Quadratic Spline. 53

RMHD Relativistic Magneto-hydrodynamic. 2

SBLs Shear Boundary Layers. v, vi, 2–4

SEDs Spectral Energy Distributions. v

SNRs Supernova Remnants. 5, 44

SSC Synchrotron Self-Compton. 70

TRISTAN-MP TRIdimensional STANford - Massively Parallel. 54

UV Ultra Violet. 1

VHE Very High Energy. 5

VLBI Very Long Baseline Interferometry. x, 9, 10

Chapter 1

Introduction

1.1 Overview and Motivation

The primary focus of this thesis is to investigate the radiation emitted by relativistic particles that are accelerated within shear layers present in relativistic jets. Relativistic jets are astrophysical phenomena characterized by collimated outflows of particles and radiation propelled at velocities close to the speed of light. These jets are commonly observed in various astrophysical sources, including Active Galactic Nuclei (AGNs) and Gamma-ray Bursts (GRBs) (e.g., Blandford et al., 2019). Revealing the underlying composition of relativistic jets observed in AGNs and GRBs remains a fundamental challenge in gamma-ray astronomy. These jets, studied using advanced telescopes like the Fermi Gamma-Ray Space Telescope and Atmospheric Cherenkov Telescopes (e.g., H.E.S.S., MAGIC, and VERITAS), are also a subject of interest for the future Cherenkov Telescope Array. For a comprehensive overview of our current knowledge and uncertainties regarding relativistic jets, both in the context of key model components for Galactic and extragalactic jet sources and with a focus on AGNs (particularly blazars) and microquasars, refer to a recent review article by Romero et al. (2017). A key focus is to understand the mechanisms responsible for accelerating particles to ultrarelativistic energies within these powerful jets and the radiative processes associated with them. The investigation of relativistic jets in AGNs finds its most direct insights through observations of blazars. Blazars are AGNs whose jets are oriented at a small angle relative to our line of sight. Their broadband nonthermal continuum emission is composed of two broad emission components (e.g., Böttcher, 2007), likely originating from small, localized regions within the relativistic jet. A widely accepted explanation for the radio through optical/UV (and sometimes X-ray) emission from blazars is synchrotron radiation produced by relativistic particles. Addressing the high-energy emission of blazars, leptonic models propose that the X-rays and gamma-rays originate from Compton upscattering of lower-energy photons by the same relativistic electrons (e.g., Böttcher, 2007).

Several acceleration mechanisms have been proposed to account for the energization of

particles to ultrarelativistic energies in relativistic jets from AGNs and GRBs. The most prevalent acceleration mechanisms are magnetic reconnection (see e.g., Zenitani and Hoshino, 2001; Drake et al., 2006; Cerutti et al., 2012; Sironi, 2022) and Diffusive Shock Acceleration (DSA) (e.g., Micono et al., 1999; Baring et al., 2016; Cerutti and Giacinti, 2023). Relativistic magnetic reconnection becomes significant when the magnetic energy density surpasses the plasma rest mass energy density, leading to rearrangements in magnetic topology thereby releasing a considerable amount of magnetic energy. This non-thermal particle acceleration mechanism has been extensively investigated using the Particle-in-Cell (PiC) method (e.g., Sironi and Spitkovsky, 2014; Werner et al., 2018a). Fermi acceleration operates based on the shock jump conditions observed at relativistic shocks (e.g., Gallant, 2002). DSA is the favored mechanism for cosmic ray production that occurs in astrophysical shocks of various scales, from the solar system to supernova remnants, GRBs, and AGNs. DSA accelerates particles by interactions with shock waves and magnetic field perturbations, leading to power-law energy distributions. Simulating DSA is challenging due to its multi-scale nature (e.g., Marcowith et al., 2020).

The first-order Fermi acceleration mechanism is a likely explanation for knotty features observed in extragalactic jets, indicative of strong shock formation. However, recent high-resolution studies suggest that first-order Fermi acceleration alone cannot fully explain extended high-energy emission. Observations of quasar 3C 273 reveal the absence of the expected strong synchrotron cooling process, further highlighting the requirement for a continuous re-acceleration mechanism in relativistic jets (e.g., Jester et al., 2001). Consequently, there is mounting evidence supporting the presence of spine-sheath boundary layers in relativistic jets, characterized by a rapid inner spine enveloped by a slower outer sheath (e.g., Ghisellini et al., 2005). These shear layers in relativistic jets refer to a region where there is a significant velocity difference (shear) between the jet plasma and its surrounding environment. The ensuing Shear Boundary Layers (SBLs) are a promising candidate for particle acceleration and radiation (e.g., Stawarz and Ostrowski, 2002; Sahayanathan, 2009; Liang et al., 2013a; Chand et al., 2019). SBLs form at the interfaces between high-velocity plasma within relativistic jets and their surrounding interstellar environments in various astrophysical scenarios such as AGNs (e.g., Alves et al., 2012; Liang et al., 2013a; Rieger, 2019) and also in the jets involving ultra-relativistic outflows of GRBs (e.g., Piran, 2000).

Particle acceleration in shear flows (e.g., Stawarz and Ostrowski, 2002; Rieger and Duffy, 2006; Webb et al., 2018; Rieger, 2019) occurs as energetic particles scatter off small-scale magnetic field irregularities in the moving background flow. While the direction of particle momentum randomizes in each scattering event, its magnitude remains preserved in the local comoving flow frame (e.g., Rieger and Duffy, 2004). In the presence of shear, the particle's momentum relative to the flow changes, resulting in a potential net momentum increase over time (e.g., Rieger and Duffy, 2006). Recently, Wang et al. (2023) have investigated the self-generation of a sheath during the propagation of a relativistic spine jet into a static cocoon using 3D Relativistic Magneto-hydrodynamic (RMHD) simulations, examining jet properties such as turbulence and potential shear acceleration.

Recent investigations of SBLs employing PiC simulations in the context of relativistic jets have revealed that effective generation of electric and magnetic fields, along with subsequent particle acceleration, can emerge from initially unmagnetized plasma (e.g., Alves et al., 2012; Liang et al., 2013a,b; Rieger, 2019). The self-generated magnetic field arises from plasma instabilities, such as the Kelvin-Helmholtz Instability (KHI) (Chandrasekhar, 1961) and the Weibel instability (Weibel, 1959). The KHI arises from the shear flow between two fluid layers with different velocities, leading to the formation of vortices or waves at their interface. Turbulence emerges as a consequence of the nonlinear evolution of the KHI, which arises from velocity shear. Such shear is inherent in explosive outflows, such as relativistic jets, owing to the intermittent and inhomogeneous nature of both the outflow and its surrounding medium. These turbulent shear flows are commonly characterized by a high degree of ionization, with the turbulent dynamo expected to be instigated by the KHI (e.g., Zhang et al., 2009). Subsequently, this mechanism is anticipated to facilitate the self-generation of magnetic fields within jets. On the other hand, the Weibel instability results from an anisotropic distribution of particle velocities in a plasma, generating magnetic fields perpendicular to a particle beam's direction, causing filamentation (e.g., Weibel, 1959; Liang et al., 2013a; Nishikawa et al., 2014). While the classical KHI, in the hydrodynamic limit, renders the shear interface unstable, the presence of ambient magnetic fields, especially longitudinal B-fields, suppresses this instability (Chandrasekhar, 1961). Consequently, the shear interface within AGN's kpc-scale jets remains stable against the KHI.

Energetic particles can sample velocity disparities while traversing shear flows. Magnetic field irregularities present in different strata of the shear flow scatter these particles, fostering energy gain due to variations in bulk velocity across the shear flow (e.g., Liu et al., 2017). Consequently, this process transforms the kinetic energy of the background flow's bulk motion into nonthermal particle energies. Prior studies have indicated that the efficiency of shear acceleration hinges on the intensity of velocity shear, making shear acceleration more effective in relativistic jets compared to non-relativistic ones (e.g., Webb, 1989; Ostrowski, 1990). High-energy particles accelerated within SBLs along magnetic field lines exhibit an anisotropic momentum distribution, displaying efficient Synchrotron radiation emission (e.g., Liang et al., 2013a). Several investigations employing PiC simulations have explored the impact of synchrotron cooling (e.g., Hakobyan et al., 2019) and Inverse Compton (IC) cooling (e.g., Werner et al., 2018a) on particles in relativistic jets, considering magnetic reconnection and the consequent radiation spectra. Nonetheless, while radiative cooling holds the potential for significant influence on particle dynamics, the role of radiation drag on radiating particles and its implications on radiation spectra largely remain uncharted within studies of particle acceleration at SBLs in jets.

1.2 Thesis at a Quick Glance

In this thesis, our focus is on exploring the acceleration mechanism and radiation characteristics of SBLs within relativistic jets. We provide an in-depth analysis that highlights how SBL turbulence, driven by self-generated electromagnetic fields, plays a pivotal role in generating high-energy particles. Additionally, we conduct comprehensive calculations to determine the radiation spectra, taking into account IC scattering of relativistic electrons. We consider both angle-averaged and angle-dependent soft photon fields, and we investigate the influence of IC cooling on the overall dynamics and energetics of the particles involved.

Chapter 2 offers a comprehensive introduction to the fascinating realm of extragalactic high-energy sources characterized by extreme environments, with a particular focus on the intricate dynamics of relativistic jets. In Chapter 3, we delve into the theoretical underpinnings of the acceleration and radiative mechanisms operative within relativistic jets. We also discuss the theoretical background of an IC scattering of an external blackbody photon field and how we evaluate the radiation spectra. Turning our attention to computational methods, Chapter 4 elaborates on the basics of PiC simulations, encompassing the codes utilized throughout our study. While the `ACRONYM` (Kilian et al., 2012) code set the initial groundwork, our investigation's core findings were predominantly facilitated by the extensive application of the `TRISTAN-MP` (Spitkovsky, 2005) code. Chapter 5 is devoted to presenting our model configuration, with a specific focus on simulating self-generated electric and magnetic fields, while also considering particle anisotropy within the context of SBLs in relativistic jets. Chapter 6 unveils our simulation findings pertaining to the impact of IC cooling on particle spectra and dynamic behaviors. This chapter also highlights the resultant radiation spectra arising from these interactions. Concluding our exploration, Chapter 7 offers comprehensive final reflections and illuminates potential avenues for future inquiries. It is noteworthy that this thesis incorporates results recently published in the Astrophysical Journal (Chand and Böttcher, 2024) and other proceeding papers (Chand et al., 2019; Chand and Böttcher, 2022, 2023).

Chapter 2

Astrophysical Powerhouses: Extragalactic High-Energy Sources

2.1 Overview

Astrophysics represents a branch of science that investigates the physical properties, behaviors, and interactions of celestial objects within the vast expanse of the universe. It utilizes a combination of theoretical models, computational simulations, and observational data to unveil the underlying mechanisms governing the cosmos. One of the most intriguing facets of astrophysics is the study of high-energy astrophysics, which focuses on celestial sources that emit or interact with high-energy radiation. High-energy astrophysics encompasses the investigation of various astrophysical objects such as AGNs, GRBs, microquasars, pulsars, Supernova Remnants (SNRs), etc. These objects offer a window into extreme physical conditions characterized by high temperatures, dense matter, strong magnetic fields, relativistic velocities, and intense gravitational forces. Investigation of these extreme conditions provides valuable insights into fundamental physics, including general relativity, particle acceleration mechanisms, and the behavior of matter and radiation within such extreme regimes.

2.2 Active Galactic Nuclei

AGNs represent highly energetic and compact zones situated at the cores of certain galaxies. These nuclei harbor supermassive black holes, with masses spanning from 10^5 to 10^9 times that of the solar mass ($M_\odot$) (e.g., Alston et al., 2022). They emit electromagnetic radiation across the entire electromagnetic spectrum, spanning from radio frequencies to Very High Energy (VHE) γ-rays ($E_\gamma \geq 100$ GeV), and also release particles from the accretion disk. This entails a range of captivating characteristics, encompassing remarkably high luminosities (reaching up to $L_{bol} \approx 10^{48}$erg s^{-1}), compact emitting regions in the

majority of wavelengths (typically at the milliparsec scale), pronounced evolution of luminosity functions, and broad-band emission spanning the entirety of the electromagnetic spectrum (for an in-depth overview, refer to Padovani (2017)). This powerful outflow is commonly referred to as a **relativistic jet**. Figure 2.1 illustrates an active galactic nucleus, with its central engine emitting the highly powerful relativistic jet. The accretion disk surrounding a supermassive black hole is formed from infalling gas and dust and emits intense radiation as it spirals inward.

AGNs are powered by the accretion of mass onto a supermassive black hole residing in the galactic nucleus (e.g., Fabian, 1999). AGNs exhibit a wide range of emission properties, including the formation of relativistic jets that can extend over vast distances. These jets are collimated outflows of highly energetic particles that are launched perpendicular to the accretion disk. The intense radiation from AGNs is believed to arise from various physical processes associated with the jets, such as the acceleration of charged particles, magnetic field interactions, and the emission from hot plasma surrounding the central black hole. The study of AGNs and their relativistic jets provides valuable insights into the processes of particle acceleration, energy transfer, and the powerful phenomena occurring in the vicinity of supermassive black holes. **Blazars** are subtypes of AGNs characterized by their exceptionally bright and highly variable emission across the entire electromagnetic spectrum, from radio waves to gamma rays. They are distinguished by their relativistic jets that are oriented towards Earth (line of sight), resulting in highly beamed emission (e.g., Blandford et al., 1978; Rees, 1966; Angel and Stockman, 1980; Blandford et al., 2019). The observed emission from blazars is dominated by non-thermal radiation, indicating the presence of high-energy particles and powerful magnetic fields in their jets. Blazars are known for their extreme variability on various timescales, from minutes to years (e.g., Romero et al., 2017), making them fascinating objects for studying the physics of relativistic jets and particle acceleration processes. Illustrated in Figure 2.2, the classification of AGNs through observations centers on a fundamental distinction between radio-quiet and radio-loud categories, with the latter comprising a smaller fraction, around 10%, of the total population. Notably, radio-loud AGNs outshine their radio-quiet counterparts in the radio spectrum by approximately three orders of magnitude. For additional comprehensive insights on AGN classifications, we refer readers to the work by, e.g., Beckmann and Shrader (2012); Dermer and Giebels (2016). In conjunction with active AGNs, a range of celestial sources have been noted for emitting relativistic jets, each presenting distinctive opportunities to unravel fundamental physical mechanisms. Among these sources are GRBs, and microquasars, each of which is briefly outlined below.

Gamma-ray bursts are highly energetic cosmic explosions characterized by the emission of intense bursts of gamma-ray radiation, the most energetic form of electromagnetic radiation. They are classified into two main categories: long-duration GRBs and short-duration GRBs. Long-duration GRBs, typically lasting several seconds to minutes, are associated with the core-collapse of massive stars and the formation of black holes (e.g., Woosley and Bloom, 2006). During the collapse and subsequent supernova explosion, relativistic jets are launched along the rotational axis of the newly formed black hole. These jets,

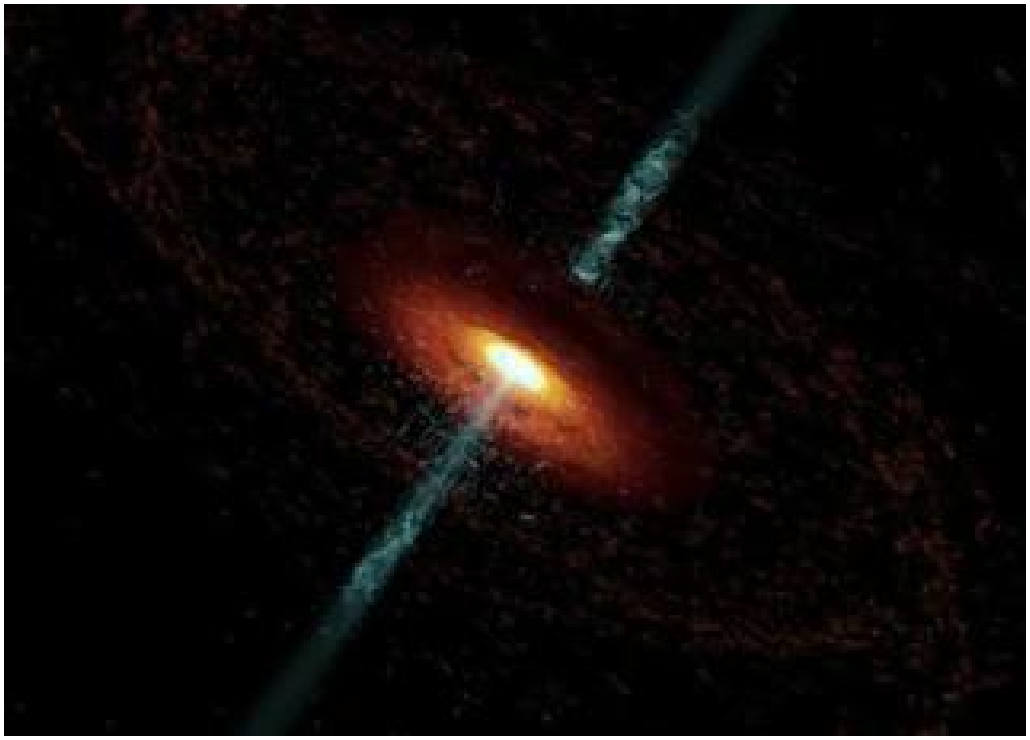

Figure 2.1: Illustration depicting the central region of an active galaxy, near the supermassive black hole. The relativistic jet originates from the accretion disk of the black hole. Image credit: Boston University Blazar Group/Cosmovision.

traveling at speeds close to the speed of light, produce the observed gamma-ray emission. The relativistic motion of the jets gives rise to a beaming effect, concentrating the emitted radiation in a narrow cone aligned with the jet axis. As a result, GRBs can be observed from vast distances despite their brief duration. On the other hand, short-duration GRBs are thought to arise from the merger of compact objects such as neutron stars or black holes (e.g., Abbott et al., 2017). Neutron-star-black-hole mergers are likely to also generate relativistic jets. Recent observations have revealed that the unique characteristics of the nearby GRB060614, such as its duration (102 s) and absence of an accompanying supernova, challenge existing interpretations and suggest a new classification scheme straddling long- and short-duration GRBs (e.g., Gehrels et al., 2006).

Microquasars are compact astrophysical systems with a stellar-mass black hole or neutron star, with masses up to few tens of $M_\odot$ (e.g., Mirabel, 2003), in a binary setup. They actively accrete matter from a companion star, producing relativistic jets. They are scaled-down versions of quasars, short for "quasi-stellar radio sources". Quasars are highly luminous objects at galaxy centers fueled by supermassive black holes, with masses spanning from approximately 10^5 to 10^9 $M_\odot$ (e.g., Shen, 2013). They also generate relativistic jets.

Pulsars are highly magnetized, rapidly rotating neutron stars that emit beams of electromagnetic radiation. These beams are produced as a result of the neutron star's rotation and its strong magnetic field. While pulsars do not typically exhibit relativistic jets, their

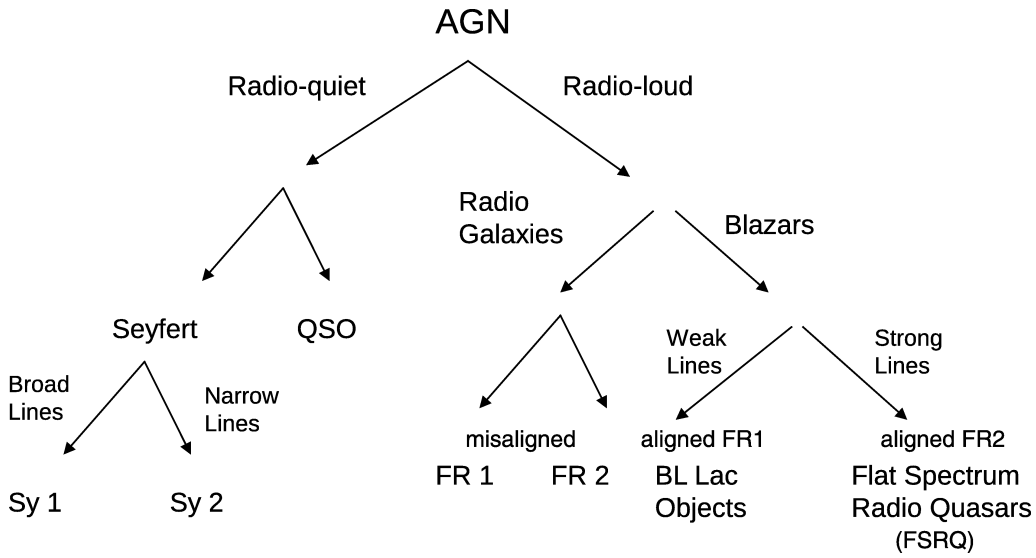

Figure 2.2: Categorization of Active Galactic Nuclei from an observational standpoint: adopted from the work of Dermer and Giebels (2016), this categorization hinges on distinct characteristics, including radio flux intensity and the discernible presence of optical lines within the spectra.

emission processes can involve relativistic effects, such as the beaming of radiation due to the star's rapid rotation and the presence of magnetic fields.

Relativistic jets from AGN, GRBs, and microquasars are pivotal in the study of fundamental physics and the universe. They unveil insights into particle acceleration mechanisms, radiative processes, magnetic field dynamics, and energy dissipation within extreme environments.

2.3 Relativistic Jets in Active Galactic Nuclei

2.3.1 Historical overview

The study of relativistic jets has a long and significant history in astrophysics, with numerous seminal papers proposing and refining the concept (e.g., Fath, 1909; Curtis, 1918; Jansky, 1933; Reber, 1940; Seyfert, 1943; Jennison and Das Gupta, 1953; Baade and Minkowski, 1954; Shklovsky, 1955; Hazard et al., 1963; Blandford and Rees, 1974; Keel, 1983; Blandford et al., 2019). Curtis (1918) made an observation of the galaxy NGC4486 (M87) that would eventually provide an early clue to the existence of relativistic jets. In his analysis of an optical image of the galaxy, Curtis noticed a "curious straight ray" extending from the nucleus of the galaxy. This ray appeared to be connected to the nucleus by a thin line of matter. Notably, the ray exhibited its brightest intensity at its inner end. While he did not have the theoretical framework to fully understand the phenomenon he observed, Curtis's observation was an important milestone in the history of astrophysics, as it helped to spark interest in the study of galaxies and their internal structure. Baade

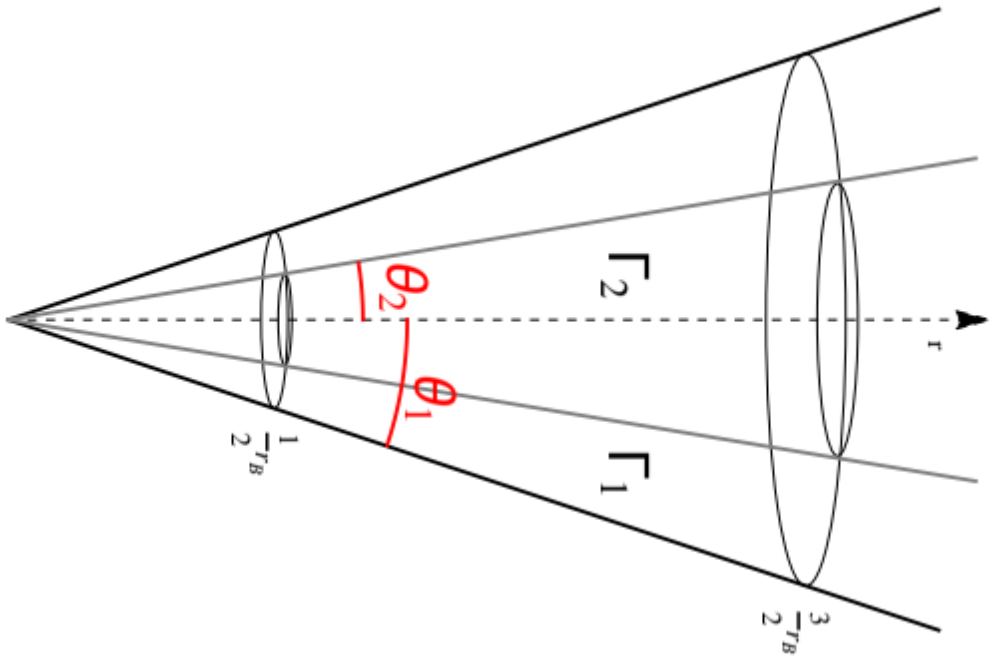

Figure 2.3: Schematic depiction of the spine-sheath structure observed in relativistic jets: These jets originate from the supermassive black hole residing at the centre in active galaxies. The spine exhibits a narrower jet-opening angle (θ_2) and higher bulk Lorentz factor (Γ_2), whereas the outer sheath region extends with a comparably wider jet-opening angle (θ_1) and lower bulk Lorentz factor (Γ_1). Adopted from Sikora et al. (2015).

and Minkowski (1954) proposed the idea of a relativistic jet to explain the elongated radio source observed in the galaxy M87. This was the first proposal of a jet of material moving at relativistic speeds in astrophysics, and the concept has since been extended to a wide variety of sources, including active galactic nuclei, gamma-ray bursts, and microquasars. For a comprehensive exploration of the historical context surrounding AGNs and the emission of jets from these sources, readers are encouraged to delve into the comprehensive and up-to-date reviews authored by, e.g., Romero et al. (2017); Blandford et al. (2019) and citations therein.

2.3.2 Spine-sheath Morphology of Relativistic Jets

The radially stratified configuration of relativistic jets known as the spine-sheath model has caught significant attention, supported by multiple observational evidence (e.g. Junor and Biretta, 1999) and MHD simulations (e.g., Mizuno et al., 2014). In the spine-sheath configuration of jets, a fast-moving inner spine characterized by intense brightness is surrounded by a comparatively slower-moving and fainter sheath region (e.g., Sol et al., 1989; Perlman et al., 2001; Ghisellini et al., 2005; McKinney, 2006; Bruni et al., 2021). Evidence supporting the existence of spine-sheath jets with radial structure is obtained through the observation of limb-brightening in blazar and radio galaxy jets, as revealed by Very Long

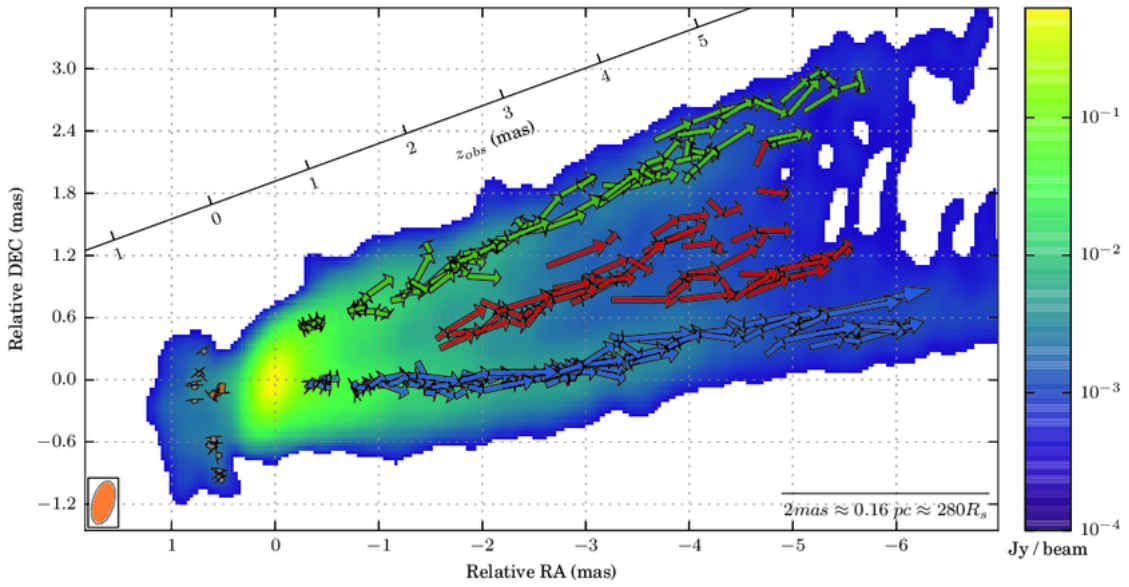

Figure 2.4: Limb-brightened morphology of the M87 jet deduced from the analysis of multi-epoch VLBI data at 43 GHz. Adopted from Mertens et al. (2016).

Baseline Interferometry (VLBI) studies (e.g., Giroletti et al., 2004; Nagai et al., 2014); see Figure 2.4. Limb brightening is thought to be observed when a velocity gradient exists across the jet, and the emission from the spine has a narrower beaming angle compared to the angle at which the jet is observed (e.g., Giroletti et al., 2004; Nagai et al., 2014). The spine-sheath framework for relativistic jets addresses specific challenges encountered in single-component jets (e.g., Lyutikov and Lister, 2010; Meliani and Keppens, 2009). Moreover, the intensified radiation at the interface between the spine and sheath could potentially contribute to the phenomenon of limb brightening observed in the case of relativistic jets (Giroletti et al., 2004). Several well-resolved strong-flavor jets, particularly in the transverse direction, exhibit limb-brightening or flat-topped emission profiles away from bright knots (Carilli et al., 1996; Swain et al., 1998; Böttcher et al., 2012). Strong-flavor jets are mostly one-sided, seen in quasars, and exhibit narrow spreading, and parallel magnetic field dominance, terminating at hot spots to form luminous two-lobed FR II sources as described by Böttcher et al. (2012). The observed suppression of emission near the jet axis, as indicated by these profiles, may be linked to differential Doppler boosting between a fast, relativistic spine and a slower-moving boundary layer (Böttcher et al., 2012).

2.3.3 Jet Composition

A fundamental question connected with the essence of relativistic jets in AGNs pertains to their constitution: whether they consist of protons and electrons, electron-positron pairs, or a combination thereof, remains an unresolved query. While there is no definitive consensus, several theories and observations provide insights into the possible composition

of these jets. Observations of synchrotron radiation, a product of high-energy electrons spiraling within magnetic fields, furnish support for the existence of electrons within relativistic jets.

Arguments supportive of proton-electron composition within quasar jets are elucidated by Celotti and Fabian (1993). Employing synchrotron self-Compton constraints derived from radio-core observations and information about the energetics of jets obtained from studies of the radio lobes, these investigators demonstrated that the scenario of exclusively electron-positron jet composition faces a challenge due to the impractically high number of electron-positron pairs that would need to be generated by the central engine. Utilizing the constraints set by the annihilation process and the minimum Lorentz factor of the electron distribution, they put forward a plausible scenario suggesting that jets consist of an electron-proton plasma. The arguments supportive of the hybrid composition of the plasma in jets have been advanced by Sikora and Madejski (2000). They propose that jets are initially comprised predominantly of a proton-electron plasma, with the protons contributing to the overall momentum to account for the kinetic energy output of the jet. Later on, this plasma gets enriched by electron-positron pairs due to interactions with high-energy X-rays or soft gamma-rays emitted by the hot corona of the accretion disc.

The radiation emitted from relativistic jets carries information about the composition and energy distribution of jet particles. By analyzing the spectral properties of the radiation, researchers can estimate the energy content, particle densities, and energy distribution within the jet. However, despite extensive endeavors aimed at unraveling the composition of relativistic jets, the matter still continues to be a subject of debate and investigation.

2.3.4 Jet Launching

One of the fundamental questions in the study of relativistic jets involves determining the factors that dictate whether AGNs exhibit radio-loud or radio-quiet behavior. It is firmly established that the radio-loudness of AGNs is connected to the presence of jets. However, the precise mechanism behind the emergence of relativistic jets remains somewhat elusive. The jet launching is likely intertwined with the spin of the supermassive black hole and the rotation of the accretion disk. The prevailing theory for a jet launching from a black hole stems from the proposition of Blandford and Znajek (1977), suggesting that the rotational energy of a black hole could be extracted through electromagnetic stress, ultimately transforming into Poynting flux that eventually powers the jet. Another significant mechanism that could play a role in the launching of jets is the Blandford and Payne (1982) process, where the jet originates from the accretion disc rather than the central black hole. This process results in a jet primarily composed of matter, in contrast to the Poynting flux-dominated jets associated with the Blandford and Znajek (1977) process. Generally, Blandford and Payne (1982) jets tend to exhibit lower relativistic speeds compared to those stemming from the Blandford and Znajek (1977) mechanism. The Blandford-Znajek process can be explained within the context of general relativistic mag-

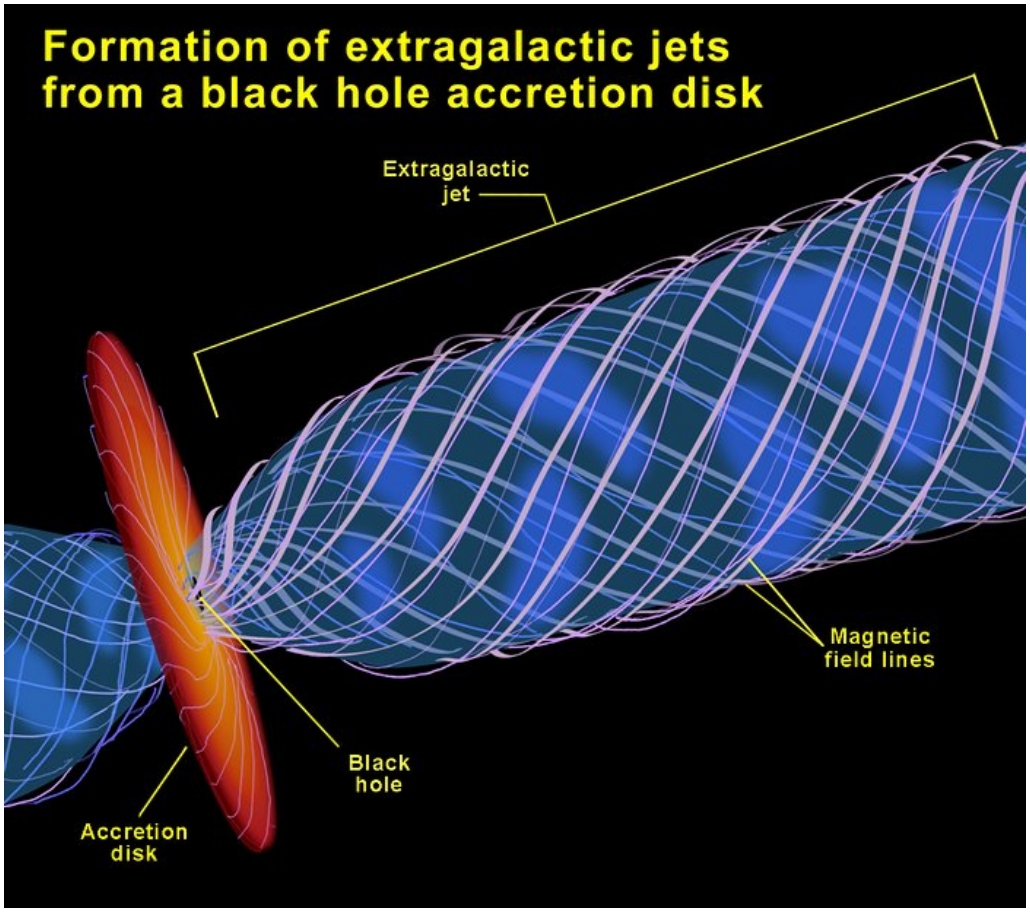

Figure 2.5: Schematic representation of the jet launching process (Blandford-Znajek mechanism). This process is driven by magnetic field lines that become twisted as a result of black hole frame-dragging and/or the differential rotation of the accretion disk. Through these magnetic field lines, the jet becomes connected to both the event horizon of the black hole and the accretion disk. This enables the rotational energy, generated by the spinning black hole and rotating accretion disk, to be transferred. Image credit: NASA/ESA and Ann Feild (Space Telescope Science Institute).

netohydrodynamics, combining hydrodynamics with Maxwell's equations and Einstein's equation of general relativity to describe the motion of the plasma in the curved space-time around a black hole. In a qualitative sense, a rapidly rotating black hole distorts the space-time around it, exhibiting a characteristic property known as rotational frame-dragging (Lense and Thirring, 1918). This phenomenon induces the precession of tilted orbits for test particles orbiting the black hole, compelling particles close to the black hole to partake in its rotation. In the case of a rapidly spinning black hole, the orbits can approach speeds close to the speed of light. The magnetic field lines within the accretion disk follow the motion of the plasma due to the frozen-in condition. Near the black hole, the frame-dragging effect causes magnetic field lines to be dragged in the direction of the black hole's rotation, leading them to wind around the black hole's event horizon. Consequently, the magnetic field lines near the horizon coil up, generating an outgoing angular momentum flux along the rotational axis of the black hole. This process results

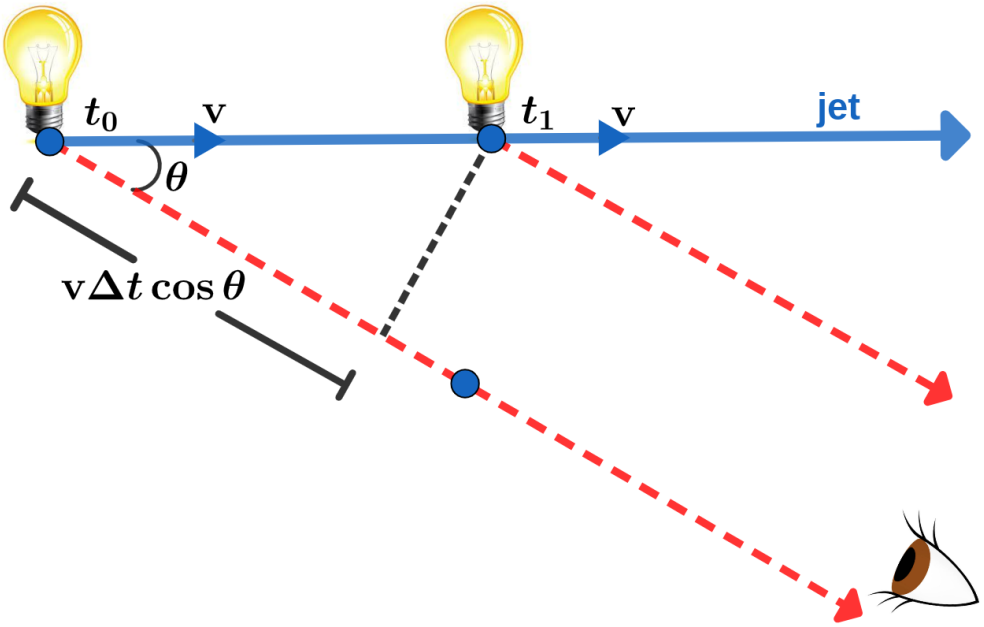

Figure 2.6: An elucidative diagram depicting apparent superluminal motion: two moving bulbs symbolize the source traveling to the right. The arrows depict light rays traveling from the source to an observer, with Δt representing the time interval between two light bursts. The source is in motion at a velocity v making an angle θ with respect to the observer's line of sight.

in the electromagnetic extraction of rotational energy from the black hole, converting it into Poynting flux, ultimately launching the jet.

The validity of the Blandford-Znajek process has been substantiated through General Relativistic Magnetohydrodynamic (GRMHD) simulations (e.g., McKinney and Narayan, 2007; Liska, 2019; Vourellis and Fendt, 2021; Kaaz et al., 2023). Nevertheless, a range of unresolved inquiries concerning jet launching continues. For instance, the reasons behind the pronounced collimation of jets and the mechanisms that confine them, particularly as they extend to significant distances from the black hole, continue to pose challenges. Addressing these inquiries requires additional GRMHD simulations and observational investigations.

2.3.5 Relativistic Motions Within Jets

In the study of blazar jets, high-resolution observations reveal knotty structures that appear to move at speeds exceeding the speed of light. This apparent contradiction with special relativity is a confirmation of the apparent superluminal motions in relativistic jets. Relativistic effects play a crucial role in shaping the distinctive appearance of astrophysical jets. While these potent jets might initially appear lopsided, the underlying reason lies in the phenomenon of relativistic beaming. As these jets move closer to our line of sight, a trio of interconnected factors collaborates to create this illusion. First, the photons emitted by

the jet experience a blue shift, causing them to appear more energetic than they actually are. Second, the relativistic aberration leads to most of the radiation being emitted in a narrow cone (1/Gamma) along the jet and thereby intensifies the emission in the forward direction. Lastly, together with the light-travel-time effects, time intervals in the co-moving frame are actually shortened by one Doppler factor when seen in the observer's frame. Collectively, these intertwined relativistic effects combine to craft the illusion of a one-sided jet, obscuring its inherent symmetry. When accounting for these effects, astrophysical jets may unveil a more balanced and symmetrical structure, underscoring the pivotal role that relativity plays in shaping our understanding of the universe. The diagram in Figure 2.6 portrays a geometric arrangement that elucidates the occurrence of the apparent superluminal motion phenomenon. An electron within the source releases a photon at time t_0 and another photon at time t_1. The displacement of the source in physical space during the time interval $\Delta t = t_1 - t_0$, as observed by an observer, is a projection of the actual distance moved in a direction perpendicular to the line of sight. This projection can be expressed as $\Delta x = v\Delta t \sin\theta$, where v is the velocity of the source. When light is emitted from the source in its initial position, it must travel an additional distance of $v\Delta t \cos\theta$ to reach the observer, compared to the light emitted at time t_1. As a result, the observer does not perceive the source to have shifted by Δt in time, but rather by a time interval, $\Delta t_{\rm obs} = (c\Delta t - v\Delta t\cos\theta)/c = \Delta t\,(1 - \beta\cos\theta)$, where $\beta = v/c$. The apparent velocity of the source which the observer measures, is then given by

$$v_{\rm app} = \Delta x/\Delta t_{\rm obs} = \frac{c\ \beta\sin\theta}{1-\beta\cos\theta} \tag{2.1}$$

When a relativistic jet is pointed at a narrow angle relative to the observer's line of sight, it appears to move at an extremely high speed. The highest apparent speed occurs when the angle (θ) between the jet's direction and our line of sight is such that $\beta = \cos\theta$. At this specific angle, known as the superluminal angle or Critical angle, the maximum observed velocity ($\rm v_{app,max}$) is equal to Γv, Γ being the bulk Lorentz factor of the jet.

The relativistic Doppler effect, a fundamental concept in the realm of astrophysics and high-energy astrophysical phenomena, emerges as a result of the motion of objects at substantial fractions of the speed of light. It was initially predicted and named by Christian Doppler in 1842 in the fields of acoustics and optics. In the context of relativistic jets observed in AGNs, the relativistic Doppler effect plays a pivotal role (e.g., Böttcher et al., 2012).

The Doppler factor for a jet can be expressed using the following equation:

$$\delta = \frac{1}{\Gamma(1-\beta_\Gamma\cos\theta)} \tag{2.2}$$

where Γ is the Lorentz factor of the jet and $0 \leq \theta \leq \pi$ is the viewing angle.

In the case of a counter-jet, where $\theta > \pi/2$, the Doppler factor (δ) always remains below 1. This behavior is easily deduced from Equation 2.2, indicating that a counter jet consistently experiences Doppler deboosting. For an approaching jet, the situation is more intricate.When $\theta = 0$, the Doppler factor δ is given by $\delta = \frac{1}{\Gamma(1-\beta)} = \frac{1+\beta}{\Gamma(1-\beta^2)} = \Gamma(1+\beta)$,

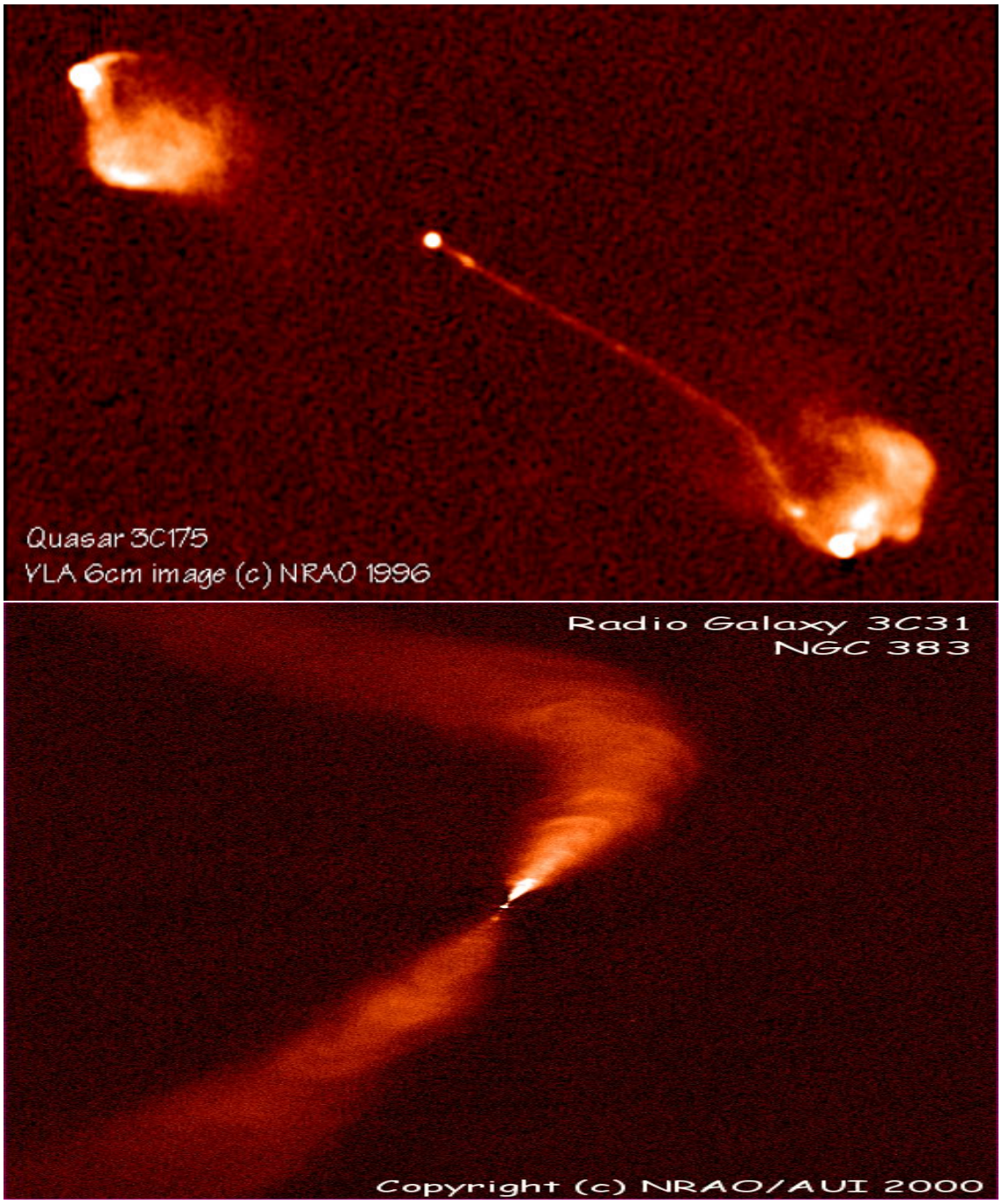

Figure 2.7: Depiction of the relativistic beaming phenomenon in jets: The top image portrays the 3C 175 jet, exhibiting twin jets oriented nearly directly towards and away from Earth; the jet directed towards Earth is distinctly observable (Image credit: Alan Bridle, NRAO Charlottesville, VLA, NRAO, NSF). The bottom image showcases the 3C 31 jet (Image credit: Legacy Astronomical Images, Radio Galaxy 3C31, NRAO/AUI Archives), where both jets lie approximately perpendicular to our line of sight, making both simultaneously visible. The upper jet subtly inclines more toward Earth's direction (line of sight), resulting in enhanced brightness.

which is always greater than 1. This applies to highly relativistic motion with $\Gamma \gg 1$. Conversely, for $\theta = 180°$, $\delta = \frac{1}{\Gamma(1+\beta)} \approx \frac{1}{2\Gamma}$. However, in the rest frame of the jet ($\beta = 0, \Gamma = 1$), the Doppler factor is 1, indicating no relativistic effects.

The angle (θ) at which the photon emitted from a relativistic particle, accelerated within relativistic jets, as observed in the observer's frame is expressed as:

$$\cos\theta = \frac{\cos\theta' + \beta}{1 + \beta\cos\theta'}, \tag{2.3}$$

where θ' represents the angle of photon propagation in the rest frame of the jet and $\beta = \sqrt{1-(1/\Gamma^2)}$ is the normalized speed of the jet plasma. If a photon is emitted perpendicular to the jet axis ($\cos\theta' = 0$) in its rest frame, the observer will receive it at an angle of $\cos\theta = \beta$ (see Equation 2.3). When Γ is significantly larger than 1, it implies that β is nearly equal to one, and consequently, the corresponding angle $\theta = \cos^{-1}(\beta)$ becomes small. In this scenario, we can employ a Taylor expansion for both β and $\cos\theta$ to establish the following relationships:

$$\beta = \sqrt{1 - \frac{1}{\Gamma^2}} \approx 1 - \frac{1}{2\Gamma^2} \tag{2.4}$$

and

$$\cos\theta \approx 1 - \frac{\theta^2}{2} \tag{2.5}$$

When we compare Equations 2.4 and 2.5, we see that photons emitted at a perfect right angle to the jet axis in the rest frame will be received at an angle of approximately $\theta = 1/\Gamma$ in the observer's frame. Now, if we assume that the relativistically approaching source emits photons uniformly in all directions in its own frame, approximately half of all photons will be concentrated within a narrow cone with an opening angle of approximately $\theta = 1/\Gamma$ in the observer's frame. Readers are recommended to refer to Böttcher et al. (2012) for comprehensive literature on relativistic beaming within jets.

We can examine how the Lorentz transformations impact the measured radiation fluxes from an object moving at relativistic speeds. We define the energy flux in electromagnetic radiation as follows:

$$F_\nu = \frac{h\nu\ d^3N_{\rm ph}}{dt\, dA\, d\nu}, \tag{2.6}$$

Here, $dN_{\rm ph}$ represents the photon counts within a frequency interval $[\nu, \nu + d\nu]$, and since it is an integer value, it remains constant in all reference frames. dA denotes a unit area interval. We can express dA in terms of the distance D between the source (s) and the observer (obs) as $dA = D^2 d\Omega$, where $d\Omega$ is a solid angle element which is defined as $d\Omega = d\mu d\phi$, where $\mu = \cos\theta$. To determine how fluxes are transformed between the source's and observer's frames, we need to compute:

$$F^{\rm obs}_{\nu^{\rm obs}} = F^{\rm s}_{\nu^{\rm s}} \frac{\nu^{\rm obs}}{\nu^{\rm s}} \frac{d\nu^{\rm s}}{d\nu^{\rm obs}} \frac{d\Omega^{\rm s}}{d\Omega^{\rm obs}} \frac{dt^{\rm s}}{dt^{\rm obs}}. \tag{2.7}$$

The frequency transformations nullify each other, and the ratio of time intervals $dt^{\rm s}/dt^{\rm obs} = \delta$. Given that $\phi^{\rm s}$ is equal to $\phi^{\rm obs}$, the expression $d\Omega^{\rm s}/d\Omega^{\rm obs}$ simplifies to:

$$\frac{d\Omega^{\rm s}}{d\Omega^{\rm obs}} = \frac{d\mu^{\rm s}}{d\mu^{\rm obs}} = \frac{1}{\Gamma^2(1-\beta\mu^{\rm obs})^2} = \delta^2. \tag{2.8}$$

Consequently, we arrive at

$$F^{\rm obs}_{\nu^{\rm obs}} = F^{\rm s}_{\nu^{\rm s}}\ \delta^3. \tag{2.9}$$

Henceforth, the Doppler boosting effect profoundly influences the flux emanating from an approaching jet, substantially amplifying it, while concurrently suppressing the emission from the receding jet. This phenomenon elucidates why, in most cases, the opposing jet remains unobservable. Furthermore, the dominance of non-thermal jet emission in the observed blazar emission is greatly attributed to the Doppler boosting effect. The beaming effect, in particular, offers an explanation for the fact that blazars emit bright and often dominant fluxes of γ-rays, while radio galaxies are comparatively less prominent γ-ray emitters. In the context of the spine-sheath jet structure, γ-ray emissions predominantly emanate from the inner spine region, while the bulk of radio emissions emanate from the outer sheath, as elucidated by, e.g., Blandford et al. (2019). Given the greater speed of the spine compared to the sheath, the observed γ-ray emissions exhibit a considerably narrower, highly concentrated cone, in contrast to the wider dispersion of radio flux. Consequently, only radio jets oriented extremely close to the observer's line of sight emerge as the brightest γ-ray emitters. As a result, the SED of blazars spans across a broad spectrum, ranging from radio to γ-ray wavelengths.

Chapter 3

Particle Acceleration and Radiation Mechanisms: Theory

This chapter explores various mechanisms that facilitate the acceleration of relativistic jet plasma and the subsequent emission processes. Additionally, we elucidate the methods employed to evaluate the radiation spectra utilized in our model.

3.1 Magnetic Reconnection

Magnetic reconnection is a fundamental process where magnetic field lines in plasma converge, break, and then reconfigure themselves. This phenomenon results in the conversion of magnetic field energy into kinetic energy by rearranging the topology of the magnetic field. Peter Sweet (Sweet, 1958) and Eugene Parker (Parker, 1957) pioneered the first theoretical model for magnetic reconnection for a collisional plasma within the framework of resistive MHD. Extensive research exists regarding magnetic reconnection, encompassing both the collisional scenario, which relies on resistive MHD (e.g., Zenitani et al., 2010; Medina-Torrejón et al., 2023), and the non-collisional scenario, which is based on kinetic approaches (e.g., Sironi et al., 2015; Guo et al., 2016; Nalewajko et al., 2018). The reconnection proceeds faster in the Petschek model of magnetic reconnection (Petschek, 1964), in which a fundamental assumption is that the inflow and outflow regions are separated by slow-mode shocks. This assumption is particularly relevant in the context of an X-point geometry, where these shocks play a crucial role in mediating the reconnection process and maintaining plasma pressure balance.

Figure 3.1 provides a general overview of the reconnection process. Initially, the magnetic field connects points A to B and A′ to B′, with the field lines oriented in opposite directions. This configuration creates a current sheet in the reconnection region, marked in red. The reconnection process subsequently causes a reconfiguration of these magnetic field lines, resulting in a reduction of magnetic energy. This leads to the reconnection of points A

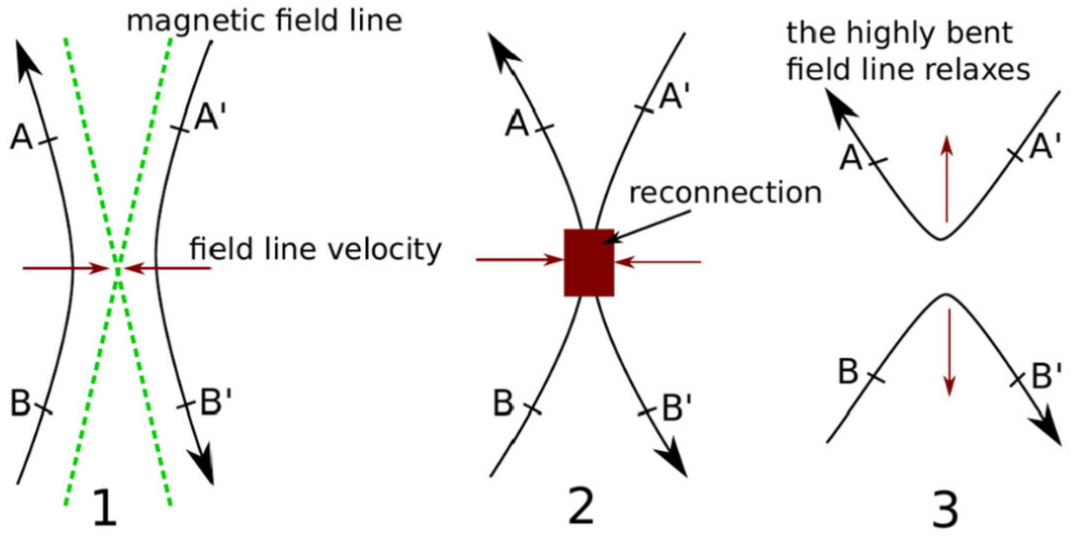

Figure 3.1: A schematic representation of magnetic reconnection in a 2D setting illustrating the process before and after reconnection occurs. In the initial configuration (event 1), anti-parallel magnetic field lines denoted as AB and A′B′ are present within the current sheet, accompanied by plasma flows. The reconnection event takes place in the central region of the figure, highlighted (event 2)). Additionally, dashed green lines are used to indicate separatrices, which serve as boundaries separating regions of the magnetic field that are not topologically connected. The magnetic field lines have undergone a transformation, reconnecting points A with A′ and points B with B′ (event 3). This image has been adopted from Melzani (2014).

with A′ and points B with B′, creating new, highly curved field lines.

Many aspects of magnetic reconnection remain open questions. These include the triggers for reconnection events in celestial objects, the mechanisms responsible for accelerating particles to ultra-relativistic energies, the characteristics of energy spectra, the potential for ions to achieve comparable energies as electrons. A deeper understanding of these queries holds the promise of shedding light on critical astrophysical phenomena.

Within astrophysical jets, magnetic reconnection takes place in the relativistic regime due to the magnetic energy per particle surpassing their rest mass energy. Utilizing PiC simulations to study relativistic magnetic reconnection, it has been observed that when an initial guide field is introduced, the process leads to the development of the relativistic drift kink instability. This instability causes deformation and eventual disruption of the reconnection layer, resulting in substantial plasma heating, but limited production of non-thermal particles. Conversely, a moderate guide field serves to stabilize the reconnection layer and facilitates efficient particle acceleration (e.g., Cerutti et al., 2014). Some studies, employing PiC simulations also reveal that extended current sheets can experience the initiation of plasmoid and tearing-like instabilities, even in the absence of a guide field. These instabilities perturb the smooth structure of the current sheet, resulting in the

emergence of magnetic islands or plasmoids, separated by X-points. This phenomenon not only accelerates the reconnection process but also stimulates interactions between these plasmoids, giving rise to mechanisms of non-thermal particle acceleration (e.g., Sironi and Spitkovsky, 2014). For a more in-depth exploration of magnetic reconnection phenomena, one can reference review articles by Kagan et al. (2015); Marcowith et al. (2020), and references therein.

3.2 Fermi Acceleration Processes

"Never underestimate the joy people derive from hearing something they already know."

– Enrico Fermi

In the dynamic environments of relativistic jets, Fermi acceleration mechanisms come into play as key drivers of particle energization. This process involves high-energy particles gaining energy through interactions with shock waves and turbulent regions within the jet. As particles encounter these shocks and magnetic irregularities, they experience repeated cycles of acceleration, gaining energy with each encounter. This Fermi acceleration process in relativistic jets is responsible for the production of energetic radiation. The Fermi particle acceleration mechanism, as proposed by Fermi (1949), primarily relies on the concept that relativistic particles can increase their energy through elastic collisions with magnetic turbulence patterns or irregularities that are themselves in motion with a characteristic velocity $\vec{u}$. In basic microscopic analysis, assuming that energy remains constant within the frame of reference where the collision occurs, the change in a particle's energy as a result of the collision can be expressed (Rieger et al., 2007) as:

$$\Delta\epsilon = \epsilon_2 - \epsilon_1 = 2\gamma^2(\epsilon_1 u^2/c^2 - \vec{p_1}.\vec{u}), \tag{3.1}$$

where γ represents the bulk Lorentz factor of magnetic irregularities, and $\vec{p_1} = E_1\vec{v}/c^2$ signifies the particle momentum before scattering, associated with its energy E_1, while ϵ_1 and ϵ_2 represent the particle energies normalized by the rest mass energy of an electron before and after scattering. When a particle experiences a head-on collision or approaches the magnetic irregularity (i.e., $\vec{p_1}.\vec{u} < 1$), it gains energy. Conversely, when the particle follows or overtakes the magnetic irregularity (i.e., $\vec{p_1}.\vec{u} > 1$), it loses energy.

The comprehensive discussion of the Fermi acceleration process (Sections 3.2.1 and 3.2.2) relies primarily on literature presented in the works of Longair(2011), supplemented by insights from Rybicki and Lightman(1979) and Dermer and Menon(2009). The discussion concerning shear acceleration in Section 3.2.3 is grounded in the work of Rieger and Duffy (2004), Rieger and Duffy (2005), Rieger and Duffy (2006), and the comprehensive review paper by Rieger (2019).

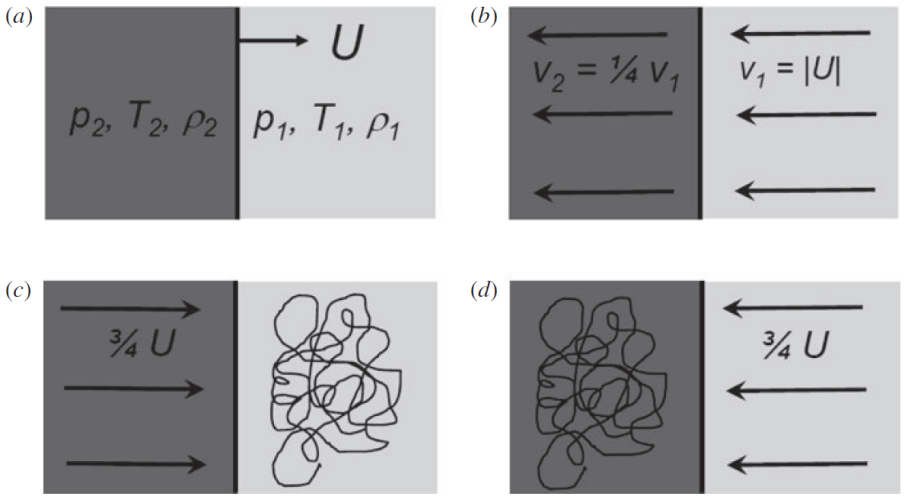

Figure 3.2: The acceleration of high-energy particles near a shock wave: (a) illustrates the dynamics of a shock wave moving at supersonic velocity U through a stationary interstellar gas medium. The light gray region represents the upstream plasma with density ρ_1, pressure P_1, and temperature T_1, while the dark gray region represents the downstream plasma with density ρ_2, pressure P_2, and temperature T_2. (b) depicts the same situation in the reference frame where the shock is at rest. In this frame, the ratio of upstream to downstream velocities is given by $V_1/V_2 = (\Upsilon + 1)/(\Upsilon - 1)$, with Υ being the adiabatic index of the ionized plasma. For a fully ionized mono-atomic, non-relativistic plasma, where $\Upsilon = 5/3$, this ratio, called the compression ratio (R) equals 4. (c) shows the gas flow as observed in the reference frame where the upstream gas remains stationary, and the velocity distribution of high-energy particles is isotropic. (d) similarly displays the gas flow, but from the reference frame where the downstream gas is stationary. The figure has been adopted from Longair (2011).

3.2.1 Diffusive Shock Acceleration

The Fermi first-order acceleration mechanism, commonly known as diffusive shock acceleration as described by (e.g., Krymskii, 1977; Bell, 1978; Blandford and Ostriker, 1978; Axford et al., 1977), involves high-energy particles gaining kinetic energy by repeatedly crossing shock fronts generated by supersonic collisions (e.g., Summerlin and Baring, 2012). These particles' momenta are reversed due to magnetic fields so that they can return to the shock. Magnetic fields scatter the particles and lead to a net energy increase with each crossing. Shock acceleration is often considered a primary mechanism for rapidly and efficiently accelerating particles to energies in the range of GeV to TeV within relativistic jets. The formation of shocks is inhibited in highly magnetized environments. This is described by the magnetization parameter, σ_B, which is calculated as the ratio of the magnetic field energy density to the plasma's rest mass energy density, (i.e., $\sigma_B = B^2/4\pi n_e m_e c^2$, where n_e is the electron density). When $\sigma_B << 1$, it promotes the formation of shocks and Fermi-type particle acceleration. Conversely, when $\sigma_B \geq 1$, it suppresses shock formation and instead encourages magnetic reconnection processes.

Non-relativistic shocks, characterized by $U << c$, are observed in various astrophysical phenomena like supernova remnants, AGN winds, and interactions between stellar winds. Mildly-relativistic shocks (i.e., $\beta\gamma \sim 1$, where $\beta = U/c$), are found in scenarios such as internal shocks within AGN jets and GRBs. Relativistic shocks, i.e., $\gamma >> 1$, are encountered in external shock situations like those in GRBs and pulsar-wind nebulae.

Let us now calculate the energy increase of a particle following its passage through a non-relativistic shock. In the reference frame of the shock, the upstream medium moves faster than the downstream one ($V_1 > V_2$), and they approach each other at a relative speed of $V_{\rm rel} = V_1 - V_2 = \frac{3U}{4}$. If we consider a particle with energy E, as measured in the reference frame of the upstream plasma (assumed as non-relativistic), we can determine its energy as E' as seen in the downstream region using Lorentz transformations:

$$E' = \gamma(E + \vec{p}\cdot\vec{V}_{\rm rel}) = \gamma\left[E + (E/c)V_{\rm rel}\cos\theta\right] \approx E(1 + \frac{V_{\rm rel}}{c}\cos\theta), \tag{3.2}$$

where θ represents the angle between the particle's velocity vector and the vector perpendicular to the shock front. So the relative energy gain (i.e., $(E' - E)/E = \Delta E/E$) by the particle passing from the upstream to the downstream is given by

$$\frac{\Delta E}{E} = \frac{V_{\rm rel}}{c}\cos\theta \tag{3.3}$$

Next, we calculate the average energy gain of the particle across different angles. Since the particle velocity distribution is assumed isotropic, the likelihood that a particle will move within an angle range between θ and $\theta + d\theta$ is determined by:

$$P_{\rm cross} = \frac{\int_0^1 \cos^2\theta d(\cos\theta)}{\int_0^1 \cos\theta d(\cos\theta)} = \frac{2}{3} \tag{3.4}$$

Thus, the average relative energy gain while passing from upstream to downstream plasma becomes

$$\left\langle \frac{\Delta E}{E} \right\rangle = \frac{2}{3}\frac{V_{\rm rel}}{c} = \frac{1}{2}\frac{U}{c} \tag{3.5}$$

Beyond the shock front, turbulent magnetic mirrors scatter particles, causing their velocity vectors to become randomized and propelling them back into the upstream region. Upon re-crossing the shock front and returning to the upstream medium, the particle once more elevates its energy, accumulating an identical energy increase, with an average value of $\left\langle \frac{\Delta E}{E} \right\rangle = (1/2)(U/c)$. Consequently, over the course of one complete journey across the shock front, the particle, on average, experiences an energy gain of:

$$\left\langle \frac{\Delta E}{E} \right\rangle = \frac{U}{c} \tag{3.6}$$

Each time the particle crosses the shock front, it consistently gains energy without any loss, which sets it apart from second-order Fermi acceleration (discussed in Section 3.2.2). These particles remain confined around the shock, bouncing back and forth. It provides the balance between the acceleration and escape of the particles determining the spectral index. Through multiple such crossings, particles gradually accumulate higher energies. This mechanism is termed the first-order Fermi mechanism because the relative energy

gain during each crossing is directly proportional to the shock velocity, thereby resulting in first-order energy increments. In the context of non-relativistic shocks, DSA is recognized for generating power-law particle spectra, specifically $\frac{dN}{dE} \propto E^{-2}$, when the shock is strong (with a compression ratio R = 4). It is noteworthy that these power-law particle spectra remain largely unaffected by the underlying microphysical processes and primarily depend on the shock's compression ratio.

In the first-order Fermi acceleration mechanism, the acceleration timescale can be defined as the time required for a particle to double its energy. This timescale is determined by the number of shock crossings needed for the particle's energy to increase by a factor of 2, which can be approximated as $k \approx \ln 2/\ln(1+U/c)$. When considering a relativistic particle, the duration of a single crossing, $\Delta t \approx \Delta t \approx \lambda/c$, where λ represents the particle's mean free path against interactions with scatterers that can reverse its momentum. Consequently, the first-order Fermi acceleration timescale, denoted as $t_{\rm I}$, can be expressed as $t_{\rm I} = k\Delta t \approx \frac{\ln 2}{\ln(1+\frac{U}{c})}\frac{\lambda}{c}$. For non-relativistic shocks where $U << c$, applying a Maclaurin series expansion to the denominator $\ln(1+\frac{U}{c})$ yields an acceleration timescale approximation of $t_{\rm I} \approx \frac{\lambda}{U}$.

3.2.2 Second Order Fermi Acceleration

The second-order Fermi acceleration mechanism, initially proposed by Fermi (1949), provides a stochastic process through which particles can be accelerated to high energies by interacting with clouds in the interstellar medium. In Fermi's original concept, charged particles undergo reflection from 'magnetic mirrors', which are associated with irregularities present in the Galactic magnetic field. These magnetic mirrors/turbulence are assumed to move randomly with a typical velocity U.

In the absence of dominant shock effects, high-energy particles will encounter both head-on and overtaking collisions, resulting in both energy loss and gain. However, the collision rate is proportional to $|\overrightarrow{V_1} - \overrightarrow{U}|/V_1 \cong (1 - \overrightarrow{V_1} \cdot \overrightarrow{U}/|\overrightarrow{V_1}|^2)$, where U is the random magnetic cloud velocity. This implies that there is a higher likelihood of head-on collisions occurring compared to overtaking collisions.

Let us examine the collision between a particle and a magnetic mirror. This collision occurs with an angle θ between the initial direction of the particle and the normal to the mirror's surface. We will conduct a relativistic analysis to determine the energy change of the particle during a single collision. We are considering an infinitely massive mirror, which means its velocity remains constant during the collision. So, we will work within the center-of-momentum frame of reference, which aligns with the cloud's motion at velocity U. The energy of the particle in the center-of-momentum frame is given by

$$E' = \gamma_{\rm cl}(E + U\ p\ \cos\theta), \quad \text{where} \quad \gamma_{\rm cl} = \left(1 - \frac{U^2}{c^2}\right)^{-1/2}. \tag{3.7}$$

Here, $\gamma_{\rm cl}$ represents the Lorentz factor of the cloud with which the particle interacts.

The component of the relativistic 3-momentum along the x-axis in the center-of-momentum frame is

$$p'_x = p' \cos\theta = \gamma_{\rm cl} \left(p \cos\theta + \frac{UE}{c^2} \right) \tag{3.8}$$

During the collision, in the CM frame, the particle's energy remains conserved, meaning that E' before and after the collision remains constant. However, the particle's momentum undergoes a reversal, changing from p'_x to $-p'_x$. Therefore, when we transform the particle's energy back to the observer's frame,

$$E'' = \gamma_{cl}(E' + Up'_x). \tag{3.9}$$

Therefore, considering Equations (3.7), (3.8), and (3.9), and employing the relationship $p/E = v/c^2$, where v represents the particle's velocity, the change in the particle's energy can be expressed as:

$$\Delta E = E'' - E = E \left[\frac{2Uv\cos\theta}{c^2} + 2\left(\frac{U}{c}\right)^2 \right]. \tag{3.10}$$

For convenience, let us consider the scenario of a relativistic particle ($v \approx c$). In this case, the collisional probability at an angle θ is proportional to $\gamma_{\rm cl}[1+\beta_{\rm cl}\mu]$, where $\beta_{\rm cl} = \frac{U}{c}$, and $\mu = \cos\theta$. Now, when we average over all angles within the range of 0 to π, the first term in Equation (3.10) yields:

$$\left\langle \frac{\Delta E}{E} \right\rangle = (2\beta_{\rm cl}) \frac{\int_{-1}^{1} \cos\theta[1+\beta_{\rm cl} cos\theta] d(\cos\theta)}{\int_{-1}^{1}[1+\beta_{\rm cl}\cos\theta] d(\cos\theta)} = \frac{2}{3}\left(\frac{U}{c}\right)^2 \tag{3.11}$$

Now, when considering the inclusion of the last term from Equation (3.10) as well, the average relative energy gain per collision becomes:

$$\left\langle \frac{\Delta E}{E} \right\rangle = \frac{8}{3}\left(\frac{U}{c}\right)^2. \tag{3.12}$$

As observed, the average relative energy gain per collision scales with the square of the magnetic cloud velocity. Hence, this acceleration mechanism is denoted as *second-order Fermi acceleration*. It is also characterized as *stochastic* because particles undergo diffusion within the medium, experiencing energy fluctuations during each scattering event, resulting in gradual energy increase through stochastic processes. The associated acceleration time scale of this process is:

$$t_{II} = \frac{\lambda\, c^2}{4vU^2}, \tag{3.13}$$

where λ represents the particle's mean free path during scattering. The greater the number of scatterings a particle undergoes with the clouds, the greater its energy increment. Second-order Fermi acceleration is usually expected to lead to particle spectra $\frac{dN}{dE} \propto E^{-(1+t_{II}/t_{\rm esc})}$, where $t_{\rm esc}$ is the particle escape time scale.

3.2.3 Shear Acceleration

Shear flows are ubiquitous in various astrophysical environments. Notable examples include the rotational accretion flows encircling compact celestial objects and the relativistic

jets, observed in phenomena like GRBs and AGNs (e.g., Rieger and Duffy, 2004; Liang et al., 2013a; Rieger, 2019) . The presence of shear boundary layers in relativistic jets was initially inferred from observations of FR I sources (Stawarz and Ostrowski, 2002). Also, in certain observed FR II radio sources, such as 3C 353, a jet morphology has been interpreted as a Doppler-deboosted relativistic spine enveloped by a slower-moving boundary layer has been interpreted (Swain et al., 1998; Stawarz and Ostrowski, 2002). Similar phenomena, such as a fast central spine and a slow sheath, have been observed in other sources like Cyg A and 3C 84 (e.g., Boccardi et al., 2016; Mertens et al., 2016; Martí, 2019).

The concept of shear acceleration is rooted in the idea that energetic particles can acquire additional energy through interactions with small-scale irregularities in the magnetic field that exhibit systematic motion. These interaction points (scattering centers) are believed to be embedded within a collisionless shear flow. Importantly, each scattering centre's velocity aligns with the local flow velocity, distinguishing this process from second-order Fermi acceleration, which involves random motion of scattering centres. Consequently, shear acceleration primarily uses the kinetic energy of the background flow. During particle scattering in this scenario, the momentum of a particle becomes randomized in direction while its magnitude remains conserved within the local co-moving frame of fluid or scattering frame (Rieger and Duffy, 2005). When there is no velocity shear or flow divergence, particles neither gain energy nor momentum solely from scattering. However, in the presence of a velocity shear within the flow, a particle's momentum changes as it traverses the shear region, potentially resulting in a net increase in energy for the particle.

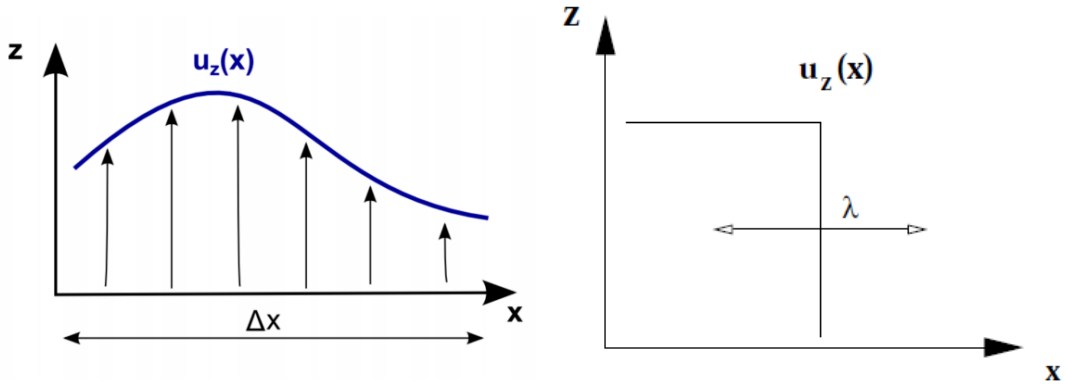

Figure 3.3: Schematic representation of a 2D velocity shear profile: On the left side, a depiction of a shear velocity profile illustrating the scenario of gradual shear is presented (adopted from Rieger (2019)). On the right side, a corresponding representation is shown for the case of non-gradual shear flow (adapted from Rieger and Duffy (2005)). In both illustrations, the flow velocity $u_z(x)$ signifies that the flow is aligned along the z-axis, and its magnitude varies with the x-coordinate. The symbol Δx denotes the width of the transition layer. Notably, in the instance of non-gradual shear, particles encounter a sudden and discontinuous change in the flow velocity.

Rieger and Duffy (2004) categorized various shear scenarios based on the relationship

between a particle's mean free path and the width of the shear layer. In cases where an energetic particle encounters a shear region where the velocity changes smoothly and its mean free path is significantly shorter than the width of the shear region (i.e., $\lambda < \Delta x$, where λ and Δx are particle's mean free path and shear width, respectively), it will experience a gradual shear profile (see Figure 3.3 (left)).

The characteristic acceleration timescale associated with the gradual shear scenario, as elaborated in Rieger and Duffy (2004); Rieger (2019), is expressed as:

$$t_{\rm acc} \cong \frac{3(\Delta r)^2}{\gamma_b^4 c\lambda} \sim \frac{3(\Delta r)^2}{\gamma_b^4 c r_g} \tag{3.14}$$

Here, $\Delta r = r_2 - r_1$ signifies the width of the transition layer, while $\gamma_b(r) = [1 - \frac{v_z(r)^2}{c^2}]^{-1/2}$ characterizes the bulk Lorentz factor, where v_z represents the velocity component along the z direction. Additionally, λ denotes the mean free path of the particle, and r_g signifies the gyroradius of the particle within the magnetic field B. In typical relativistic scenarios observed in parsec-scale radio emissions from AGN jets, $B = 0.01$ G, $\gamma_b(r_1) = 10$, and $\gamma = 300$ for radio-emitting electrons. Consequently, $\lambda \lesssim r_g = 5 \times 10^7(\gamma/300)$ cm. In this context, the electron acceleration timescale near r_1 may be given as

$$t_{\rm acc} \cong 500 \left(\frac{300}{\gamma}\right) \left(\frac{\Delta r}{0.003 \text{ pc}}\right) \text{yr}. \tag{3.15}$$

The corresponding isotropic electron synchrotron cooling timescale is approximately given as

$$t_{\rm cool} \sim 800 \left(\frac{300}{\gamma}\right) \left(\frac{0.01\,\text{G}}{B}\right)^2 \text{yr}. \tag{3.16}$$

Therefore, to ensure efficient electron acceleration, it would be necessary for the shear layer to have a radius of approximately 0.001 pc or less. Equation 3.14 indicates that the acceleration timescale varies inversely with the particle mean free path. Here, the particle gyroradius scales to its mean free path (i.e., $r_g \cong \lambda$). Consequently, this situation aligns with the Bohm diffusion case, where $\lambda \propto \gamma$. As a result, the acceleration time scale is inversely proportional to γ (i.e., $t_{\rm acc} \propto 1/\gamma$). Similarly, the synchrotron cooling time scale follows the same, i.e., $t_{\rm cool} \propto 1/\gamma$. Efficient particle acceleration necessitates an acceleration time scale that is shorter than the synchrotron cooling time scale (i.e., $t_{\rm acc} < t_{\rm cool}$). Given their inverse dependencies on γ, when acceleration becomes efficient ($t_{\rm acc} < t_{\rm cool}$), it can surpass synchrotron losses, sustaining the acceleration. This implies that once the acceleration process efficiently initiates, synchrotron loss no longer has the capability to halt it. Particles continue to be accelerated to higher energies unless a dominating process like escape or cross-field diffusion intervenes. The gradual shear flow can be further divided into two subcategories: gradual longitudinal shear and gradual transverse shear. These mechanisms are recognized as potential sites for particle acceleration within jets. For additional information, readers may refer to Rieger and Duffy (2004).

When a particle gains a significant amount of energy to the extent that its mean free path exceeds the width of the velocity transition layer (i.e., $\lambda > \Delta x$), it can be observed as passing through this layer without significant effects in its velocity. If this particle

undergoes elastic scattering from magnetic irregularities embedded in the background flows and repeatedly crosses this layer, it can efficiently accelerate to high energies. For instance, Ostrowski (1990) has proposed that the boundary between the inner jet of a powerful AGNs and the surrounding medium might serve as such a transition layer across which a sharp drop in velocity occurs naturally at relativistic speeds.

(Ostrowski, 1990, 1998) has estimated a characteristic acceleration timescale in the ambient medium rest frame, given by

$$t_{\rm acc} = \frac{\alpha\lambda}{c} \geq (1-10)\,\frac{r_g}{c}, \qquad \text{if } r_g > \Delta x \tag{3.17}$$

The parameter α is a free parameter, and its suggested value, based on particle simulations, falls within the range of 1 to 10 (Rieger and Duffy, 2004). In this case, the acceleration time scale, $t_{\rm acc} \propto \lambda$. In such scenarios, one would typically anticipate that the gyroradius of electrons is much smaller than the width of the jet. So the non-gradual shear acceleration mechanism would not function efficiently for electrons as the electrons experience rapid radiation losses (synchrotron or inverse Compton) at high energies. However, the mechanism appears to be significantly more favorable for protons as protons could be efficiently accelerated until their gyroradius becomes larger than the shear width. Importantly, the gyroradius of a particle, in this context, does not scale in proportion to its mean free path (i.e., $r_g >> \lambda$), which indicates that the conditions for the Bohm diffusion case are not met.

3.3 Radiative Processes

The powerful jets, often associated with AGNs and GRBs, propel matter to near-light speeds and create extreme conditions. Within these jets, charged particles, such as electrons and protons, gain energy through mechanisms like Fermi acceleration as discussed in section 3.2. As these particles move at relativistic speeds through magnetic fields, they emit synchrotron radiation and high-energy gamma rays via inverse Compton scattering. In this chapter, our objective is to introduce the fundamentals of the non-thermal radiation mechanisms occurring in relativistic jets, namely, synchrotron emission and inverse Compton scattering, along with an overview of recent research developments related to these mechanisms. Given that we are exploring environments such as AGNs and GRBs, characterized by extremely low particle densities, we will not delve into phenomena that result from binary particle collisions, including Coulomb interactions, bremsstrahlung radiation, and electron-positron annihilation. The discourse regarding synchrotron radiation (Section 3.3.1) and Compton scattering (3.3.2) primarily draws from literature authored by Rybicki and Lightman (1979), Dermer and Menon (2009), and Longair (2011). .

3.3.1 Synchrotron Radiation

Synchrotron radiation from ultra-relativistic electrons plays a prominent role in various aspects of high-energy astrophysics (e.g., Longair, 2011). This form of radiation, initially observed during early betatron experiments, involves the emission of high-energy electrons as they spiral within a magnetic field. It is the underlying mechanism responsible for the radio emissions originating from various celestial sources, including our own Galaxy, supernova remnants, and extragalactic radio sources. In the case of non-relativistic motion of charged particles, the radiation produced is referred to as cyclotron radiation. The cyclotron frequency corresponds directly to the frequency at which the charged particle gyrates within the magnetic field. In the case of highly relativistic charged particles, the frequency spectrum becomes more sophisticated, often encompassing frequencies that surpass multiple times the particle's gyration frequency. This radiation phenomenon is referred to as synchrotron radiation.

If we consider the movement of a charged particle with mass m_e, velocity $\vec{v}$, and charge q within the presence of both a magnetic field $\vec{B}$ and an electric field $\vec{E}$, the force exerted on this charged particle due to electromagnetic effects is mathematically described by the Lorentz force equation, which can be expressed as:

$$\frac{d}{dt}(\gamma m_e \vec{v}) = q(\vec{E} + \frac{\vec{v}}{c} \times \vec{B}) \tag{3.18}$$

In the majority of astrophysical plasma environments, the movement of free charges is such that it effectively nullifies the electric field. We make the simplifying assumption that this condition holds true and consider $\vec{E} = 0$. This also implies that the particle undergoes negligible energy loss during a single gyration.

$$q\vec{v} \cdot \vec{E} = \frac{d}{dt}(\gamma m_e c^2) = 0 \implies \gamma = \text{constant}. \tag{3.19}$$

Consequently, Equation (3.18) becomes

$$m_e \gamma \frac{d\vec{v}}{dt} = \frac{q}{c}\, \vec{v} \times \vec{B}. \tag{3.20}$$

When we break down the velocity of a particle into components parallel and perpendicular to the direction of the magnetic field, we observe that $d\vec{v}_{\parallel}/dt = 0$ and $d\vec{v}_{\perp}/dt = (q/\gamma m_e c)(\vec{v}_{\perp} \times B)$. This implies that the component of velocity parallel to the magnetic field remains constant over time. Furthermore, since γ remains constant, the overall magnitude of the velocity $|\vec{v}|$ remains constant as well. Consequently, this leads to the conclusion that the magnitude of the velocity perpendicular to the field, $|\vec{v}_{\perp}|$, also remains constant over time. The solution to this equation indicates that the particle undergoes helical motion.

The gyrofrequency or the Larmor angular frequency of the particle can be expressed as:

$$\omega_B = \frac{qB}{\gamma\ m_e\ c} \tag{3.21}$$

The acceleration is at a right angle to the velocity and has a magnitude of $a_\perp = \omega_B v_\perp$. The emission of Synchrotron radiation occurs when a charged particle undergoes acceleration perpendicular to its velocity. The instantaneous particle energy-loss rate due to synchrotron loss for a particle is determined by:

$$P = \frac{2q^2}{3c^3}\gamma^4(a_\perp^2 + \gamma^2 a_\parallel^2). \tag{3.22}$$

Given that $\vec{v}_\parallel$ remains constant, it follows that $\vec{a}_\parallel = 0$. Consequently, we can express the total emitted radiative power as:

$$P = \frac{2q^2}{3c^3}\gamma^4 \left(\frac{q^2B^2}{\gamma^2 m_e^2 c^2}\right) v_\perp^2 = \frac{2q^2}{3c^3}\gamma^4 \left(\frac{q^2B^2}{\gamma^2 m_e^2 c^2}\right) v^2 \left\langle \sin^2\psi \right\rangle, \tag{3.23}$$

where ψ is the pitch angle, the angle between the magnetic field and velocity. Relativistic electrons within radio sources may sustain their ultrarelativistic energies for thousands to millions of years, depending on the magnetic field strength. These electrons undergo repeated scattering events caused by fluctuations in magnetic fields and interactions with charged particles in their surroundings. As a consequence, their pitch angle distribution gradually transforms into an isotropic configuration. For an isotropic distribution of particle velocities to occur, certain pitch angle scattering mechanisms must be in operation, and these mechanisms should act on a timescale shorter than the timescale of energy loss. Assuming rapid pitch-angle scattering, where a single particle can quickly explore all pitch-angle directions uniformly, we can calculate the rate of energy loss by averaging Equation (3.23) over pitch angle.

$$\left\langle v_\perp^2 \right\rangle = v^2 \left\langle \sin^2\psi \right\rangle = \frac{2}{3}v^2 \tag{3.24}$$

This results in the following equation:

$$P = -\left(\frac{dE}{dt}\right)_{\rm syn} = \frac{4}{3}\sigma_T c \gamma^2 \beta^2 U_B, \tag{3.25}$$

where $\sigma_{\rm T} = 8\pi r_0^2/3$ is the Thomson cross section, $r_0 = e^2/m_e c^2$ is the classical electron radius, $\beta = v/c$, and $U_B = B^2/8\pi$ is the magnetic energy density. If we normalize Equation (3.25) by the electron's rest mass energy ($m_e c^2$) on both sides, the electron synchrotron energy-loss rate in terms of the rate of change of the electron Lorentz factor becomes

$$-\left(\frac{d\gamma}{dt}\right)_{\rm syn} = \frac{4}{3}\sigma_T c \gamma^2 \beta^2 u_B, \tag{3.26}$$

where $u_B = U_B/m_e c^2 = B^2/8\pi m_e c^2$.

Relativistic electrons in most synchrotron sources exhibit power-law energy distributions, indicating that they are not in LTE. Consequently, these sources are commonly labeled as "nonthermal". However, a synchrotron source characterized by a relativistic Maxwellian electron-energy distribution would, at least in theoretical considerations (e.g., Wardzinski and Zdziarski, 2000), be classified as a thermal source. Therefore, the terms "synchrotron"

and "nonthermal" are not entirely interchangeable. The power-law energy distribution of relativistic electrons is

$$N(\gamma)d\gamma = N_0\gamma^{-p}d\gamma, \tag{3.27}$$

where $\mathrm{E} = \gamma \mathrm{m_e c^2}$ represents the energy of a relativistic particle and $\mathrm{N_0}$ signifies the normalization factor determining the density of particles. p represents the power-law index. The Synchrotron emissivity, see e.g., Rybicki and Lightman (1979), may be expressed as

$$\mathrm{j}_\nu = \frac{\sqrt{3}q^2\gamma\sin\psi}{8\pi^2 m_e c^2}F(x) \qquad \left[\mathrm{erg\ } s^{-1}cm^{-3}Hz^{-1}\right], \tag{3.28}$$

where F(x) is given by

$$F(x) = x\int_x^\infty K_{5/3}(\xi)d\xi \tag{3.29}$$

Here, $K_{5/3}$ is the modified Bessel function of the second kind of order 5/3, and $x = \nu/\nu_c$, ν_c being the critical frequency, approximately representing the peak frequency of synchrotron radiation of mono-energetic electrons with Lorentz factor γ. The critical frequency (ν_c) is defined as

$$\nu_c = \frac{3\gamma^2 qB\sin\psi}{2m_e c}, \tag{3.30}$$

The total power per unit volume per unit frequency is obtained by integrating Equation 3.28 over a power-law distribution of relativistic electrons, as defined in Equation 3.27 with $\gamma_1 < \gamma < \gamma_2$. The classical synchrotron theory suggests that an electron's radiation power is proportional to $\nu^{1/3}$ below the critical frequency ν_c (e.g., Dermer and Menon, 2009; Böttcher et al., 2012), a notion seemingly supported by observations in astrophysical sources. However, the $\nu^{1/3}$ spectrum corresponds to angle-integrated radiation, not radiation per solid angle along the line of sight. Despite the isotropic pitch-angle distribution of electrons in many astrophysical processes, the classical $\nu^{1/3}$ spectrum is often considered the default assumption. Also, if ordered magnetic fields exist in the emission region, the momentum distribution of electrons may show notable anisotropy. This anisotropy, particularly evident in cases of helical motion of electrons within large-scale magnetic fields, causes a deviation from the classical $\nu^{1/3}$ spectrum, with the observed spectrum following $F_\nu \propto \nu^{2/3}$ at low frequencies in extreme cases where the angle distribution is a Delta function (e.g., Yang and Zhang, 2018).

Another main characteristic of synchrotron emission is its polarization. Polarization refers to the preferred orientation of the electric field vector of the emitted radiation. Synchrotron radiation is inherently polarized due to the characteristic spiraling motion of charged particles in magnetic fields. The degree and angle of polarization serve as invaluable probes into the magnetic field geometry and the distribution of emitting particles in celestial objects (e.g., Trippe, 2014). The degree of polarization, ranging from complete lack of polarization to full polarization, quantifies the fraction of the total intensity that exhibits a preferred orientation. Additionally, the polarization angle provides crucial information about the orientation of the magnetic field. The unique polarization signature inherent in synchrotron emission has played a pivotal role in unraveling the intricate magnetic structures and dynamic processes within diverse astrophysical sources, including but not

limited to, AGNs and pulsars. This has significantly enriched our understanding of the cosmos. When the magnetic field aligns perpendicular to the observer's line of sight, the radiation appears purely linearly polarized. This is due to the observer perceiving the acceleration vector executing simple harmonic motion in a plane perpendicular to the magnetic field. Conversely, when the magnetic field aligns parallel to the line of sight, the radiation is entirely circularly polarized. This occurs because the acceleration vector continuously changes direction as the electron orbits in a circle around the magnetic field lines. In cases where the magnetic field is at an angle (θ) to the line of sight, the radiation is observed to be elliptically polarized, with the ratio of axes of the polarization ellipse determined by the cosine of θ (e.g., Longair, 2011). Taking into account the influence of beaming effects, the radiation emitted by a single charge will exhibit elliptical polarization. However, when considering a realistic distribution of particles with smooth variations in pitch angle, the elliptical polarization components tend to cancel out. This cancellation occurs because the emission cone contributes equally from both sides of the line of sight. Consequently, the resulting synchrotron radiation becomes partially linearly polarized (e.g., Rybicki and Lightman, 1979).

The linear polarization degree (Π) for particles exhibiting a power-law distribution of energies with an index p (polarized flux/total flux) is found to be

$$\Pi(p) = \frac{p+1}{p+\frac{7}{3}}. \tag{3.31}$$

For a typical value of $p = 2.5$, the polarization degree is determined to be approximately 70%. This is a substantial value; however, it is derived based on the assumption of a uniform magnetic field. The polarization electric vectors are observed either parallel or perpendicular to the jet axis. Explaining perpendicular polarization, common in large-scale radio and optical jets, is challenging as it requires the dominance of longitudinal magnetic fields. In expanding jets, the parallel magnetic field component decays faster than the perpendicular one. To account for this, a process amplifying the poloidal component on large scales, often attributed to velocity shear at the jet boundary–our primary focus in this study–is typically invoked (e.g., Laing, 1980; Nalewajko, 2009).

3.3.2 Compton Scattering

Shortly after the advent of quantum mechanics in 1923, Arthur H. Compton made a groundbreaking discovery–the Compton effect, an inelastic scattering phenomenon involving a photon and a charged particle, typically an electron. Compton's pivotal contribution to understanding this interaction earned him the Nobel Prize in Physics in 1927. The significance of the Compton effect lies in its demonstration that light cannot be exclusively treated as a wave in the high-energy regime, specifically when the photon energy becomes comparable to the rest energy of the charged particle. In this interaction, governed by the conservation of mass-energy and momentum, a portion of the photon's energy is transferred to the charged particle, usually an electron, causing it to recoil. Consequently, the scattered photon is emitted in a different direction with an altered wavelength. This

phenomenon fundamentally revealed the particle-like characteristics of light and remains integral to our understanding of quantum behavior in high-energy physics.

Scattering from Electrons at Rest

The Compton scattering phenomenon can be investigated through two distinct approaches: one involves approximating photons classically as electromagnetic waves (classical approach), and the other considers the scattering of photons from a particle perspective within the framework of quantum mechanics (quantum-mechanical particle approach).

Classical Approach (Thomson Scattering) In the regime of low photon energies ($\epsilon_0 << 1$), the scattering of radiation from free charges converges to the classical scenario of Thomson scattering. In this scenario, the collision between an electron and a photon exhibits elastic behavior (coherent), denoted by $\epsilon_0 = \epsilon_s$. Here, ϵ_s represents the energy of the scattered photon. The differential Thomson cross section for unpolarized incident radiation is given by the expression:

$$\frac{d\sigma_T}{d\Omega} = \frac{1}{2} r_0^2 (1 + \cos^2 \chi), \tag{3.32}$$

where r_0 is the classical electron radius. χ is the angle between the direction of the propagation of the unscattered and scattered photon as shown in Figure 3.4. The total cross-section for scattering into all solid angles is given by

$$\sigma_T = \int_0^\pi \frac{d\sigma_T}{d\Omega} d\Omega = \int_0^\pi \frac{d\sigma_T}{d\Omega} (2\pi \sin \chi d\chi) = \frac{8\pi}{3} r_0^2 = 6.65 \times 10^{-25} \ \text{cm}^2 \tag{3.33}$$

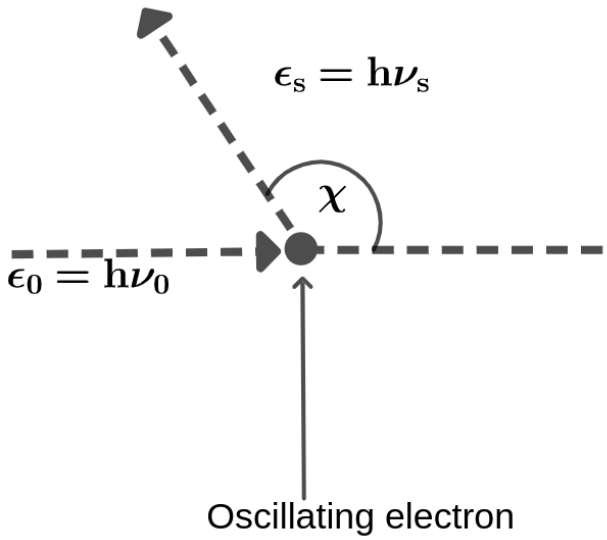

Figure 3.4: Classical Treatment of Compton Scattering with Radiation from a Stationary Oscillating Electron.

Quantum-mechanical particle approach Quantum effects manifest in two distinct manners: firstly, through the kinematics governing the scattering process, and secondly, through variations in the cross sections. Kinematic effects arise from the fact that a photon carries both momentum (hν/c) and energy (hν). The scattering process deviates from being elastic ($\epsilon_0 \neq \epsilon_s$) due to the recoil of the charged particle, be it an electron or proton. In relativity, the conservation of energy and momentum transforms into the conservation of four-momentum. The four-momentum of a particle with mass m and energy E moving in the direction of the unit vector $\hat{n}$ is expressed as:

$$\underline{p} = \left[\gamma mc, \gamma m\vec{v}\right] = \left[\frac{E}{c}, \frac{E}{c}\frac{\vec{v}}{c}\right] = \frac{E}{c}\left[1, \beta\hat{n}\right], \tag{3.34}$$

where c is the speed of light, γ is the Lorentz factor, $\vec{v}$ is the velocity vector, and β is the velocity normalized to the speed of light. The limiting case, where $m \to 0$ and $\beta \to 1$, can be employed for the photon in Equation 3.34 to yield the 4-momentum of a photon:

$$\underline{p_\gamma} = \frac{E_\gamma}{c}\left[1, \hat{n}\right], \tag{3.35}$$

where E_γ is the photon energy.

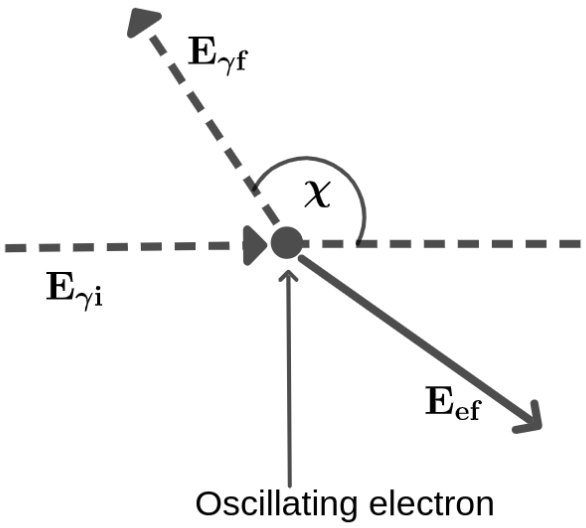

Figure 3.5: Quantum-mechanical particle treatment of Compton scattering involving radiation from a stationary oscillating electron.

Let,
$\vec{p}_{\gamma i}$ = initial 4-momentum of the photon = $\frac{E_\gamma}{c}\left[1 \quad \hat{n}_{\gamma i}\right]$
$\vec{p}_{\gamma f}$ = final 4-momentum of the photon = $\frac{E_\gamma}{c}\left[1 \quad \hat{n}_{\gamma f}\right]$
$\vec{p}_{ei}$ = initial 4-momentum of the electron = $\left[m_e c \quad 0\right]$
$\vec{p}_{ef}$ = final 4-momentum of the electron = $\frac{E_e}{c}\left[1 \quad \hat{n}_{ef}\right]$

Conservation of 4-momentum implies that

$$\begin{aligned}\vec{p}_{\gamma i} + \vec{p}_{ei} &= \vec{p}_{\gamma f} + \vec{p}_{ef} \\ \vec{p}_{ef} &= \vec{p}_{\gamma i} + \vec{p}_{ei} - \vec{p}_{\gamma f}\end{aligned} \tag{3.36}$$

The modulus of a vector A_μ is given by

$$\underline{A}^2 = \eta_{\mu\nu} A^\mu A^\nu = -(A^0)^2 + (A^1)^2 + (A^2)^2 + (A^3)^2 \tag{3.37}$$

and the scalar product of $\vec{A}$ and $\vec{B}$ is

$$\underline{A} \cdot \underline{B} = \eta_{\mu\nu} A^\mu B^\nu = -A^0 B^0 + A^1 B^1 + A^2 B^2 + A^3 B^3 \tag{3.38}$$

The magnitude of the 4-momentum of a particle is given by the equation $\mathrm{p}^2 = -\mathrm{m}^2\mathrm{c}^2$. However, for a photon, the magnitude of its 4-momentum is uniquely determined as $\mathrm{p}^2 = 0$. By squaring both sides of Equation 3.36 and subsequently simplifying the result, we obtain the final expression for the energy of the scattered photon:

$$E_{\gamma f} = \frac{E_{\gamma i}}{1 + \left(\frac{E_{\gamma i}}{m_e c^2}\right)(1 - \cos\chi)} \tag{3.39}$$

$$\epsilon_s = \frac{\epsilon_0}{1 + \epsilon_0(1 - \cos\chi)} \tag{3.40}$$

Here, $\epsilon_s \equiv E_{\gamma f}/m_e c^2$ and $\epsilon_0 \equiv E_{\gamma i}/m_e c^2$. Equation 3.40 indicates that as a result of electron recoil, the scattered photon's energy varies from $\frac{\epsilon_0}{1+2\epsilon_0}$ when scattering backward to ϵ_0 for forward scattering. In the Thomson regime characterized by $\epsilon_0 \ll 1$, the energy of the scattered photon, $\epsilon_\mathrm{s} \approx \epsilon_0$ regardless of the scattering direction. Conversely, the Klein-Nishina regime is marked by $\epsilon_0 \gg 1$. The wavelength change of a photon is given as $\lambda_\mathrm{s} - \lambda_0 = \lambda_\mathrm{C}(1 - \cos\chi)$, where $\lambda_\mathrm{C} \equiv \mathrm{h/m_e c} = 0.02426\text{Å}$ is the Compton wavelength. For photons with long wavelengths ($\lambda \gg \lambda_C$ or $h\nu \ll m_e c^2$), scattering is almost entirely elastic. Under these conditions, we can assume no change in photon energy in the Electron Rest Frame (ERF).

Alongside the relativistic effects dictated by the conservation of energy and momentum, quantum mechanical influences alter the electron cross-section, deviating from the classical value. The Klein-Nishina formula expresses the differential cross-section as:

$$\frac{d\sigma_\mathrm{KN}}{d\Omega} = \left(\frac{r_0^2}{2}\right)\left(\frac{\epsilon_s}{\epsilon_0}\right)^2\left(\frac{\epsilon_s}{\epsilon_0} + \frac{\epsilon_0}{\epsilon_s} - \sin^2\chi\right). \tag{3.41}$$

For $\epsilon_s \sim \epsilon_0$, Equation 3.42 reduces to the classical expression (i.e. Equation 3.32). The main consequence is a decrease in the cross-section compared to its classical value as the photon energy increases. Consequently, Compton scattering exhibits reduced efficiency at higher energies. Upon integrating Equation 3.41 over a solid angle, we obtain the total Klein-Nishina cross-section as follows:

$$\sigma_{KN} = \frac{3}{4}\sigma_T\left[\frac{1+\epsilon_0}{\epsilon_0^3}\left\{\frac{2\epsilon_0(1+\epsilon_0)}{1+2\epsilon_0} - \ln(1+2\epsilon_0)\right\} + \frac{1}{2\epsilon_0}\ln(1+2\epsilon_0) - \frac{1+3\epsilon_0}{(1+2\epsilon_0)^2}\right] \tag{3.42}$$

In the nonrelativistic regime, i.e., $\epsilon_0 \ll 1$, we have the scattering cross-section

$$\sigma = \sigma_T \left(1 - 2\epsilon_0 + \frac{26\epsilon_0^2}{5} + ...\right), \tag{3.43}$$

whereas for the extreme relativistic regime, we have

$$\sigma = \frac{3}{8}\sigma_T \epsilon_0^{-1} \left(\ln 2\epsilon_0 + \frac{1}{2}\right) \tag{3.44}$$

$\sigma \to 0$ as $\epsilon_0 \to \infty$.

Scattering from Electrons in Motion

In the electron's rest frame, where $\epsilon_0 \ll 1$, the Klein-Nishina formula's relativistic corrections can be safely neglected. However, in many astrophysical scenarios, electrons exhibit relativistic velocities, necessitating a detailed consideration of Klein-Nishina effects. When the moving electron possesses significant kinetic energy relative to the photon, there is a net transfer of energy from the electron to the photon, leading to the phenomenon known as *inverse Compton scattering*.

3.3.3 Inverse Compton Radiation

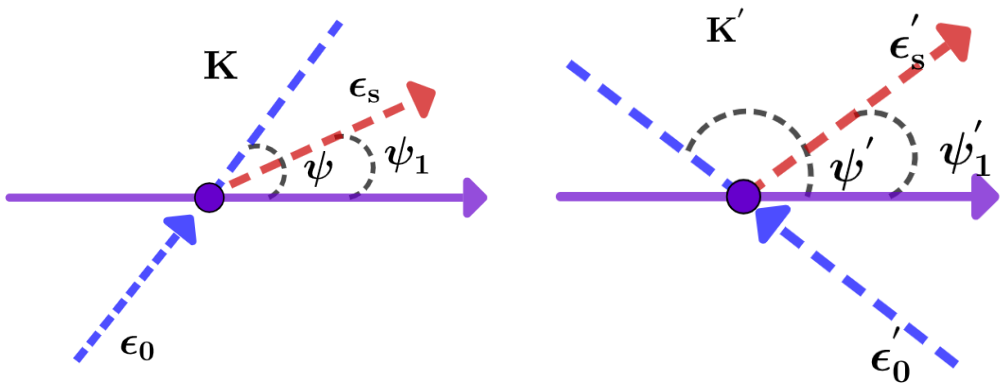

Figure 3.6: Illustration of scattering geometries, showing the electron rest frame (K′) on the right and laboratory frame (K) on the left. Angular measurements are taken clockwise from the positive axis defined by the electron velocity.

Let K represent the lab or observer's frame, and K′ denote the rest frame of the electron. The depiction of the scattering event as observed in each frame is illustrated in Figure 3.6. The notational conventions employed in this section are presented in Table 3.1.

The photon energies undergo reverse and forward transformations between the ERF and the Laboratory Frame (LF), resulting in:

$$\epsilon_0' = \gamma\epsilon_0 \left(1 - \beta\cos\psi\right) = \gamma\epsilon_0 \left(1 - \beta\mu\right) \tag{3.45}$$

Table 3.1: Notations and Definitions for Inverse Compton Scattering

Notation	Definition
K	Laboratory Frame (LF)
$K^{'}$	Electron rest frame (ERF)
$\epsilon_0^{'}$	Unscattered photon energy in the ELF normalized by the electron rest mass energy, i.e., $\epsilon_0^{'} = \frac{h\nu^{'}}{m_e c^2}$
ϵ_0	Unscattered photon energy in the LF, $\epsilon_0 = \frac{h\nu}{m_e c^2}$
ϵ_s	Scattered photon energy in the LF, $\epsilon_s = \frac{h\nu_s}{m_e c^2}$
$\epsilon_s^{'}$	Scattered photon energy in the ELF, $\epsilon_s^{'} = \frac{h\nu_s^{'}}{m_e c^2}$
γ	Lorentz factor of the relativistic electron
β	Velocity of a relativistic electron, i.e., $\epsilon = \frac{v}{c}$
ψ	The angle between the initial photon direction and the velocity of the electron in the LF.
$\psi^{'}$	The angle between the initial photon direction and the velocity of the electron in the ELF
ψ_1	Angle between the electron and the photon propagation directions after scattering as observed in the LF
$\psi_1^{'}$	Angle between the electron and the photon propagation directions after scattering as observed in the ELF
σ_T	Thomson cross-section
n_{ph}	Number density of the target photons

$$\epsilon_s = \gamma\epsilon_s^{'}\left(1 + \beta\cos\psi_1^{'}\right) = \gamma\epsilon_s^{'}\left(1 + \beta\mu_1^{'}\right) \tag{3.46}$$

Here, $\mu = \cos\psi$ and $\mu_1^{'} = \cos\psi_1^{'}$. Therefore, with the exception of angles near $\mu = 1$, the photon gains a factor of γ during the transformation to the ERF. Similarly, except for angles near $\mu_1^{'} = -1$, a factor of γ is acquired when transforming the energy of the scattered photon back to the laboratory frame. In the Thomson regime and in the ERF, $\epsilon_0^{'} = \epsilon_s^{'}$. So the maximum scattered photon energy in the Thomson regime can be obtained from Equation 3.46 as:

$$\epsilon_{s_{max}} = 2\epsilon_s^{'}\gamma = 2\epsilon_0^{'} = 4\gamma^2\epsilon_0 \tag{3.47}$$

In the Klein-Nishina regime, the maximum scattered photon energy can be constrained by using the principle of the conservation of the energy as:

$$\epsilon_{s_{max}} < \gamma m_e c^2 + \epsilon_0 \sim \gamma m_e c^2 \tag{3.48}$$

Within the Thomson regime, where the scattered photon energy is much less than the energy of the scattering electron, i.e., $\epsilon_s < (\gamma - 1) \approx \gamma$, the condition $4\gamma\epsilon_0 \ll 1$ is satisfied.

Considering that ψ and $\psi^{'}$ are typically of the order $\pi/2$ (e.g., Rybicki and Lightman, 1979), the photon energy ratios during the transformation from the LF to the ERF and then back to the LF, derived from Equations 3.46 and 3.47, are of the order:

$$1 : \gamma : \gamma^2$$

3.3.4 Radiated Power in Inverse Compton Scattering for a Single Electron

Consider the incident flux of isotropic photons on the electron in the ERF. Let, in the ERF, the number density of photons having energy in the range $d\epsilon_0^{'}$ be $n_{ph}^{'}(\epsilon_0^{'})d\epsilon_0^{'}$. In the Thomson regime, the total inverse Compton emitted power in the ERF can be expressed as:

$$\frac{dE_1^{'}}{dt^{'}} = \sigma_T c \int m_e c^2 n_{ph}^{'}(\epsilon_o^{'})\epsilon_s^{'}(\epsilon_0^{'})d\epsilon_0^{'} \tag{3.49}$$

As the power emitted by the electron is Lorentz invariant, we can write:

$$\frac{dE_1}{dt} = \frac{dE_1^{'}}{dt^{'}} \tag{3.50}$$

The invariance of the phase space distribution is expressed as $f(X,p) := \frac{dN}{d^3\vec{x}\,d^3\vec{p}} = f^{'}(X^{'},p^{'})$. Here, let $n_{\rm ph}(\epsilon_0)d\epsilon_0 = f_{\rm ph}(X,p)d^3p$, where $f_{\rm ph}$ represents the photon distribution function. Since d^3p is Lorentz transformed the same as energy, we can write:

$$\frac{n_{ph}(\epsilon_0)d\epsilon_0}{\epsilon_0} = \frac{n_{ph}^{'}(\epsilon_0^{'})d\epsilon_0^{'}}{\epsilon_0^{'}} = \text{Lorentz invariant} \tag{3.51}$$

Now, with Equation 3.45 and the fact that in the Thomson regime, $\epsilon_{\rm s}^{'} = \epsilon_0^{'}$ in the ERF, we can express the photon energy density $U_{rad}^{'}$ in the ERF as:

$$\begin{aligned} U_{rad}^{'} &= \int m_e c^2 \epsilon_0^{'} n_{ph}^{'}(\epsilon_0^{'})d\epsilon_0^{'} = \int m_e c^2 \epsilon_0^{'2} \frac{n_{ph}^{'}(\epsilon_0^{'})d\epsilon_0^{'}}{\epsilon_0^{'}} = m_e c^2 \int \epsilon_0^{'2} \frac{n_{ph}(\epsilon_0)d\epsilon_0}{\epsilon_0} \\ &= m_e c^2 \int \epsilon_0^2 \gamma^2 (1-\beta\mu)^2 \frac{n_{ph}(\epsilon_0)d\epsilon_0}{\epsilon_0} \end{aligned} \tag{3.52}$$

Since $\langle\mu\rangle = 0$ and $\langle\mu^2\rangle = 1/3$, for an isotropic photon distribution, we can write:

$$\langle(1-\beta\mu)^2\rangle = 1 + \frac{1}{3}\beta^2 \tag{3.53}$$

Now, Equation 3.52 becomes:

$$U_{rad}^{'} = \gamma^2(1+\frac{1}{3}\beta^2)U_{rad}, \tag{3.54}$$

where $\rm U_{rad} = \int m_e c^2 \epsilon_0 n_{ph}(\epsilon_0)d\epsilon_0$. Now, the angle-averaged Compton scattered power in the LF can be expressed as:

$$\frac{dE_1}{dt} = \sigma_T c U_{rad}^{'} = \sigma_T c \gamma^2 \left(1 + \frac{\beta^2}{3}\right) U_{rad} \tag{3.55}$$

The energy lost by the electron can be obtained by subtracting the incoming power from the scattered power:

Inverse Compton Scattering of Angle-averaged Blackbody Photons

In the astrophysical realm, the general expressions for the Compton cross section can be simplified by considering two key factors: the target photon energy is typically small ($\epsilon_0 << 1$), and the electrons are relativistic ($\gamma >> 1, \beta \to 1$). This relativistic condition, in particular, implies that the incident photon in the ERF travels in a direction very close to opposite to the electron momentum due to relativistic aberration determined by

$$\cos\theta'_{ph} = \frac{\cos\psi - \beta}{1 - \beta\cos\psi}, \tag{3.56}$$

Where θ'_{ph} is the angle between photon direction and electron travel direction in the ERF and ψ is the angle between the direction of propagation of incident photon and electron. In equation (3.56), when $\beta \to 1, \cos\theta'_{ph} \to -1$. This supports the head-on approximation that can conveniently simplify the Compton cross-section. So, we use the head-on approximation to streamline the Compton cross-section calculation, facilitating the derivation of the inverse Compton emissivity. Consequently, we arrive at an expression for the cooling term associated with inverse Compton scattering in the context of an angle-averaged blackbody photon distribution. The incident electron causes the target photons to undergo upscattering, with the resulting scattered photons propagating in the direction of the incoming electron, i.e., $\Omega_{\rm s} = \Omega_{\rm e}$, where $\Omega_{\rm s}$ and $\Omega_{\rm e}$ represent the solid angles associated to the angular direction of the scattered photons and incident electrons, respectively. The Compton cross section in the Thomson regime and the head-on approximation is given by

$$\frac{d\sigma}{d\Omega_s d\epsilon_s} = \sigma_T \delta(\epsilon_s - \gamma^2\epsilon_0)\delta(\Omega_s - \Omega_e)H(1 - \epsilon_0\gamma) \tag{3.57}$$

Here, H represents the Heaviside step function, which is defined as

$$H(x-a) = \begin{cases} 1 & \text{if } x - a > 0 \\ 0 & \text{if } x - a < 0 \end{cases}$$

and represents a sharp cut-off at the transition from the Thomson to the Klein-Nishina regime. The Heaviside function ensures Thomson scattering by limiting the integral to situations where $1 - \epsilon_0\gamma > 0$, implying that $\epsilon_0 < 1/\gamma$. The expression for the emissivity of Compton-scattered blackbody photons, considering the normalized photon temperature $\theta = \frac{\rm K_B T}{\rm m_e c^2}$, resulting from the interaction with a single electron, is as follows:

$$\mathrm{j}^{\text{head-on}}(\gamma, \epsilon_0, \theta) = \sigma_T m_e c^3 \epsilon_s \int_0^\infty n_{ph}(\epsilon_0, \theta)\delta(\epsilon_s - \epsilon_0\gamma^2)\delta(\Omega_s - \Omega_e)d\epsilon_0 \tag{3.58}$$

The spectral photon density of the isotropic blackbody radiation field, n_{ph}, is defined as:

$$n_{\rm ph} = K\frac{\epsilon_0^2}{\exp(\frac{\epsilon_0}{\theta}) - 1}, \tag{3.59}$$

where $K = \frac{8\pi}{\lambda_C^3}$. Consequently, Equation 3.58 becomes:

$$\mathrm{j}^{\text{head-on}}(\gamma, \epsilon_0, \theta) = \sigma_T\ m_e c^3 \epsilon_s\ K\ \delta(\Omega_s - \Omega_e) \int_0^\infty \frac{\epsilon_0^2}{\exp(\frac{\epsilon_0}{\theta}) - 1}\delta(\epsilon_s - \epsilon_0\gamma^2)\ d\epsilon_0 \tag{3.60}$$

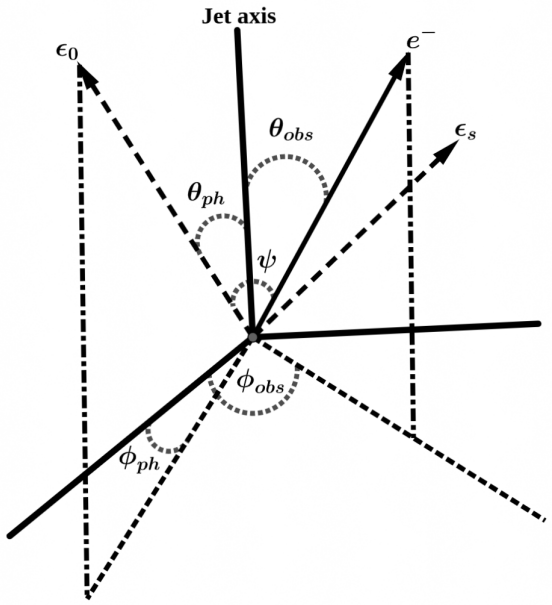

Figure 3.7: Various angles in spherical geometry depicting Compton upscattering of photons with energy ϵ_0 to ϵ_s off electrons with energies γ. Adopted from Chand and Böttcher (2024)

Utilizing the delta function to solve the integral, Equation 3.60 results in the expression:

$$\mathrm{j}^{\text{head-on}}(\gamma, \epsilon_s, \theta) = \sigma_T m_e c^3 K \delta(\Omega_s - \Omega_e) \frac{1}{\gamma^6} \frac{\epsilon_s^3}{\exp(\frac{\epsilon_s}{\gamma^2 \theta}) - 1} \tag{3.61}$$

Equation 3.3.4 can be integrated with respect to ϵ_s utilizing a standard integration formula[1]. This integration yields the radiation cooling term for inverse Compton scattering of a relativistic electron in an isotropic blackbody photon field under Thomson scattering conditions.

$$-\left(\frac{d\gamma}{dt}\right)_{\text{IC}} = \int_0^\infty \mathrm{j}^{\text{head-on}}(\gamma, \epsilon_s, \theta) d\epsilon_s = \frac{\pi^4}{15}\ \sigma_T\ m_e c^3 K \gamma^2 \theta^4 \tag{3.62}$$

Inverse Compton Scattering of Angle-dependent Blackbody Photons

The differential Compton cross-section can be approximated using the head-on approximation as

$$\frac{d\sigma}{d\Omega_s d\epsilon_s} = \delta(\Omega_s - \Omega_e) \frac{d\sigma}{d\epsilon_s} \tag{3.63}$$

The differential Compton cross section can be integrated over Ω_s to get

$$\frac{d\sigma_C}{d\epsilon_s} = \frac{\pi r_e^2}{\gamma \epsilon^{'}} \left(y + \frac{1}{y} - \frac{2\epsilon_s}{\gamma \epsilon^{'} y} + \left(\frac{\epsilon_s}{\gamma \epsilon^{'} y}\right)^2 \right) H\left(\epsilon_s\ ;\ \frac{\epsilon^{'}}{2\gamma}\ ,\ \frac{2\gamma \epsilon^{'}}{1 + 2\epsilon^{'}}\right), \tag{3.64}$$

[1]The standard integration formula: $\int_0^\infty \frac{x^3\ dx}{e^x - 1} = \frac{\pi^4}{15}$

where $\epsilon^{'} = \gamma\epsilon_0(1-\beta\cos\psi)$ is the photon energy in the ERF, and $y = 1-(\epsilon_s/\gamma)$. The emissivity of the electron is obtained by using the Compton cross section in equation (3.64) as:

$$\begin{aligned} \mathrm{j}_{\mathrm{C}}^{\text{head-on}}(\epsilon_s, \epsilon^{'}, \gamma) = \frac{3m_e c^3\sigma_T\epsilon_s(1-\beta\mu)}{8\gamma}\int_0^\infty \frac{1}{\epsilon^{'}}\Bigg\{y+\frac{1}{y} \\ -\frac{2\epsilon_s}{\gamma\epsilon^{'}y}+\left(\frac{\epsilon_s}{\gamma\epsilon^{'}y}\right)^2\Bigg\}\, n_{ph}(\epsilon_0,\theta) \\ H\left(\epsilon_s\ ;\ \frac{\epsilon^{'}}{2\gamma}\ ,\ \frac{2\gamma\epsilon^{'}}{1+2\epsilon^{'}}\right)d\epsilon_0 \end{aligned} \tag{3.65}$$

The cosine angle, $\mu = \cos\psi$, characterizes the interaction angle, which can be expressed as:

$$\mu = \mu_{obs}\ \mu_{ph} + \sqrt{1-\mu_{obs}^2}\sqrt{1-\mu_{ph}^2}\ \cos(\phi_{obs}-\phi_{ph}), \tag{3.66}$$

where $\mu_{\rm obs}$ and $\mu_{\rm ph}$ represent the cosines of the angles $\theta_{\rm obs}$ and $\theta_{\rm ph}$, respectively. Here, $\theta_{\rm obs}$ and $\theta_{\rm ph}$ indicate the angles made by the electrons and photons, respectively, with respect to the jet axis. Additionally, $\phi_{\rm obs}$ and $\phi_{\rm ph}$ correspond to the azimuth angles associated with the electrons and photons, respectively.

The mean photon energy of a blackbody radiation field is

$$\langle\epsilon_0(\theta)\rangle = \frac{\int_0^\infty d\epsilon_0\epsilon_0^3/\big(\exp(\epsilon_o/\theta)-1\big)}{\int_0^\infty d\epsilon_0\epsilon_0^2/\big(\exp(\epsilon_0/\theta)-1\big)} = \frac{\Gamma(4)\zeta(4)}{\Gamma(3)\zeta(3)} \cong 2.7\theta \tag{3.67}$$

Therefore, the peak of the blackbody radiation spectrum occurs at an average photon energy given by $<\epsilon_0(\theta)>= 2.7\theta$. The shape of the spectrum from IC scattering by non-thermal, relativistic electrons is typically dictated by the broad, non-thermal electron distribution, which is much broader than the relatively narrow thermal target photon distribution. This motivates why the exact shape of the target photon distribution is irrelevant. Hence, a monochromatic δ-function approximation can further simplify the spectral calculation to sufficient accuracy for a first exploration of the spectral and beaming patterns of such Compton emission (e.g., Dermer and Menon, 2009). Thus, the blackbody photon density can be approximated as

$$n_{ph}(\epsilon_0,\theta) = n_{ph}(\theta)\delta(\epsilon_0-2.7\theta) = 2.4K\theta^3\delta(\epsilon_0-2.7\theta) \tag{3.68}$$

With this simplification, the Compton emission coefficient in Equation (3.65) can be expressed as:

$$\begin{aligned} \mathrm{j}(\epsilon_s,\theta,\gamma) = \frac{0.3m_e c^3\sigma_T K\epsilon_s\theta^2}{\gamma^2}\Bigg[y+\frac{1}{y}-\frac{2\epsilon_s}{2.7y\gamma^2\theta(1-\beta\mu)} \\ +\frac{\epsilon_s^2}{(2.7)^2\gamma^4\theta^2(1-\beta\mu)^2y^2}\Bigg] \\ H\left(\epsilon_s;\frac{2.7\theta(1-\beta\mu)}{2},\frac{5.4\gamma^2(1-\beta\mu)\theta}{1+5.4\gamma\theta(1-\beta\mu)}\right) \end{aligned} \tag{3.69}$$

Equation (3.69) needs to be integrated over scattered photon energies, ϵ_s within the limits constrained by the Heaviside function to get the Compton cooling term. Equation (3.69) is the general expression for Compton emissivity that is applicable in both the Thomson

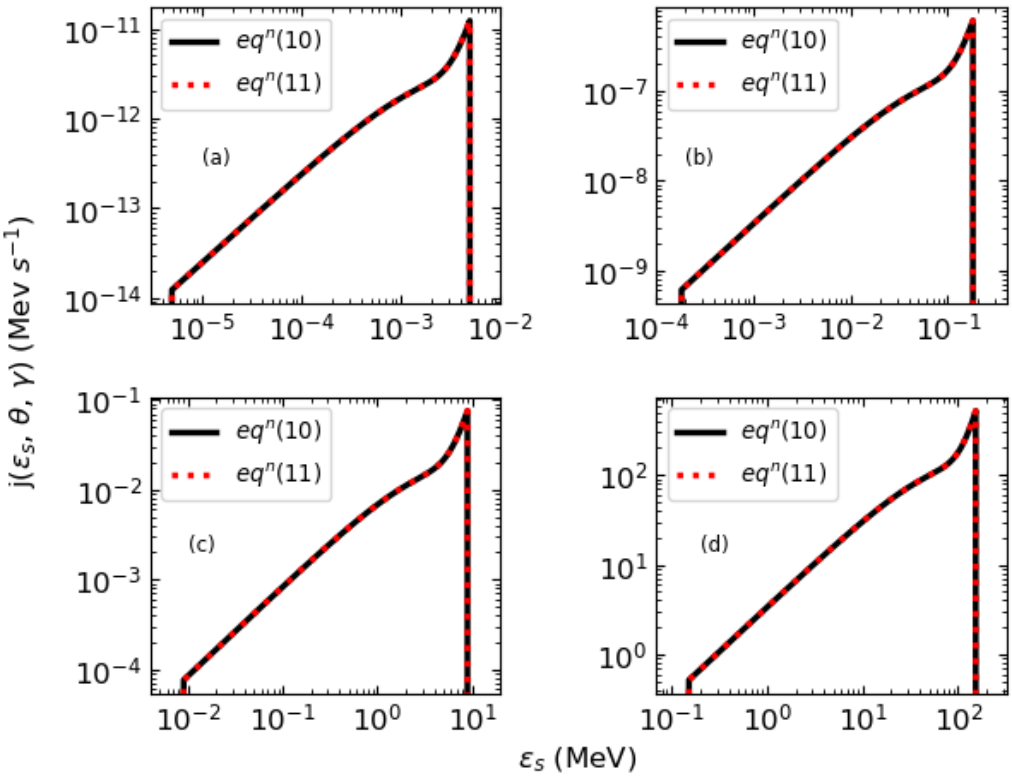

Figure 3.8: Comparison between equations (3.69) and (3.70), for $\gamma = 10^3$ and $\cos\psi = -1$: The top panels show the Compton emissivity due to a single electron vs. scattered photon energy for $\theta = 4.58 \times 10^{-10}$ (left) and $\theta = 10^{-8}$ (right), respectively, whereas the lower panels show the same for $\theta = 10^{-6}$ (left) and $\theta = 10^{-5}$ (right), respectively. Adopted from Chand and Böttcher (2024)

and Klein-Nishina regimes. The term $\mathrm{y} + 1/\mathrm{y}$ can be rewritten as $2 + \frac{\epsilon_s^2}{\gamma(\gamma-\epsilon_s)}$. In the Thomson regime, when $\epsilon^{'} << 1$, $\gamma >> \epsilon_s$ and $\gamma - \epsilon_s \cong \gamma$. In this limit, equation (3.69) can be simplified by binomially expanding the terms containing $(\gamma - \epsilon_s)$ as

$$\mathrm{j}(\epsilon_s, \theta, \gamma) = \frac{0.3 c \sigma_T K \theta^2}{\gamma^2}\left[2\epsilon_s + \epsilon_s\left\{\left(\frac{\epsilon_s}{\gamma}\right)^2 + \left(\frac{\epsilon_s}{\gamma}\right)^3 + ...\right\} - \frac{2}{2.7\theta(1-\beta\mu)}\left\{\left(\frac{\epsilon_s}{\gamma}\right)^2 + \left(\frac{\epsilon_s}{\gamma}\right)^3 + ...\right\} + \frac{1}{2.7^2\theta^2(1-\beta\mu)^2}\frac{1}{\gamma}\left(\frac{\epsilon_s}{\gamma}\right)^3\left\{1 + 2\left(\frac{\epsilon_s}{\gamma}\right) + 3\left(\frac{\epsilon_s}{\gamma}\right)^2 + 4\left(\frac{\epsilon_s}{\gamma}\right)^3 + ...\right\}\right] H\left(\epsilon_s \; ; \; \epsilon_{s_{min}}, \epsilon_{s_{max}}\right), \tag{3.70}$$

where $\epsilon_{s_{max}} = 5.4\gamma^2(1-\beta\mu)\theta/(1 + 5.4\gamma\theta(1-\beta\mu))$ and $\epsilon_{s_{min}} = 2.7\theta(1-\beta\mu)/2$ are the maximum and minimum energies of the upscattered photons. Equations (3.69) and (3.70) were compared to assess the impact of the binomial approximation. Figure 3.8 indicates that the approximation has no significant effect on the result for electrons with Lorentz factors of $\gamma = 10^3$, even when scattering UV target photons with $\mu = -1$. However, when dealing with higher values of γ and ϵ_0, it is essential to consider the higher order terms of the binomial expansion that contain $(\gamma - \epsilon_s)$ to avoid significant deviations from the full re-

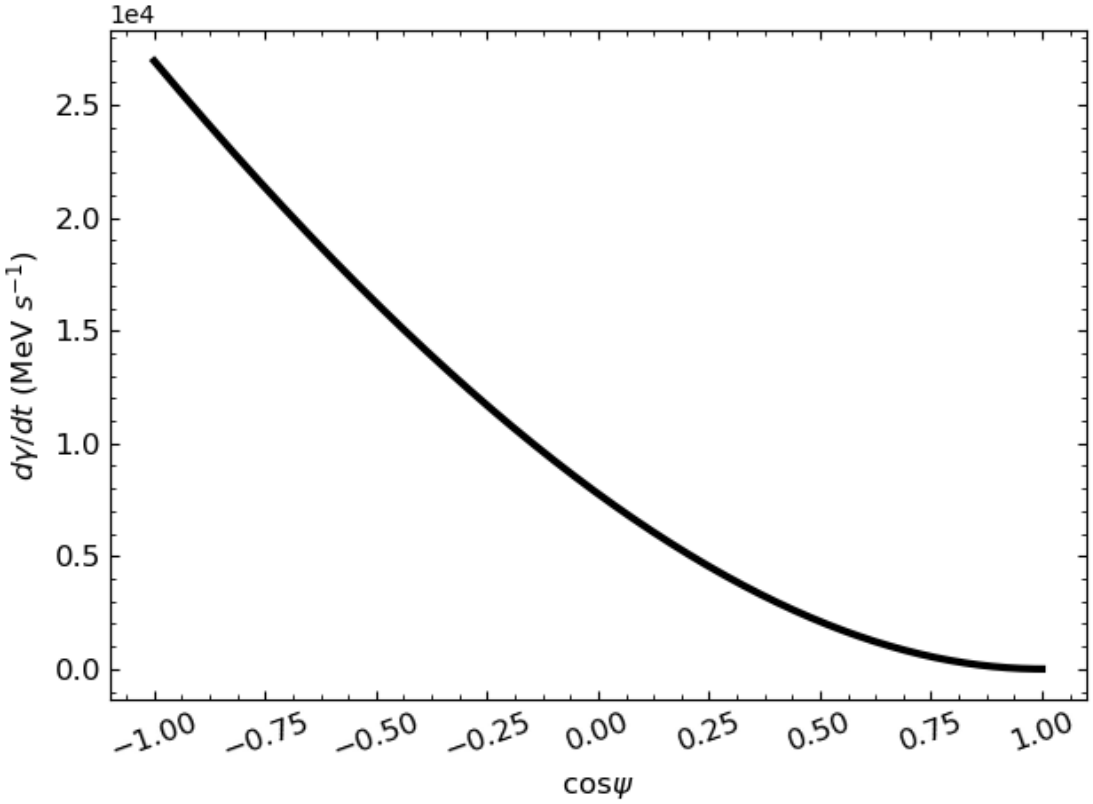

Figure 3.9: Variation of the cooling rate with the cosine of the collision angle ($\cos\psi$) at a Lorentz factor (γ) of 10^3 and radiation temperature (θ) of 10^{-5}: The figure illustrates that the maximum cooling occurs during head-on collisions between electrons and photons. Conversely, the minimum cooling is observed for tail-on collisions. Adopted from Chand and Böttcher (2024)

sults. Due to the presence of the Heaviside function in the emissivity equations, (3.69) and (3.70), a sudden drop in emissivity occurs beyond the scattered photon energy, $\epsilon_s = \epsilon_{s_{max}}$. By employing the aforementioned approximations, the integration of equation (3.70) over ϵ_s becomes feasible, considering the limits imposed by the Heaviside function. The cooling term associated with inverse Compton scattering, taking into account an angle-dependent photon field, can be expressed as

$$\frac{d\gamma}{dt}(\mu,\gamma,\theta) = A\Bigg[\left(\epsilon^2_{s_{max}} - \epsilon^2_{s_{min}}\right) + \frac{\epsilon^4_{s_{max}} - \epsilon^4_{s_{min}}}{4\gamma^2} + \frac{\epsilon^5_{s_{max}} - \epsilon^5_{s_{min}}}{5\gamma^3} - \frac{2}{B}\Bigg\{\frac{\left(\epsilon^3_{s_{max}} - \epsilon^3_{s_{min}}\right)}{3\gamma^2} + \frac{\epsilon^4_{s_{max}} - \epsilon^4_{s_{min}}}{4\gamma^3}\Bigg\} + \frac{1}{\gamma^4 B^2}\Bigg\{\frac{\epsilon^4_{s_{max}} - \epsilon^4_{s_{min}}}{4} + \frac{2\left(\epsilon^5_{s_{max}} - \epsilon^5_{s_{min}}\right)}{5\gamma} + \frac{\epsilon^6_{s_{max}} - \epsilon^6_{s_{min}}}{2\gamma^2} + \frac{4\left(\epsilon^7_{s_{max}} - \epsilon^7_{s_{min}}\right)}{7\gamma^3}\Bigg\}\Bigg], \tag{3.71}$$

where $A \equiv 0.3\ c\ \sigma_T K\theta^2/\gamma^2$ and $B \equiv 2.7\theta(1-\beta\mu)$. To calculate the cooling rate in the spine frame, a factor Γ_{rel}^2 needs to be added to the r.h.s. The angular distribution of inverse Compton scattering is described by Equation 3.66. These angles indicate the directions of the electron and photon relative to the jet axis. By assuming the azimuthal symmetry of the system and performing the numerical integration of equation (3.71) over μ_{ph}, the electron cooling rate can be obtained as a function of μ_{obs}. Figure 3.9 illustrates the dependency of the cooling rate on the cosine of ψ and θ_{obs}, highlighting the variation of the electron cooling rate with respect to these angular parameters. The plots are generated in the ELF at electron Lorentz factor of $\gamma = 10^3$ and the radiation temperature of $\theta = 10^{-5}$.

The total Compton power can be computed, and subsequently, the radiation spectra can be evaluated by considering an arbitrary distribution of electrons. For a comprehensive analysis of the detailed calculations of inverse Compton spectra in various scenarios, readers may refer Dermer and Menon (2009); Böttcher et al. (2012).

Chapter 4

Numerical Techniques:Kinetic Approach

4.1 Overview

Astrophysical plasmas, prevalent in high-energy environments like AGNs, GRBs, and SNRs, exhibit intricate behavior due to the interplay of charged particles and electromagnetic fields. Direct observations and lab experiments are often challenging. Thus, numerical simulations are crucial for understanding these phenomena. Plasma simulations in astrophysics utilize numerical techniques to study plasma dynamics. Simulations aid in validating theoretical models, exploring unobservable phenomena, predicting observational data, and studying cosmic accelerators. Utilizing methods such as Magnetohydrodynamics (MHD) and Particle-in-Cell (PiC) simulations facilitates the investigation of both large-scale structures and microphysical phenomena within various astrophysical environments.

In the kinetic simulations, a comprehensive mathematical representation of the system necessitates the incorporation of the Boltzmann equation
(Lifshitz and Pitaevskii, 1981)

$$\frac{\partial f_s}{\partial t} + \mathbf{v} \cdot \nabla f_s - \frac{q_s}{m_s}\left(\mathbf{E} + \frac{\mathbf{v}}{c} \times \mathbf{B}\right) \cdot \frac{\partial f_s}{\partial \mathbf{v}} = \left(\frac{\partial f_s}{\partial t}\right)_{\text{col}} \tag{4.1}$$

Equation 4.1 is a kinetic equation that describes the evolution of the distribution functions of charged particles $\mathrm{f_s(t; r, v)}$ for a specific plasma species s. Here, $\mathbf{r}$ and $\mathbf{v}$ indicate the 3-dimensional position vector and the three-velocity of the fluid or particle. The term $\frac{\partial f_s}{\partial \mathbf{v}}$ represents the gradient of the distribution function with respect to the velocity vector $\mathbf{v}$ and characterizes how the distribution function changes with variations in the velocity of the particle species in the phase space. The Landau collision integral $\left(\frac{\partial \mathrm{f_s}}{\partial \mathrm{t}}\right)_{\mathrm{col}}$ on the right-hand side of Equation 4.1 describes the evolution of a distribution function as a result of close encounters among charged particles, commonly known as Coulomb collisions. The electric ($\mathbf{E}$) and magnetic ($\mathbf{B}$) fields in Equation (1.1) are representative of self-

consistent fields arising from external sources and the collective motion of charged particles within the system. In practical applications, particularly in plasmas surrounding compact objects, Coulomb collisions exhibit much longer timescales compared to processes like particle gyration or acceleration. Such plasmas are often termed *collisionless*. Due to this characteristic, the right-hand side of Equation (1.1) is typically neglected in the context of collisionless plasmas. The resulting equation is referred to as the Vlasov equation (Vlasov, 1968).

$$\frac{\partial f_s}{\partial t} + \mathbf{v} \cdot \nabla f_s - \frac{q_s}{m_s}\left(\mathbf{E} + \frac{\mathbf{v}}{c} \times \mathbf{B}\right) \cdot \frac{\partial f_s}{\partial \mathbf{v}} = 0 \tag{4.2}$$

Equation 4.2 must now be coupled with Maxwell's equations governing the electromagnetic fields $\mathbf{E}(\mathrm{t}; \mathbf{r})$ and $\mathbf{B}(\mathrm{t}; \mathbf{r})$.

$$\nabla \times \mathbf{E} = -\frac{1}{c}\frac{\partial \mathbf{B}}{\partial t} \tag{4.3}$$

$$\nabla \times \mathbf{B} = \frac{1}{c}\frac{\partial \mathbf{E}}{\partial t} + \frac{4\pi}{c}\mathbf{j} \tag{4.4}$$

Here, the current density, $\mathbf{j}$ is self-consistently controlled by the motion of individual particles within a closed system and is given by

$$\mathbf{j} = \sum_s q_s \int \mathbf{v} f_s \, d^3\mathbf{v}. \tag{4.5}$$

If, at a certain initial time $t = t_0$, the initial conditions satisfy the two remaining Maxwell's equations, it can be shown that the solutions to Equations 4.3 and 4.4 will also satisfy the remaining two Maxwell's equations and subsequently, we can treat them as initial conditions.

$$\nabla \cdot \mathbf{E} = 4\pi\rho \tag{4.6}$$

$$\nabla \cdot \mathbf{B} = 0 \tag{4.7}$$

Here, ρ represents the charge density, defined as:

$$\rho = \sum_s q_s \int f_s \, d^3\mathbf{v}. \tag{4.8}$$

these conditions ensure a consistent and physically meaningful starting point for the simulation. The charge density ρ is determined by summing the charge of particles from all species (s) at each spatial point and integrating over velocity space. The system of equations from 4.2 to 4.5 lacks a general solution owing to its non-linear coupling. In practical applications, achieving a numerical solution for this system, even when discretized in both phase space and time, poses a significant computational challenge. The collisionless Vlasov-Maxwell description of the plasma introduces natural units for length scales ($c/\omega_{p,e}$), time scales ($\omega_{p,e}^{-1}$), and electromagnetic fields ($m_s \; c \; \omega_{p,e}/q_s$), where $\omega_{p,e} = \sqrt{4\pi n e^2/m_e}$ denotes the plasma frequency. The discretization must be carried out in a 6+1-dimensional space, leading to a computational cost that scales with the resolution to the sixth power. To mitigate this computational burden, various approaches and assumptions are employed to reduce the complexity of the problem. One such approach is the PiC algorithm, which we utilize in our work.

4.2 Particle-in-Cell Approach

Over the last few decades, researchers have found Particle-In-Cell (PIC) codes to be highly reliable and successful in conducting kinetic plasma simulations (e.g., Dawson, 1983; Birdsall, 1991; Villasenor and Buneman, 1992). Figure 4.1 illustrates the essential steps of the particle-in-cell algorithm. In the PiC algorithm, the approach involves sampling the distribution function itself with a finite number of macro-particles "p" as an ensemble for each species "s", instead of discretizing the phase space. Each macro-particle is characterized by continuous values for both coordinate and velocity. Consequently, at any given instant of time, the distribution function can be represented as:

$$f_s(t;\mathbf{r},\mathbf{v}) = \sum_p w_{s,p} S\left(\mathbf{r}-\mathbf{r}_{s,p}(t)\right)\delta\left(\mathbf{v}-\mathbf{v}_{s,p}(t)\right) \tag{4.9}$$

Here, $\mathbf{r}_{s,p}(t)$ and $\mathbf{v}_{s,p}(t)$ denote the coordinate and velocity of the p^{th} macro-particle belonging to species s, and $w_{s,p}$ represents the effective weight. The shape function S, characterizing the smearing of individual particles, exhibits symmetry and adheres to the condition:

$$\int S(\mathbf{r}-\mathbf{r}_{s,p}(t))\, d\mathbf{r} = 1 \tag{4.10}$$

where $\mathbf{r}$ represents the coordinates of the grid. Commonly used shapes are spline functions with orders up to $n \leq 4$. It is essential to ensure that the shape functions cover an adequate number of grid points to reduce numerical noise and prevent numerical heating. However, the number of points should be balanced to avoid excessive computational costs. Each macro-particle is treated individually, and its equation of motion can be independently integrated. The equations governing the motion of each macro-particle are expressed as follows:

$$\frac{d\mathbf{x}_{s,p}}{dt} = \mathbf{v}_{s,p} \tag{4.11}$$

$$\frac{d\mathbf{u}_{s,p}}{dt} = \frac{1}{m_s}\mathbf{F}_{s,p} \tag{4.12}$$

In these equations, $\mathbf{F}_{s,p}$ denotes the total force acting on the particle, and $\mathbf{u}_{s,p}$ represents the spatial components of the particle's four-velocity, specifically defined as $\mathbf{u}_{s,p} = \mathbf{v}_{s,p}\gamma_{s,p}$, where $\gamma_{s,p}$ represents the Lorentz factor of the particle (macro-particle). In this particular context, $\mathbf{F}_{s,p}$ signifies the Lorentz force arising from the collective electromagnetic field.

The electromagnetic fields are obtained by interpolating the fields at the particle positions.

$$\mathbf{E}_{s,p} = \int d\mathbf{x}\, \mathbf{E}(\mathbf{x})\, S(\mathbf{x}-\mathbf{x}_{s,p}(t)) \tag{4.13}$$

Similarly, the expression holds for $\mathbf{B}_{\mathrm{s,p}}$. The advancement of particles is achieved by solving the equation of motion. The interaction between particles and electromagnetic fields occurs through two mechanisms. Firstly, individual macroparticles deposit currents on the grid denoted as $\mathbf{j}_{s,p;i,j,k}$. The deposition algorithm is typically designed to be charge conservative, ensuring that the deposited currents satisfy the discretized charge continuity equation:

$$\frac{\partial \rho}{\partial t} + \nabla \cdot \mathbf{j} = 0 \tag{4.14}$$

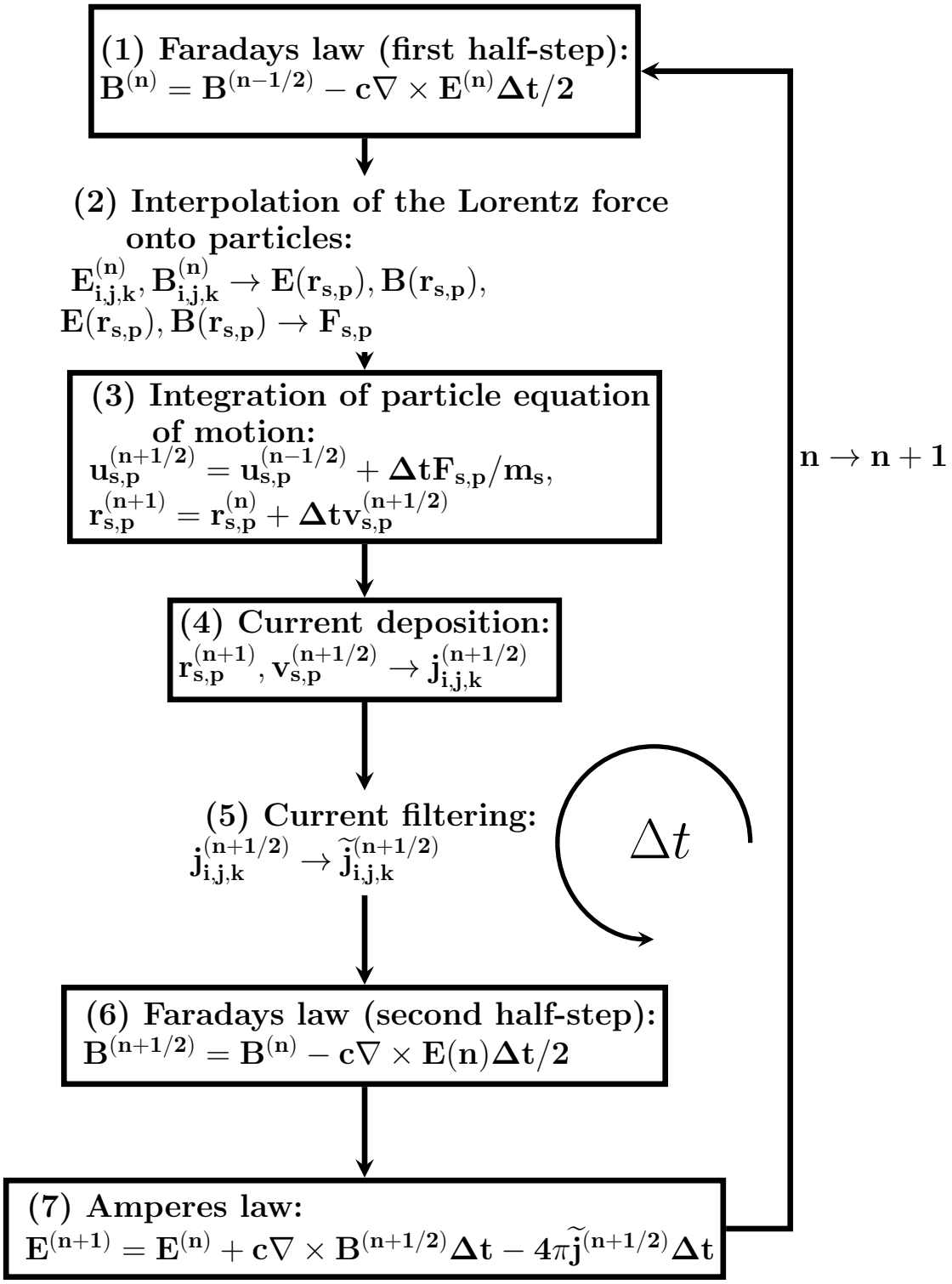

Figure 4.1: Illustration of essential steps in the PiC plasma simulation algorithm and the computational cycle process.

This discretized current, summed over all species and particles, serves as a source term in Amperes law (Equation 4.4). Ampere's law, in conjunction with Faraday's law (Equation 4.3), is then employed to advance the electric and magnetic fields over time. Conversely, electromagnetic fields exert an influence on particles through the Lorentz force:

$$\mathbf{F}_{s,p} = q_s \left(\mathbf{E}(\mathbf{r}_{s,p}) + \frac{\mathbf{v}_{s,p}}{c} \times \mathbf{B}(\mathbf{r}_{s,p}) \right) \tag{4.15}$$

This force is incorporated into the equations of motion for each individual particle (Equations 4.11 and 4.12), thus completing the algorithmic loop.

In addition to the previously discussed features, the PiC codes incorporate current filtering (step-5 in Figure 4.1) to alleviate noise arising from the finite number of macroparticles per simulation cell. Particle advancement is achieved by solving the equation of motion (4.11 and 4.12). A widely adopted method for this purpose is the Boris leap-frog pusher (Boris, 1970), expressed as follows:

$$\frac{\mathbf{x}^{n+1} - \mathbf{x}^{n}}{\Delta t} = \mathbf{v}^{n+1/2} \tag{4.16}$$

$$\mathbf{F}^{n+1/2} = \frac{\mathbf{p}^{n+1/2} - \mathbf{p}^{n-1/2}}{\Delta t} = q_s \left(\mathbf{E}^{n} + \mathbf{v}^{n+1/2} + \mathbf{v}^{n-1/2} \times \frac{\mathbf{B}^{n+1/2} + \mathbf{B}^{n-1/2}}{2} \right), \tag{4.17}$$

where the subscript $n+1$ pertains to the updated quantities calculated at time step $t_{n+1} = t_n + \Delta t$. The discretized values of electric and magnetic fields, denoted as $\mathbf{E}_{i,j,k}$ and $\mathbf{B}_{i,j,k}$, respectively, are spatially defined, where i, j, k represent the three-dimensional indices of the corresponding nodes in the discretized space known as Yee mesh configuration (Yee, 1966). Figure 4.1 illustrates the complete set of discretized equations, often referred to as the electromagnetic PiC algorithm. These equations approximate the solution of the system of hyperbolic Equations 4.2, 4.3, and 4.4, coupled via closure 4.5. The numerical solution attains second-order accuracy in time and approaches an analytic solution when the timestep is suitably short, $\mathrm{c}\Delta\mathrm{t} < 0.45\Delta\mathrm{x}$, in our simulation setup. In this context, Δx signifies the uniform cell size across all dimensions, and Δt represents the simulation timestep. This condition is known as the Courant-Friedrichs-Lewy (CFL) condition. The equations locally conserve charge, $\nabla \cdot \mathbf{B}$, and the spatial components of the total four-momentum (computed for both fields and particles). However, due to its explicit nature, the total energy is conserved only up to the second order in Δt.

4.3 The ACRONYM Code

In the nascent phase of my Ph.D. journey, I employed the `ACRONYM` code (Kilian et al., 2012) to generate preliminary results concerning self-generated electric and magnetic fields within initially unmagnetized plasma, particularly in shear boundary layers. This section is dedicated to providing an exploration of the ACRONYM code, numerical challenges, its application, and the insights derived from its utilization. Drawing upon findings presented in a conference proceeding paper (Chand et al., 2019), we delve into the unique capabilities of the ACRONYM code, underscoring its contribution to the comprehensive narrative of my research endeavors.

4.3.1 Exploration of the ACRONYM Code

`ACRONYM` code is a C++ implementation that robustly supports both fully relativistic simulations in 3D (three dimensions in space as well as in velocity space) and 2.5D (two spatial dimensions and three in velocity space). It utilizes the Esirkepov (2001) scheme for current deposition and the Penn et al. (2003) push for particle updates. The integration of Maxwell's equations is achieved through explicit time stepping, with options including the original Yee (1966) algorithm or CK or CK5 as outlined in Vay et al. (2011), depending on user preference. Parallelization is accomplished through domain decomposition into cuboids on individual CPUs, utilizing MPI for essential next-neighbor communication. Output operations are parallelized using MPI I/O features, demonstrating scalability to over 100,000 CPUs (Kilian et al., 2012). The code maintains high parallelization efficiency through load balancing between CPUs, even in the presence of significant density gradients. Its modular design facilitates easy adaptation to a broad range of simulation setups.

We generated preliminary results from our study using the `ACRONYM` code, which are discussed below.

4.3.2 Self-generated E & B Fields in SBLs

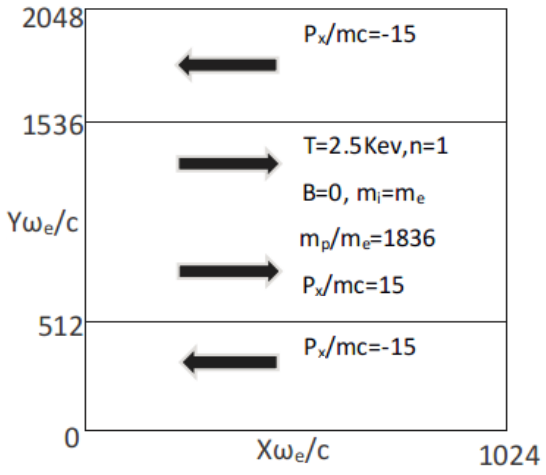

Figure 4.2: Simulation model configuration for shear boundary layers in radially stratified jets. Adopted from Chand et al. (2019).

In this sub-section, we present the results of PiC simulations depicting relativistic SBLs in initially unmagnetized plasma, conducted using the 2.5D `ACRONYM` code (Kilian et al., 2012). The initial conditions for our simulations are illustrated in Figure 4.2. The simulations are executed in the Equal Lorentz factor Frame of reference (ELF) with an initial bulk Lorentz factor of ($\Gamma = 15$).

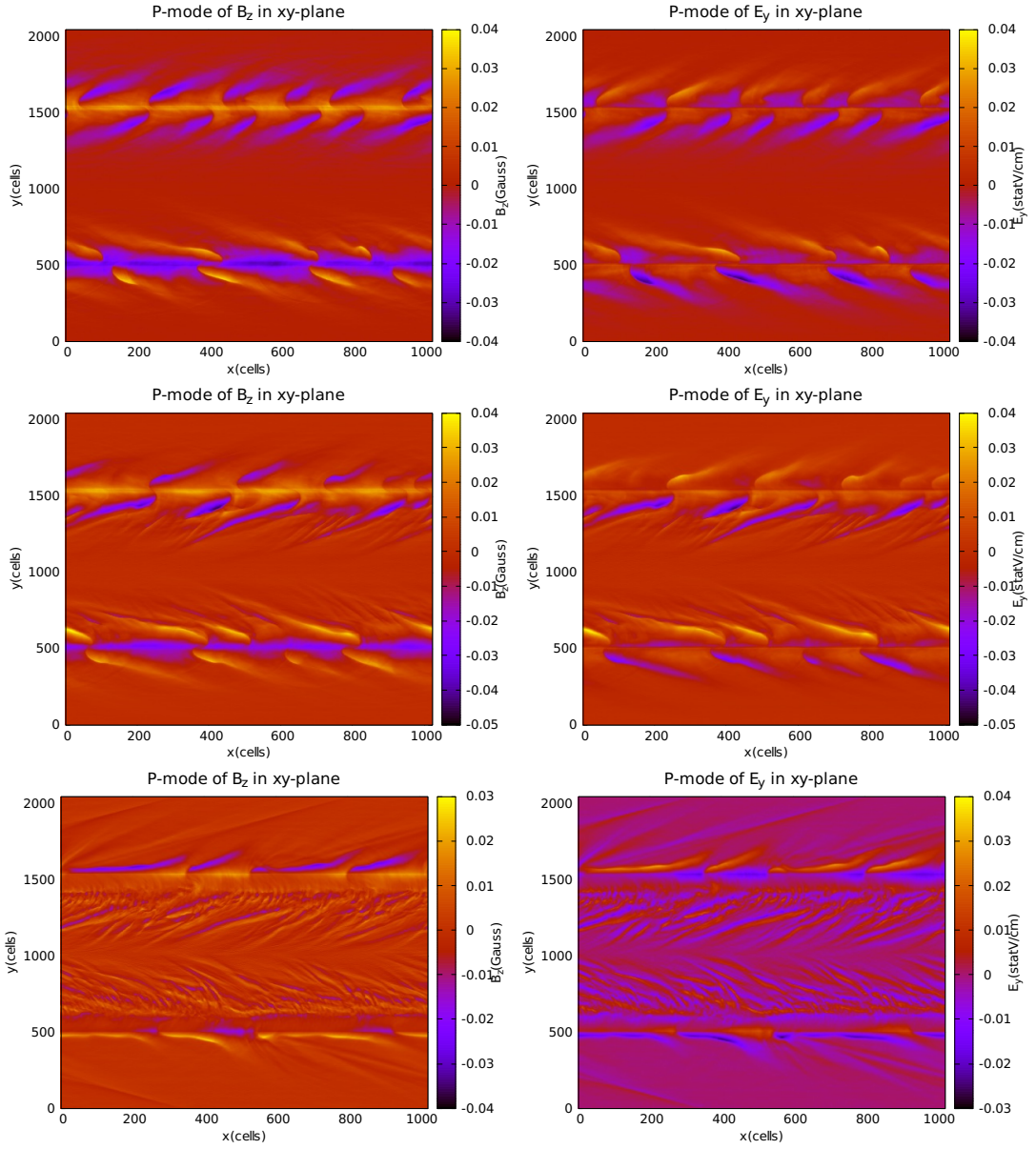

Figure 4.3: XY-cuts illustrating the self-generated electric and magnetic fields in SBLs with varying plasma compositions obtained at simulation time of $\omega_{p,e}t = 3000$: The top panel displays the self-generated magnetic and electric fields arising from a pure electron-ion plasma composition, while the middle panel exhibits the configuration in a hybrid plasma setting with 90% electron-ion and 10% pair plasma. The bottom panel shows the fields in a pure pair plasma composition. P modes are the 2D instabilities occurring in the $x - y$ plane. Adopted from Chand et al. (2019).

In this framework, the right-moving plasma, referred to as the spine and occupying the central 50% of the y-grid, moves with an equal but opposite velocity to the left-moving plasma, known as the sheath, which occupies the top 25% and bottom 25% of the y-grid. The simulation boxes have dimensions of 1024×2048, where the number of cells along the y-axis (L_y) $= 2\times$ the number of cells along the x-axis (L_x). The positron-electron mass ratio (m_i/m_e) is 1, while the proton-electron mass ratio (m_p/m_e) is maintained at

1836. The shear interfaces are positioned at $y = 512$ and $y = 1536$, respectively. Time is measured in units of $1/\omega_{p,e}$, where $\omega_{p,e}$ represents the electron plasma frequency, and all spatial distances are in units of the skin depth ($c/\omega_{p,e}$). The 2D instabilities in the $x - y$ plane are denoted as P modes, and those in the $y - z$ plane as T-modes. The longitudinal P-mode overwhelmingly dominates electromagnetic energy in the SBLs, while the transverse T-mode saturates at a very low level, contributing minimally to particle acceleration (Liang et al., 2017).

Recent PIC simulation findings illustrate the emergence of a self-generated magnetic field, possibly originating from plasma instabilities such as the Weibel instability (Weibel, 1959) and the two-stream instability (Boyd and Sanderson, 2003). This magnetic field development induces turbulence in SBLs of jets originating from initially unmagnetized shear flows, leading to particle energization (e.g., Liang et al., 2013b; Alves et al., 2012). Shear layer acceleration is anticipated to produce strongly angle-dependent lepton spectra, resulting in significantly enhanced forward boosting of the emission compared to the regular Doppler boosting effect (Liang et al., 2017). This phenomenon may offer a solution to the Lorentz factor crisis observed in Active Galactic Nucleus (AGN) jets (Lyutikov and Lister, 2010).

Figure 4.3 presents a comparative analysis of the 2D evolution of magnetic and electric field structures within shear boundary layers (SBLs) under various compositions of jet plasma. In the visual representation, blue and yellow colors denote opposite polarities. Notably, the triple layers formed at the interface exhibit a thinner profile in the case of a hybrid plasma configuration (Figure 4.3, middle panel) compared to the pure electron-ion plasma scenario (Figure 4.3, top panel). In the latter, wavy electromagnetic fields manifest outside the layers, providing additional channels for particle energization. The shear boundary layers exhibit heightened instability in the scenario of pure electron-positron plasma (Figure 4.3, bottom panel), whereas the presence of pure electron-ion plasma promotes the stability of SBLs to a greater extent (Figure 4.3, top panel). The color-coded visualization helps distinguish opposite polarities and highlights the structural variations in the evolving magnetic and electric fields.

4.3.3 Numerical Challenges

To ensure robust energy conservation in our simulations using `ACRONYM` code, we conducted multiple test runs with varying parameters such as box sizes, cell sizes, Particles Per Cell (PPC), Cells Per Skin depth (CPS), and field solvers. For these test runs, we employed a 2D generic plasma configuration. In this setup, the plasma frequency corresponds to an electron number density equivalent to 2 particles per cm^3, i.e., $\omega_{p,e} \cong 8 \times 10^4 s^{-1}$. This assumption is due to a code idiosyncrasy that assumes background and jet electrons occupy the same location. The results indicated that greater PPC and CPS values corresponded to improved energy conservation (see blue line in Figure 4.4). Taking into account these findings, the M 24 solver, an improved version of the standard Yee Maxwell solver, was

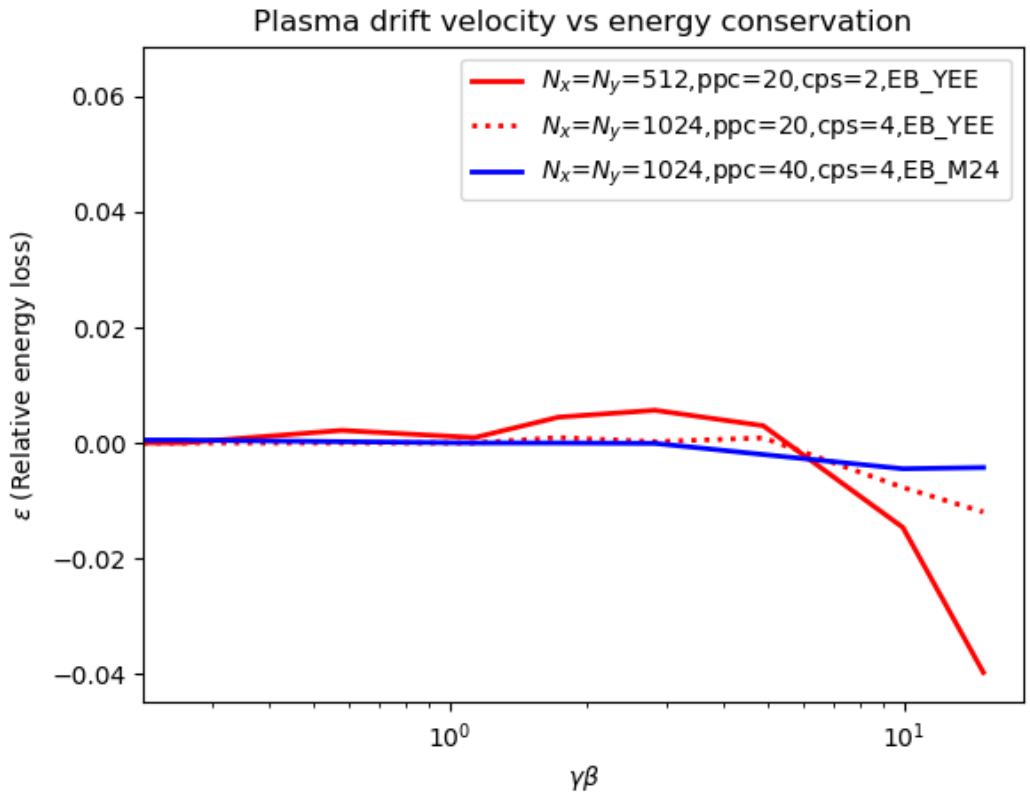

Figure 4.4: Energy conservation variation with plasma drift velocity. The plasma drift velocity in this context represents the velocity of the bulk motion of the plasma. The X-axis depicts the plasma drift velocity normalized by the speed of light and multiplied by the Lorentz factor, while the y-axis represents the relative energy loss. Adopted from (Chand et al., 2019).

selected for the results discussed in Section 4.3.2. This solver exhibits second-order accuracy in time and fourth-order accuracy in space (Hadi and Piket-May, 1997). While the PiC method is widely employed, it is susceptible to numerical instabilities that can yield unphysical simulation outcomes. Specifically, when the cell size (Δx) exceeds the Debye length (λ_D), it may lead to numerical heating and suboptimal energy conservation, a phenomenon known as finite grid instability (Birdsall, 1991). Typically, this issue is mitigated by resolving the Debye length, rendering it a relatively minor concern. The Numerical Cerenkov Instability (NCI) is a significant concern in PiC simulations that involve relativistic drifts. NCI is a computational artifact that arises in PiC simulations due to the discretization scheme employed. It is not a physical instability but a numerical phenomenon. In PiC simulations, electromagnetic fields and particle motions are discretized on a computational grid. When the discrete grid points interact with the chosen spatial and temporal resolutions, NCI occurs generating spurious wave modes. These modes can distort simulation results and potentially impact the accuracy of the physical processes under the study. The momentum plot of the magnetic field provides insight into the presence and effects of NCI. The electromagnetic field solver, M24 (Hadi and Piket-May,

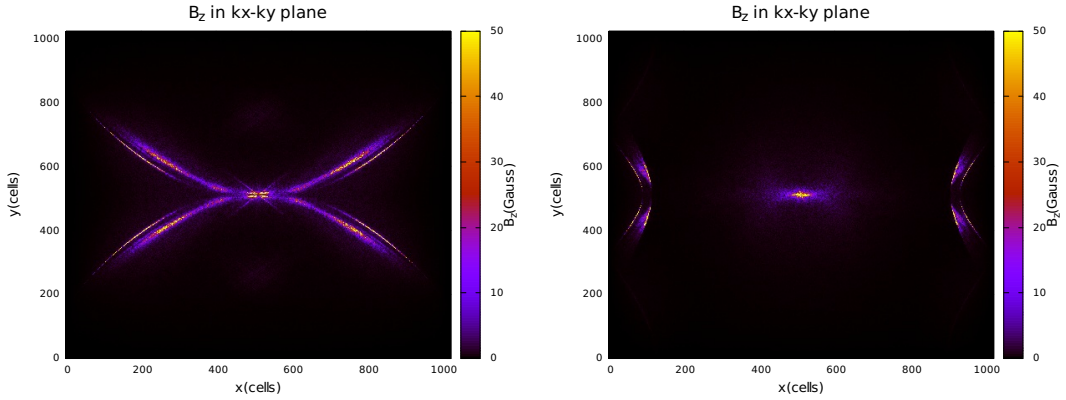

Figure 4.5: Comparison of 2D maps of B_z in the $k_x - k_y$ plane: The left panel displays B_z obtained with the ordinary Yee solver, while the right panel shows B_z obtained using the M24 Maxwell solver. Notably, the primary NCI mode present in the left plot is absent in the right plot. This highlights the effectiveness of the M24 solver in mitigating the NCI. Both plots are obtained at the simulation time of $t\omega_{p,e} = 3000$. Adopted from Chand et al. (2019).

1997), contributes to effective energy conservation and suppression of the NCI (Godfrey, 1974) (Figures 4.5). Additionally, the application of current smoothing and filtering techniques played a crucial role in enhancing energy conservation throughout the simulation run. Evaluating the spatial distribution of particle quantities within a macroparticle, referred to as the form factor, is vital for computational feasibility (Kilian et al., 2013). To ensure both physical realism and computational efficiency, we conducted test runs and determined that the Piecewise Quadratic Spline (PQS) form factor was the most suitable for our setup.

4.3.4 Conclusion

We conducted simulations to investigate the self-generation of electric and magnetic fields in SBLs of jets originating from initially unmagnetized plasma, employing a PiC code, `ACRONYM`. Rigorous testing, including the examination of the relativistic Cherenkov instability and other numerical instabilities, demonstrated significant suppression, ensuring excellent conservation of energy with deviations from the initial energy staying below 0.01% at all times. Our analysis of self-generated magnetic and electric fields unveiled the high instability of shear boundary layers in relativistic jets, particularly susceptible to both P and T modes in the case of electron-positron jet composition. In contrast, electron-ion jets exhibited mild stability, and remarkably stable and well-organized quasi-stationary electromagnetic fields were observed in such scenarios.

In the initial phase of my Ph.D. research, I started to work using the `ACRONYM` code; however, due to its lack of updates and challenges in implementing the radiation module, coupled with limited user support, I found it to be a less practical choice. The code had minimal user engagement, making problem-solving difficult. Recognizing the widespread

use and accessibility of TRISTAN-MP among computational astrophysicists, and considering its public availability and comprehensive user manual, I made the decision to transition from ACRONYM to TRISTAN-MP. This facilitated a more efficient and supported approach to my research objectives.

4.4 The TRISTAN-MP Code

In this section, we provide a brief overview of the TRISTAN-MP (Spitkovsky, 2005) code, a pivotal computational backbone that has been instrumental throughout the entirety of my Ph.D. research. This section offers a brief introduction to the code, while detailed results derived from its application are presented in other chapters of this thesis. TRISTAN-MP, an acronym for TRIdimensional STANford - Massively Parallel code, is a fully parallelized PiC code (Spitkovsky, 2005). Currently implemented in Fortran 95, the code follows a modular structure and utilizes MPI (e.g., Open MPI) and HDF5 libraries to facilitate parallelism and standardized parallel output files. As a fully relativistic PiC code designed for plasma physics computations, TRISTAN-MP rigorously solves the complete set of Maxwells equations in conjunction with the relativistic equations of motion for charged particles. Adhering to the general structure of PiC codes (e.g., Birdsall, 1991; Hockney and Eastwood, 1981), TRISTAN-MP discretizes fields on a finite 3D or 2D mesh, forming the computational grid. Subsequently, these fields drive the advancement of particle velocities over time through the Lorentz force equation. The derived charges and currents, based on particle velocities and positions, then serve as source terms for recalculating electromagnetic fields. Utilizing the positions and velocities of particles, the current is computed, serving as a crucial source term in Equation 4.4. Achieving self-consistent solutions for this set of equations involves initializing the electromagnetic fields and particles within the simulation box. This initialization ensures initially divergence-free Electric and Magnetic fields by placing electrons and ions or positrons (in our case, it is ions) at the same spatial positions.

4.4.1 Numerical Methods in Tristan-mp Implementation

In the numerical implementation of TRISTAN-MP, finite difference schemes play a pivotal role in both time and space domains, ensuring a second-order accuracy in both dimensions. Employing a 3D Yee mesh (Yee, 1966) for storing Magnetic and Electric fields, TRISTAN-MP utilizes a time-centered and space-centered approach. To interpolate the Electric and Magnetic fields to particle positions, a tri-linear interpolation function, characterized by linearity in each spatial dimension, is employed. Additionally, a three-point digital binomial filter (e.g., Birdsall, 1991; Hockney and Eastwood, 1981), with weights of 0.25, 0.5, and 0.25, is applied along each spatial dimension on the source terms for the field equations. This strategic implementation serves to suppress non-physical high-frequency field modes arising from the finite difference nature of derivative calculations.

Moreover, TRISTAN-MP provides the flexibility to choose between the regular second-order finite difference method and a fourth-order stencil (we chose it in our numerical setup), as proposed in Greenwood et al. (2004). The inclusion of the fourth-order stencil aims to mitigate the impact of the numerical Cerenkov instability. We employ the Boris pusher (Boris, 1970) for solving Equations 4.11 and 4.12.

4.4.2 Numerical Cerenkov Instability

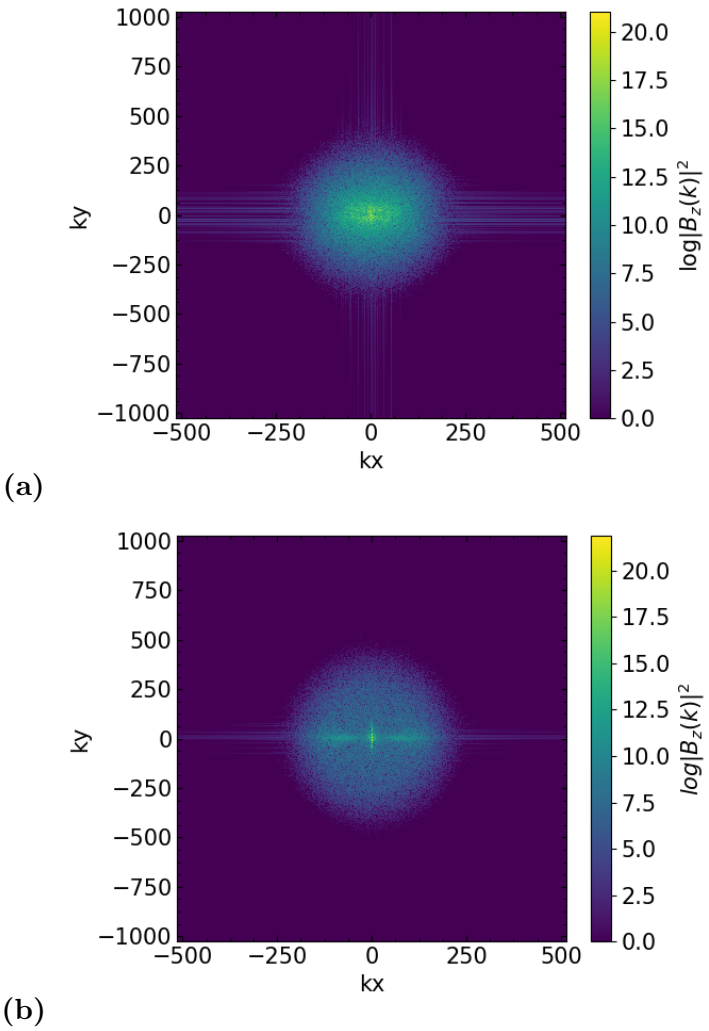

Figure 4.6: 2D color contour plots of the Fourier amplitude of B_z at two different sample times, (a) $t = 200\omega_{p,e}^{-1}$ and (b) $t = 3000\omega_{p,e}^{-1}$: It can be observed that the effects of the NCI are minimal in the simulation, and they tend to gradually decrease as the simulation progresses. Adopted from Chand and Böttcher (2024).

We examine a potential numerical Cerenkov instability that might manifest in the simulation results of TRISTAN-MP. We demonstrate that the NCI is effectively minimized in the code, and its influence on our simulation outcomes is deemed negligible. To mitigate the NCI, the TRISTAN-MP code incorporates a range of specialized numerical schemes that help suppress the instability as discussed in section 4.4.1. The code adheres to the

Aspect	**PiC Simulations**	**MHD Simulations**
Representation	Particles and Electromagnetic Fields	Fluids and Magnetic Fields
Equations of Motion	$\frac{d\mathbf{v}}{dt} = \frac{q}{m_e}(\mathbf{E} + \mathbf{v} \times \mathbf{B})$	$\rho\frac{d\mathbf{v}}{dt} = \mathbf{J} \times \mathbf{B} - \nabla P$
Coupling	Self-consistent coupling of particles and fields	MHD equations coupled to Ohm's law and thermodynamics
Spatial Scales	Applicable to kinetic scales (e.g., particle gyroradii, plasma skin depth, etc.)	Applicable to fluid scales (e.g., ion Larmor radii)
Applications	Focused on collisionless plasmas, includes backreaction from particles	Applicable mainly to weakly collisional or nearly collisional plasmas, considers MHD waves
Numerical Complexity	Particle motion requires smaller time steps	Fluid dynamics allows larger time steps
Kinetic Effects	Captures kinetic effects	Averaged fluid quantities, neglects kinetic effects
Advantages	Accurate for highly relativistic plasmas	Efficient for large-scale astrophysical systems
Challenges	Computationally much expensive, prone to numerical instability	Can not be employed to model the complex kinetic processes with high resolution

Table 4.1: Comparison of PIC and MHD Simulations

Courant-Friedrichs-Lewy (CFL) condition, ensuring that the product of the timestep and the speed of light is smaller than the minimum cell size. In this context, the speed of light is set as $c = 0.45\Delta x/\Delta t$. This also serves to mitigate the effects of the NCI. As a result, the current simulations are able to contain the NCI within acceptable levels, leading to minimizing adverse effects on particle heating. The $kx - ky$ plot in Figure (4.6) represents the distribution of the z-component of the magnetic field in momentum space, with kx and ky representing the wave numbers in the x and y directions, respectively. The smooth and well-behaved distribution of the magnetic field in the $kx - ky$ plot suggests a minimal effect of the NCI indicating that the chosen parameters in the simulations adequately mitigate numerical artifacts.

4.5 MHD vs. PiC Simulations

MHD and PiC simulations, both with their inherent strengths and limitations, provide unique perspectives on understanding plasma behavior. Table 4.1 illustrates a brief comparison of both numerical approaches. Both approaches have distinct advantages and applications, catering to different spatial and temporal scales of plasma dynamics. Recognizing these constraints, computational astrophysicists are increasingly turning to hybrid MHD-PiC simulations. By combining the strengths of both approaches, these simulations aim to provide a more comprehensive understanding of astrophysical plasma behavior, with a specific emphasis on elucidating the intricate interplay between particles and fluid dynamics, including the influential aspect of particles' backreaction on the overall system.

Chapter 5

Emergence of Self-Generated Electric and Magnetic Fields in SBLs and Particle Anisotropy

In this chapter, we begin with a discussion of the model setup and subsequently present simulation results obtained from the `TRISTAN-MP` code, pertaining to the emergence of electric and magnetic fields in initially non-magnetized plasma within SBLs. Additionally, we investigate particle densities in and around SBLs, examining the behavior of electrons and ions within these regions, leading to the formation of a triple layer composed of electrons, ions, and the transition layer between the spine and sheath. While the self-generation of fields within SBLs was briefly touched upon in Section 4.3 of Chapter 4, those were preliminary outcomes obtained using the `ACRONYM` code. This chapter offers a thorough explanation of the findings obtained through the use of the `TRISTAN-MP` code including the anisotropic momentum distribution of particles in SBLs of jets. The results of this chapter and the subsequent one (Chapter 6) have been published in the Astrophysical Journal (Chand and Böttcher, 2024).

5.1 Model Setup

In this section, we outline the physical and simulation setups employed to simulate SBLs within relativistic jets, specifically focusing on the plasma jet structures of spine-sheath configurations.

5.1.1 Physical Model

We set up a 2D PiC simulation of self-generation of $\vec{B}$ and $\vec{E}$ fields from initially unmagnetized plasma at SBLs in relativistic jets considering a spine-sheath plasma jet structure.

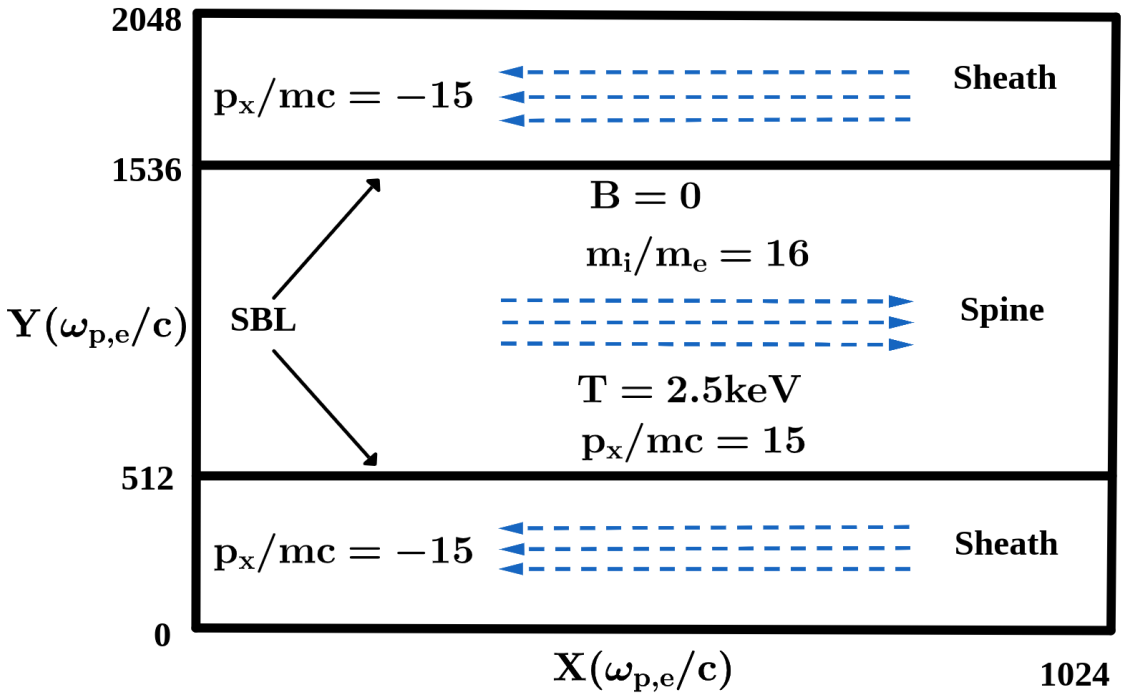

Figure 5.1: 2D simulation setup involving an electron-ion plasma with an initially unmagnetized shear flow: The plasma is composed of a central region in the Y-grid where right-moving plasma (spine) is located, where the top 25% and bottom 25% of the Y-grid are occupied by left-moving plasmas (sheath). The spine and sheath move in opposite directions with equal and opposite x-momenta $p_x/mc = \pm 15$ in the ELF. Adopted from Chand and Böttcher (2024).

The jet consists of two parts moving in opposite directions along the x-axis with the same velocity and Lorentz factor of $\Gamma = 15$. The spine moves in the positive x-direction while the sheath moves in the negative x-direction. The plasma has a uniform temperature of 2.5 keV. The simulations are carried out in the ELF with an initial bulk Lorentz factor ELF. Table 5.1 contains a list of the physical parameters that we use in our simulations.

5.1.2 Simulation Setup

We perform fully kinetic 2.5D electromagnetic PiC simulations using the `TRISTAN-MP` code (Spitkovsky, 2005). The rectangular computational domain we consider in the XY plane has periodic boundaries with a total of $L_x = 1024$ grid points in the x-direction and $L_y = 2L_x$ in the y-direction. All distances are measured in units of electron skin depth, $d_e = c/\omega_{p,e}$, where c is the speed of light and $\omega_{p,e} = \sqrt{4\pi n e^2/m_e}$ is the electron plasma frequency (n, e, and m_e represent electron number density, elementary charge, and electron mass, respectively). The simulation involves 20 particles per cell (PPC) per species with a reduced proton-to-electron mass ratio of $m_p/m_e = 16$, and the simulation time is measured

Table 5.1: Table of physical parameters: Adopted from Chand and Böttcher (2024).

Physical parameters	Values
Initial magnetic field (B)	0
Ion temperature ($K_B T_i$)	2.5 keV
Electron temperature ($K_B T_e$)	2.5 keV
Bulk Lorentz factor of the spine (Γ_{sp})	15
Bulk Lorentz factor of the sheath (Γ_{sh})	15

Table 5.2: Table of simulation parameters: Adopted from Chand and Böttcher (2024).

Simulation parameters	Values
PPC	20
Plasma skin depth (d_e)	10 Δx
m_i/m_e	16
Speed of light (c)	0.45 $\Delta x/\Delta t$
Correction factor for c	1.025
L_x	1024 Δx
L_y	2048 Δx
Plasma density (n_0)	PPC Δx^{-3}
Plasma frequency ($\omega_{p,e}$)	$0.045\Delta t^{-1}$
Spatial resolution (Δx)	0.1 d_e
Temporal resolution (Δt)	$0.045\omega_{p,e}^{-1}$

in terms of inverse plasma frequency ($1/\omega_{p,e}$). In PiC simulations of relativistic plasma, the use of a reduced m_p/m_e is a common practice to enhance computational efficiency and numerical stability. The large mass disparity between electrons and protons can lead to significant timestep discrepancies, where electrons require much smaller time steps than protons to accurately capture their dynamics. If we need to take the ion contribution into account, we should adjust the plasma frequency as $\omega_{p,e}^2 \rightarrow \omega_{p,e}^2(1+m_e/m_p)$. However, this modification is practically insignificant when dealing with the real m_p/m_e (e.g., Grismayer et al., 2013b). As we aim to study the underlying physics at electron scales and conduct analyses of simulation results covering time scales relevant to protons, utilizing the actual mass ratio is beyond our computational capabilities. Consequently, we opt for a reduced proton-to-electron mass ratio. PiC simulations have been employed to study magnetic field generation and particle acceleration within electron-proton plasmas in relativistic shear flows, considering both actual (e.g., Alves et al., 2014) and reduced (e.g., Grismayer et al., 2013a) mass ratios. We set the speed of light as $c = 0.45\Delta x/\Delta t$, where Δx and Δt are the spatial and temporal resolutions, respectively. A correction factor for the speed of light is introduced, which causes electromagnetic waves to travel a little bit faster than the maximum speed of the particles. This helps ultra-relativistic flows to avoid the numerical Cerenkov instability, enabling stable and accurate simulations (e.g., Spitkovsky, 2007; Sironi and Spitkovsky, 2009).

The right-moving spine plasma occupies the central 50% of the numerical Y-grid, while

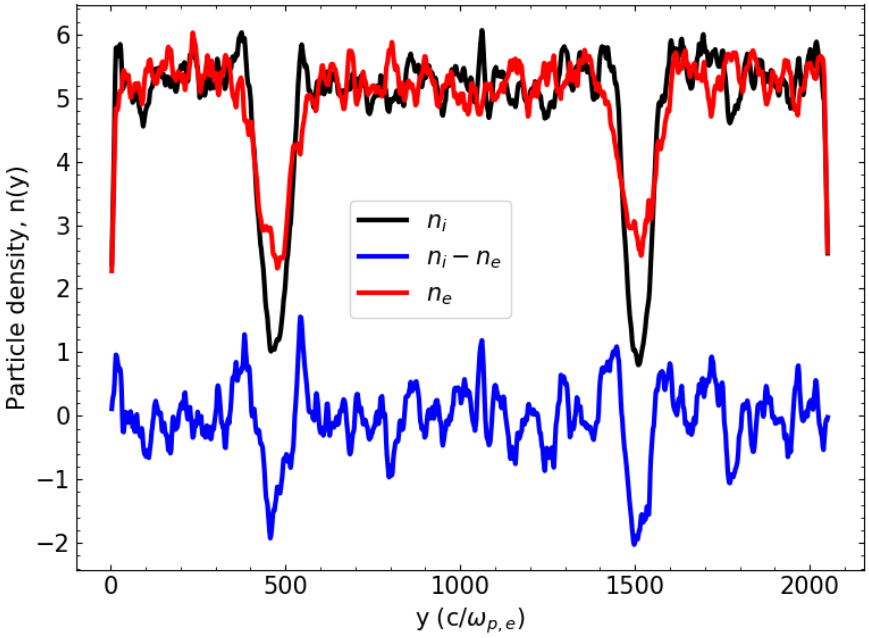

Figure 5.2: The electron number densities as a function of y at $t = 3000\omega_{\mathrm{p,e}}^{-1}$: while the ions are fully expelled from the shear interface, the electrons create a layer near the interface, resulting in the formation of a triple layer due to charge separation. Adopted from Chand and Böttcher (2024).

the left-moving sheath plasma occupies the lower and upper quarters of the Y-grid. The shear interfaces are located at Y = 512 and Y = 1536 of the simulation box. Table 5.2 summarizes the simulation parameters and their respective values used in this study.

5.2 Self-generated magnetic and electric fields

Plasma instabilities like the Weibel instability self-generate a magnetic field along the z-direction (perpendicular to the jet axis and parallel to the SBL). The self-generated electromagnetic fields in SBLs create turbulence in the spine-sheath interface, eventually leading to particle acceleration up to TeV energies in relativistic jets. Figures 5.3(a), 5.3(b), and 5.3(c) show the dominant components of electric and magnetic fields and the current density produced from the PiC simulation.

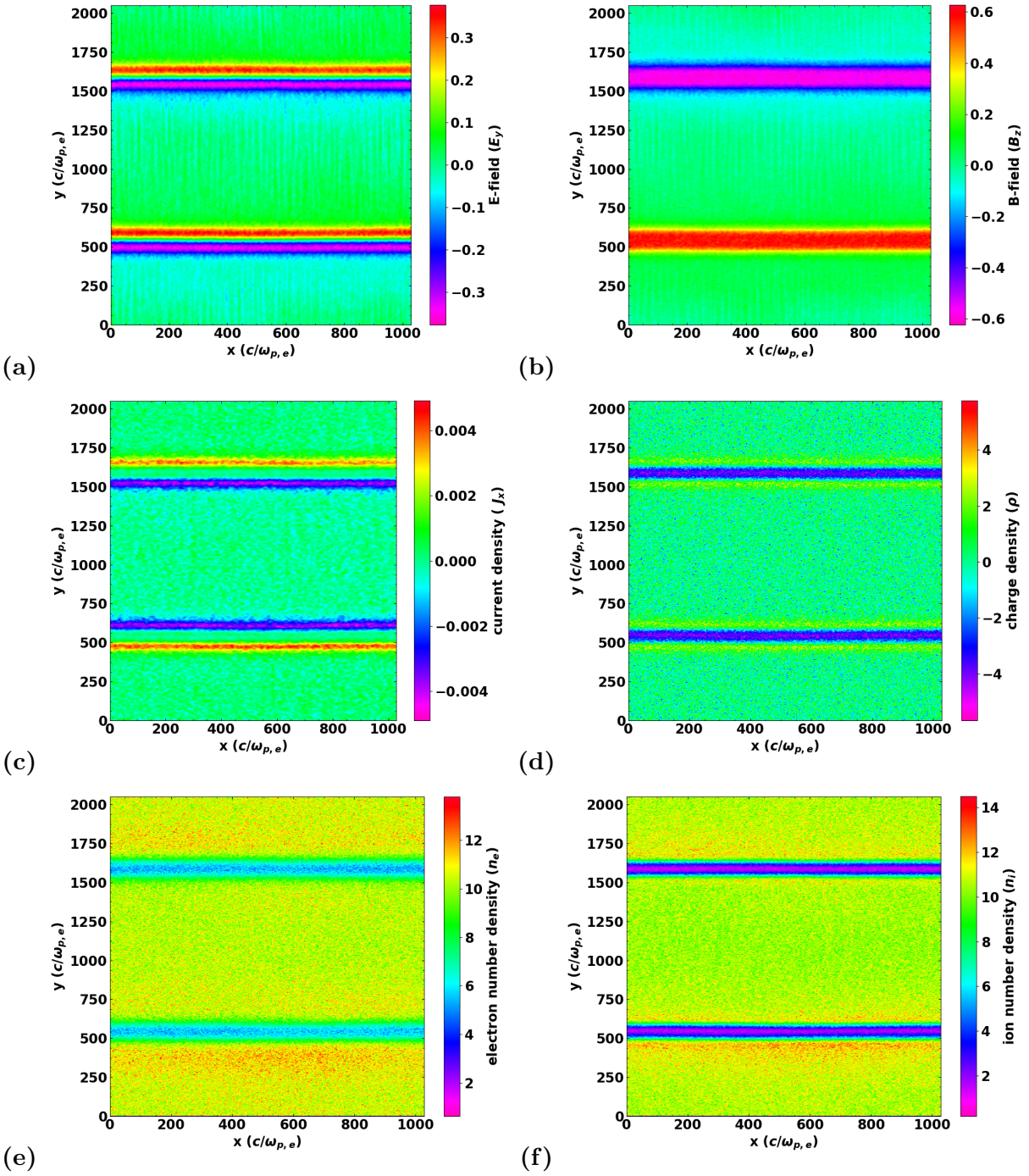

Figure 5.3: First row: Figure (a) illustrates the xy-cut of the self-generated electric field and Figure (b) presents the magnetic field in SBLs, with the red and magenta colors representing opposite polarities. Second row: Figure (c) depicts the current distribution (J_x). The ions dominate the stronger outer current sheet, while the weaker inner current sheet is dominated by electrons. Figure (d) shows the total charge density (ρ). Third row: Figures (e) and (f) respectively show the density distribution of electrons and ions. Notably, a discernible depletion in particle density is observed in the vicinity of the boundary layers. All figures correspond to $t = 3000\omega_{p,e}^{-1}$. The units displayed are arbitrary. Adopted from Chand and Böttcher (2024).

Figure 5.3(d) illustrates the net charge distribution in the SBLs, showing a notable concentration of negatively charged particles (electrons) within these regions. Positively charged particles (ions), on the other hand, tend to have a slightly more dispersed distribution and are found slightly further from the SBLs, thereby forming a triple-layer structure. Figures 5.3(e) and 5.3(f) present the spatial distribution of electron and ion number densities, respectively. These figures highlight higher electron density within the SBLs compared to the ion density. This disparity in densities is further evident in the density profiles of both species (Figure 5.2). The density profiles of ions, electrons, and net charge as a function of the y-coordinate are demonstrated in Figure 5.2. Due to the different velocities and densities of ions and electrons, the current density along the x-direction (J_x) (as depicted in Figure 5.3(c)) produces the uniform magnetic field (B_z) along the shear interface within the shear flows. Because the electron gyroradius is smaller than that of ions, ions are more displaced than electrons, leading to their expulsion from the shear interface due to the extra magnetic pressure, resulting in the formation of a density trough. This process induces charge separation and the formation of a triple layer, as illustrated in Figure 5.2. Ion-dominated current sheets are formed farther from the shear interface, while electron-dominated current sheets are formed near it, with an electric field (E_y) pointing from the ion-dominated current sheet to the electron-dominated current sheet. Ultimately, the electrons undergo efficient acceleration driven by the cross fields ($\vec{E}\times\vec{B}$) in the x-direction, which aligns with the jet-propagation direction. As the ions are more massive than electrons, ions undergo free streaming while electrons behave like fluid (e.g., Gruzinov, 2008; Liang et al., 2017). The kinetic KHI plays a vital role in initially cold electrons. However, the electrons attain a finite transverse momentum either by plasma instabilities or due to the finite temperature achieved by electrons. Eventually, electrons with finite transverse momentum cross over to the sheath moving in the opposite direction, but heavy ions do not. This mechanism, referred to as the electron counter-current instability (ECCI) (e.g., Liang et al., 2017), dominates, leading to the formation of opposite current layers on the two sides of the shear interface, creating a monopolar slab of magnetic field.

5.3 Particle Anisotropy in SBLs

In this section, we present electron phase plots, revealing a highly anisotropic momentum distribution of electrons. In order to illustrate the particle acceleration and radiation properties in the stationary (sheath) frame of the source, we Lorentz-transform the particle momenta into the sheath frame, utilizing a bulk Lorentz factor of $\Gamma = 15$.

$$p_{\mathrm{x,lf}} = \Gamma\left(p_{\mathrm{x,elf}} + \beta_\Gamma E_e/c\right), \tag{5.1}$$
$$p_{\mathrm{y,lf}} = p_{\mathrm{y,elf}}.$$

Here, p_{elf}, p_{lf}, and E_e represent the electron momenta in the ELF, lab frame, and the electron energy, respectively, with subscripts $x$and y indicating the momentum directions.

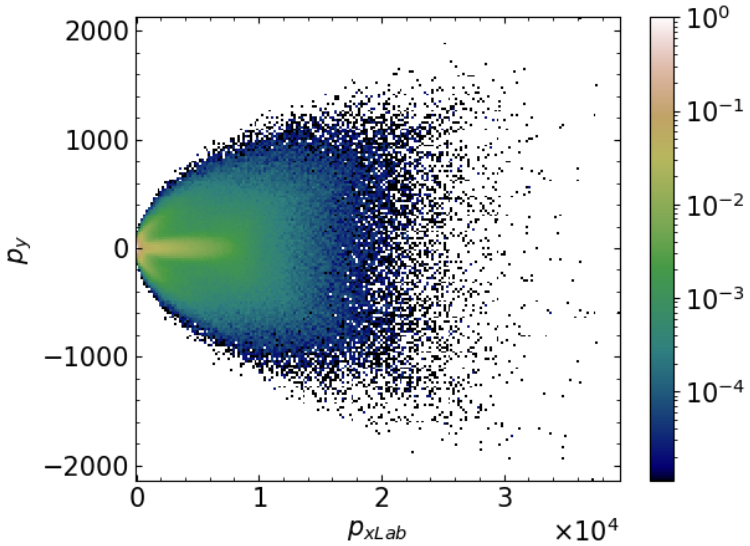

Figure 5.4: Spine electrons' p_y versus p_{xLab} at time $t = 3000\omega_{p,e}^{-1}$: p_x are Lorentz boosted to the Laboratory frame by $\Gamma = 15$. The figure illustrates that some of the spine electrons diffuse into the sheath region, leading to the deceleration of those spine electrons, represented by the low-energy arc-shaped electron population. The high-energy electron population towards the right-hand side of the figure corresponds to electrons that remain in the spine region without crossing over into the sheath region. Adopted from Chand and Böttcher (2024).

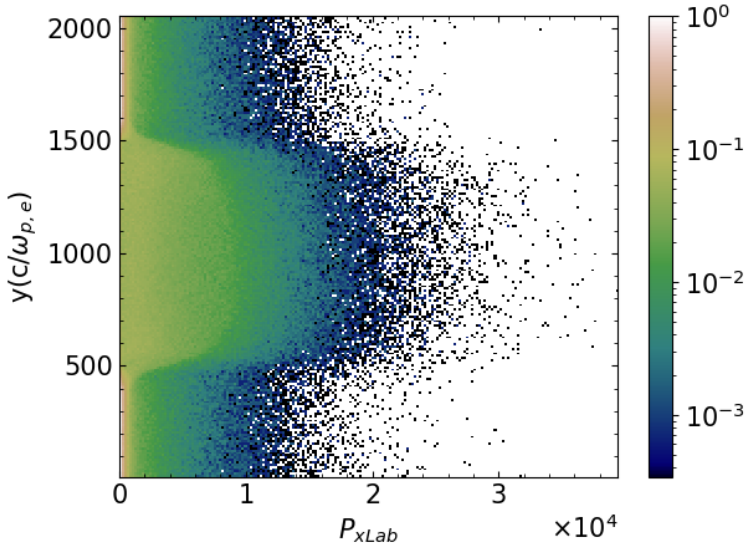

Figure 5.5: y $(c/\omega_{p,e})$ versus p_{xLab} of spine electrons at $t = 3000\omega_{p,e}^{-1}$: p_x are Lorentz boosted to the laboratory frame. As depicted in the figure, some of the spine electrons cross over through SBLs and enter the sheath region, where they experience deceleration. The spine electrons that remain strictly within the spine region undergo acceleration. Adopted from Chand and Böttcher (2024).

We can express Equation 5.1 in dimensionless form as:

$$\gamma_{\rm lab}\ \beta_{\rm lab,x} = \Gamma\left(\gamma_{\rm elf}\ \beta_{\rm elf,x} + \gamma_{\rm elf}\ \beta_{\Gamma}\right) \qquad (5.2)$$
$$\gamma_{\rm lab}\ \beta_{\rm lab,y} = \gamma_{\rm elf}\ \beta_{\rm elf,x}$$

Here, the quantities, $\rm p/m_e c = \gamma\beta$ represent the normalized momenta of the electron, $\gamma_{\rm elf}$ and $\gamma_{\rm lf}$ represent electron Lorentz factors in the ELF and the lab frame, respectively.

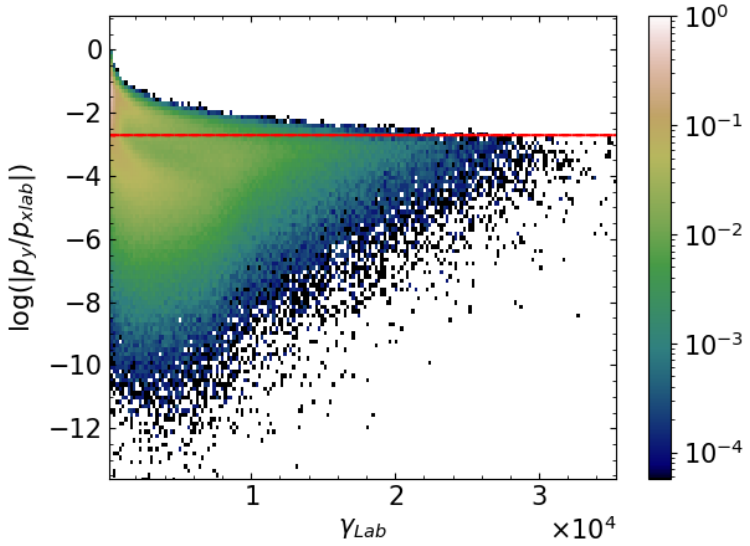

Figure 5.6: The distribution of the tangent of the beam angle of spine electrons versus electron Lorentz factor in the laboratory frame at $\rm t = 3000\omega_{p,e}^{-1}$: all high-energy spine electrons, which did not cross over to the sheath region, possess beam angles significantly smaller than $1/\Gamma$, as indicated by the red line. The figure further illustrates an anticorrelation between beam angle and electron energy. Adopted from Chand and Böttcher (2024).

The results demonstrate that spine electrons undergo significant acceleration, attaining high energies and exhibiting pronounced momentum anisotropy ($\rm p_{xlab} >> p_y$) in the laboratory frame (Figure 5.4). A portion of the spine electrons diffuses into the sheath region, experiencing deceleration and giving rise to a low-energy population, as depicted at the left in Figures 5.4 and 5.5. Moreover, Figure 5.5 illustrates the large particle momenta along the jet axis in the spine. Furthermore, we observe an anti-correlation between the beam angle $\rm |p_y/p_{xLab}|$ and electron energies, with the beam angle decreasing as electron energies increase (Figure 5.6).

Notably, the beam angles of all high-energy spine electrons, which remained in the spine region and did not transition to the sheath region, are significantly smaller than those resulting from Doppler boosting an isotropic particle distribution from the spine rest frame to the laboratory frame ($1/\Gamma$), as depicted by the red dashed line in Figure 5.6. This anisotropic distribution of electrons implies that radiation emitted from SBLs would exhibit strong beaming along the x-axis, even in the ELF.

5.4 Discussion and Outlook

In this chapter, we have explored the outcomes of simulating the self-generation of electric and magnetic fields within the SBLs of jets originating from initially unmagnetized plasma. Our investigation employed the PiC code, `TRISTAN-MP` (Spitkovsky, 2005). The focus of our study encompassed the self-generated electric and magnetic fields arising within relativistic SBLs in jets associated with AGNs and GRBs. We demonstrated that the development of plasma instabilities, such as the Weibel instability, leads to the self-generation of electric and magnetic fields, ultimately driving particle acceleration within the SBLs. As the electron gyroradius is smaller than that of ions, the ions experience greater displacement, causing their expulsion from the shear interface. This expulsion is attributed to the additional magnetic pressure, ultimately giving rise to the creation of a density trough. This sequence of events induces charge separation, leading to the formation of a triple layer. In the end, efficient acceleration of electrons occurs, propelled by the cross fields ($\vec{E} \times \vec{B}$) in the x-direction, aligning with the direction of jet propagation.

In future investigations, exploring the impact of weakly magnetized backgrounds with non-zero magnetization ($\sigma = B_0^2/(4\pi mnc^2)$, where B_0, m, and n denote the background magnetic field strength, particle mass, and particle density, respectively) on the stability of relativistic SBLs and the consequent particle spectra would be a compelling avenue of research. Utilizing the `TRISTAN-MP` code, our simulations have focused on SBLs within a pure electron-ion plasma composition. Our future investigations will extend to exploring alternative plasma compositions, such as pure pair plasma and hybrid configurations. We will leverage high-performance computing facilities to conduct an examination of simulation dimensionality and its consequential effects on plasma instabilities.

Chapter 6

Inverse Compton Emission and Cooling in Relativistic Jets' SBLs

In this chapter, we present the outcomes of our simulations investigating the impact of inverse Compton cooling on particle dynamics and the ensuing radiation spectra in SBLs of relativistic jets. We delve into the phenomenon of inverse Compton emission and the cooling process experienced by relativistic electrons. We explore how these factors shape the particle spectra and contribute to the formation of inverse Compton radiation spectra. Additionally, we address the observable features of the radiation spectra followed by the concluding section. The simulation configuration for the findings in this chapter is the same as in Chapter 5.

6.1 Electron Spectra and Effect of IC Cooling

While PiC simulations have been employed in numerous investigations to explore the impact of synchrotron cooling (e.g., Hakobyan et al., 2019) and IC cooling (e.g., Werner et al., 2018b) on relativistic jet particles within the context of magnetic reconnection, including the resultant radiation spectra, the influence of radiation drag on radiating particles and its implications for the resulting radiation spectra remain largely unexplored in studies of particle acceleration at SBLs in jets. Despite the potential for radiative cooling to significantly affect particle dynamics, a comprehensive understanding of the interplay between radiation drag and particle acceleration processes at the site of relativistic jets' SBLs is yet to be elucidated.

This section focuses on electron acceleration with PiC simulations demonstrating the impact of IC cooling on particle spectra. Initially, the energy distribution of electrons follows a Maxwellian distribution. Acceleration occurs due to the electromagnetic field generated by the relative displacement of ions and electrons. The thermal electron bulk Lorentz factor reaches its peak when energy equipartition between the ions and electrons is attained

(e.g., Lyubarsky, 2006; Iwamoto et al., 2019).

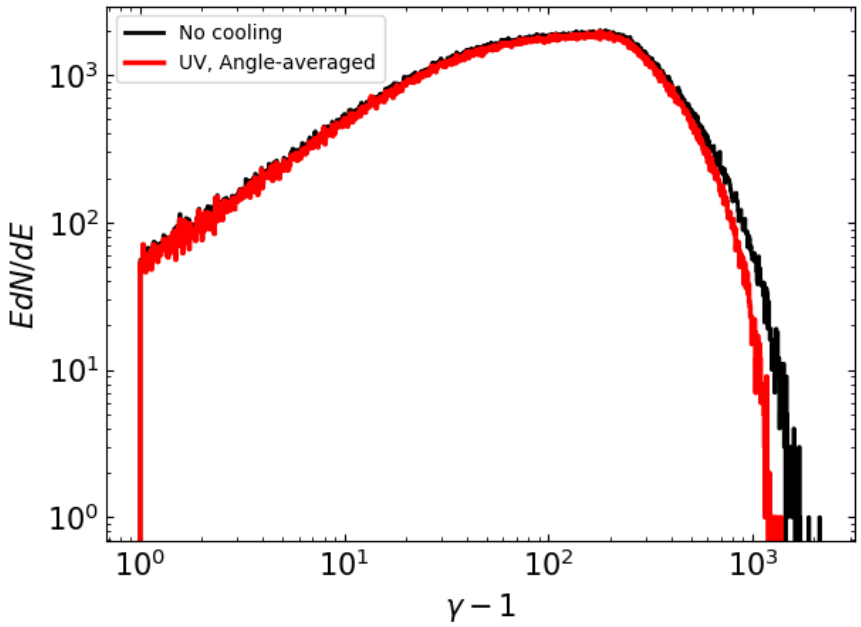

(a)

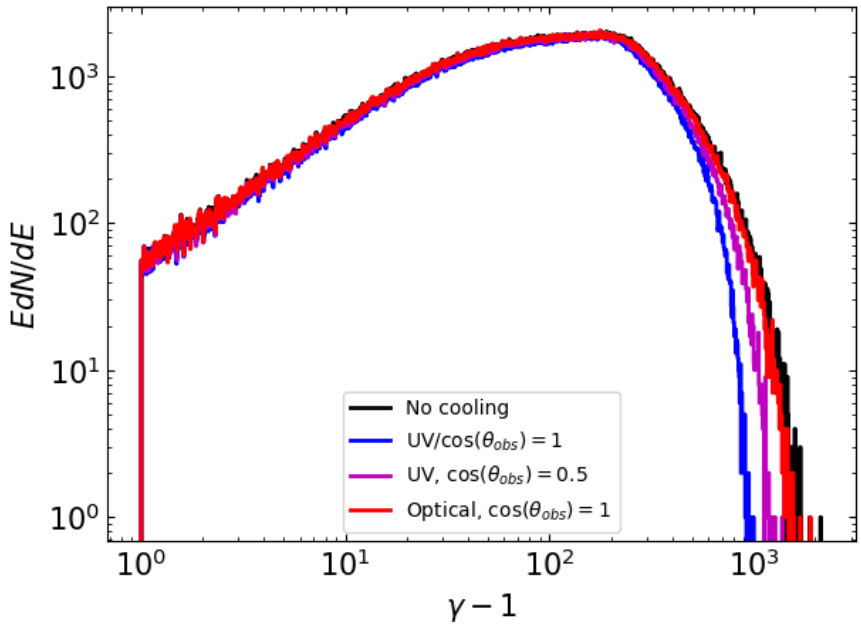

(b)

Figure 6.1: Comparison of the electron Spectra with and without inverse Compton cooling by blackbody photons: Figure (a) displays the impact of IC cooling due to angle-averaged UV photons, while Figure (b) exhibits the effect of IC cooling induced by angle-dependent UV and optical photons at various values of $\cos(\theta_{\rm obs})$. Adopted from Chand and Böttcher (2024).

Thus, the electron distribution then peaks at:

$$\gamma_{max} \simeq \frac{1}{2}\frac{\gamma_i m_i}{m_e}$$

Here, $\gamma_{\rm i}$ is the Lorentz factor of the ions (protons). The spectra illustrated in Figure 6.1 are measured in the simulation frame, where a pure e^--ion plasma shows no evidence of a power law. Initially, the electron spectra exhibit a Maxwellian distribution that evolves into a non-Maxwellian distribution, with a remnant of the original distribution. Ultimately, the system reaches a steady state with a peak around $\gamma \cong \Gamma {\rm m_i/m_e}$.

In the spine frame, the radiation cooling term for inverse Compton scattering of relativistic electrons in the angle-integrated blackbody photon field in the Thomson regime can be expressed as

$$\frac{d\gamma}{dt} = \Gamma_{rel}^2 \frac{\pi^4}{15} \sigma_T c K \gamma^2 \theta^4, \tag{6.1}$$

where $\Gamma_{\rm rel} = 2\Gamma^2 + 1$ is the relative bulk Lorentz factor between the spine and the sheath. This factor enhances radiative efficiency by leveraging the relative Doppler boosting of the radiation fields within the two jet components (Liang et al., 2017; Liang et al., 2018). Similarly, to calculate the cooling rate for inverse Compton scattering of relativistic electrons in the angle-dependent blackbody photon field in the spine frame, a factor $\Gamma_{\rm rel}^2$ needs to be added to the r.h.s. of Equation 3.71 as

$$\begin{aligned}\frac{d\gamma}{dt}(\mu,\gamma,\theta) = A\Gamma_{rel}^2 \Bigg[&\left(\epsilon_{s_{\rm max}}^2 - \epsilon_{s_{\rm min}}^2\right) + \frac{\epsilon_{s_{\rm max}}^4 - \epsilon_{s_{\rm min}}^4}{4\gamma^2} + \frac{\epsilon_{s_{\rm max}}^5 - \epsilon_{s_{\rm min}}^5}{5\gamma^3} - \frac{2}{B}\Bigg\{ \frac{(\epsilon_{s_{\rm max}}^3 - \epsilon_{s_{\rm min}}^3)}{3\gamma^2} \\ &+ \frac{\epsilon_{s_{\rm max}}^4 - \epsilon_{s_{\rm min}}^4}{4\gamma^3} \Bigg\} + \frac{1}{\gamma^4 B^2}\Bigg\{ \frac{\epsilon_{s_{\rm max}}^4 - \epsilon_{s_{\rm min}}^4}{4} + \frac{2\left(\epsilon_{s_{\rm max}}^5 - \epsilon_{s_{\rm min}}^5\right)}{5\gamma} + \frac{\epsilon_{s_{\rm max}}^6 - \epsilon_{s_{\rm min}}^6}{2\gamma^2} \\ &+ \frac{4\left(\epsilon_{s_{\rm max}}^7 - \epsilon_{s_{\rm min}}^7\right)}{7\gamma^3} \Bigg\} \Bigg].\end{aligned} \tag{6.2}$$

The angular distribution of inverse Compton scattering is described by Equation 3.66. These angles indicate the directions of the electron and photon relative to the jet axis. By assuming azimuthal symmetry of the system and performing the numerical integration of Equation (3.71) over $\mu_{\rm ph}$, the electron cooling rate can be obtained as a function of $\mu_{\rm obs}$. Figure 6.2 illustrates the dependency of the cooling rate on the cosine of $\theta_{\rm obs}$. To investigate the influence of IC cooling on the dynamics of electrons, the cooling term in Equations 6.1 and 6.2 need to be incorporated into the particle routine within the simulation code. Figure 6.1 illustrates the impact of Inverse Compton cooling on electron spectra induced by angle-averaged and angle-dependent photons. The strength of IC cooling depends on the radiation energy density and the Lorentz factor of the electrons. At lower electron energies, the cooling effect is negligible, while at higher energies, it significantly affects electron acceleration and the energy spectrum. Due to radiation drag, the high-energy end of the spectrum shifts towards lower energies (as seen in Fig. 6.1). Compared to IC cooling induced by UV photons, the effect of Compton drag for photons with temperatures $\theta \leq 10^{-6}$ is subdominant, and thus does not appreciably affect particle dynamics and the electron energy spectrum.

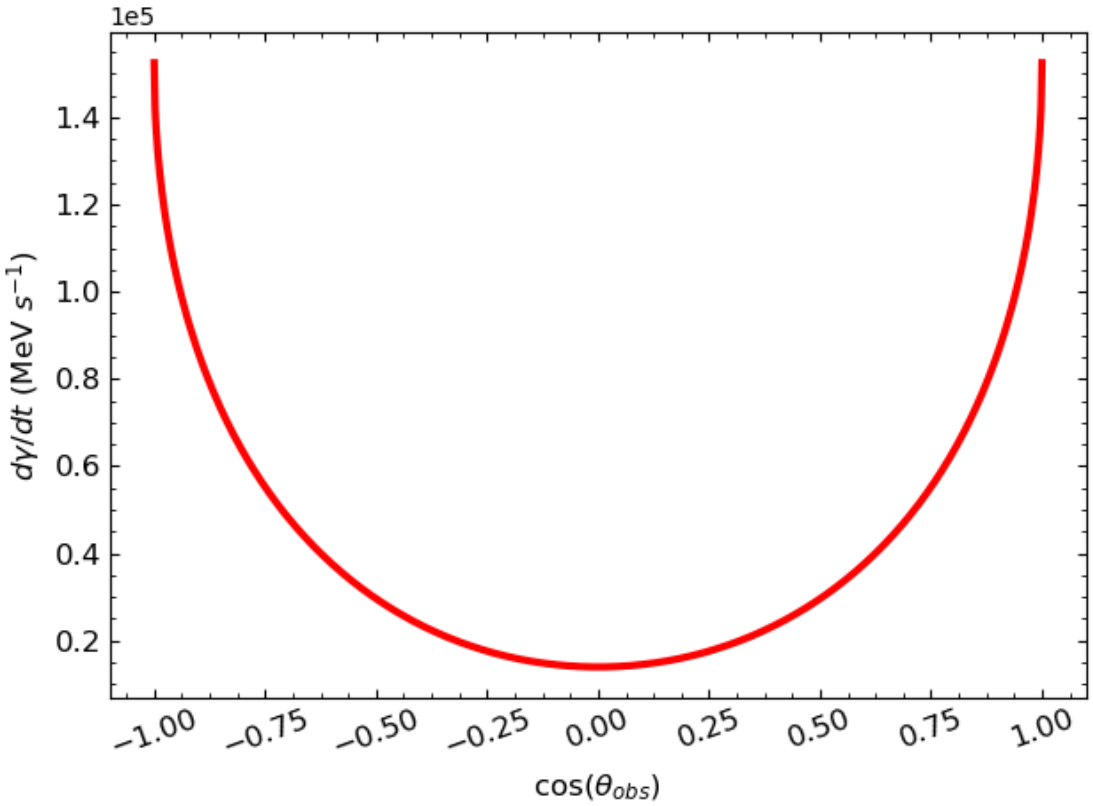

Figure 6.2: Variation of the cooling rate with the cosine of observer's angle ($\cos(\theta_{\rm obs})$) in the ELF at a Lorentz factor (γ) of 10^3 and radiation temperature (θ) of 10^{-5}: the plot depicts the inverse cooling term, obtained by integrating equation (3.71) over the photon distribution angle ($\mu_{\rm ph}$). The figure illustrates that the maximum cooling occurs when electrons travel parallel to the jet axis. Conversely, the minimum cooling is observed when electrons travel perpendicular to the jet axis. Adopted from Chand and Böttcher (2024).

6.2 Self-consistent Radiation Spectra

Blazars exhibit characteristic spectral energy distribution (SED) characterized by two distinct, non-thermal components. The lower-energy component, attributed to synchrotron emission from relativistic leptons, is prominently observed across the radio to optical/UV bands, and in certain cases, extends up to X-rays. In leptonic models, the higher-energy counterpart is ascribed to inverse Compton scattering by the same leptons, either with synchrotron photons (SSC) or external photons (EC). In this section, we discuss the radiation spectra resulting from Compton upscattering of different radiation backgrounds. Specifically, we consider the Cosmic Microwave Background (CMB), infrared, optical, and ultraviolet photons with corresponding values of θ equal to 4.58×10^{-10}, 10^{-8}, 10^{-6}, and 10^{-5}, respectively.

We observe sharp spectral peaks in the emissivity of Compton-scattered blackbody pho-

tons by mono-energetic relativistic electrons as evident in Figure 3.8. Leveraging the pronounced spectral peaks, we apply a monochromatic approximation to convert the particle energy loss rate to a monochromatic radiation spectrum. This simplification significantly streamlines our calculations and reduces computational time, enabling more efficient analysis of the radiation spectrum. The obtained results, encompassing both angle-averaged and angle-dependent photon distributions, are presented in Figures 6.3 and 6.4. Throughout the various stages of the simulations, we observe distinct evolutions in the Compton spectra of relativistic electrons interacting with photon fields. In the early phases of the simulations, both angle-integrated and angle-dependent cases exhibit a quasi-thermal inverse Compton spectrum with a single dominant component. We observe a quasi-thermal inverse Compton spectrum with a single component around simulation time of $t = 1500/\omega_{p,e}$ for an angle-integrated photon field and $t = 2000/\omega_{p,e}$ for an angle-dependent photon distribution, as depicted in Figures 6.3(a) and 6.4(a). As the simulation progresses, the Compton spectra undergo noteworthy changes. The single-component spectrum develops into a double-component spectrum, around $t = 2500/\omega_{p,e}$ and $t = 4000/\omega_{p,e}$ for the angle-integrated and angle-dependent photon distributions, respectively (see Figures 6.3(b) and 6.4(b)). In the later steady state of the simulations, observed beyond $t = 3000/\omega_{p,e}$ and $t = 5000/\omega_{p,e}$, respectively, a distinct spectral pattern emerges. The Compton spectrum exhibits a quasi-thermal low-frequency spectrum with a cut-off power-law tail (see Figures 6.3(c) and 6.4(c)).

The steady state is achieved later in the case of the inverse Compton spectra from scattering an angle-dependent photon field compared to the angle-averaged photon field. The angle-dependent Compton spectra exhibit a flatter peak in comparison to the angle-averaged Compton spectra. The observed peak energy in the angle-dependent radiation spectra is approximately $2.7\theta\gamma^2$ for $\cos(\theta_{obs}) = 1$, where $\gamma \approx 10^2$. As the value of $\cos(\theta_{obs})$ decreases, the peak energy of the radiation spectra progressively shifts towards lower energies. This observed correlation between the peak energy and $\cos(\theta_{obs})$ highlights the pronounced angular dependence intrinsic to the radiative output in relativistic jets. The radiation spectra obtained in the case of an angle-dependent photon distribution are similar to those obtained for angle-averaged photons.

In our simulations, we observe the angle-averaged radiation spectra attaining a steady state beyond $t = 3000/\omega_{p,e}$, while angle-dependent radiation spectra beyond $t = 5000/\omega_{p,e}$. Beyond this stage, there are no significant fluctuations in their shapes, reaffirming the reliability and accuracy of our results and reflecting the dynamic equilibrium achieved in our simulated system. The time delay in reaching a steady state for the angle-dependent photon field's inverse Compton spectra, in comparison to the angle-averaged photon field, can be attributed to the increased complexity and larger parameter space resulting from the inclusion of angle-dependent photons. This introduces a higher computational demand for thorough sampling and evaluation of radiation outputs, leading to extended times needed to establish a stable equilibrium and achieve consistent radiation outputs.

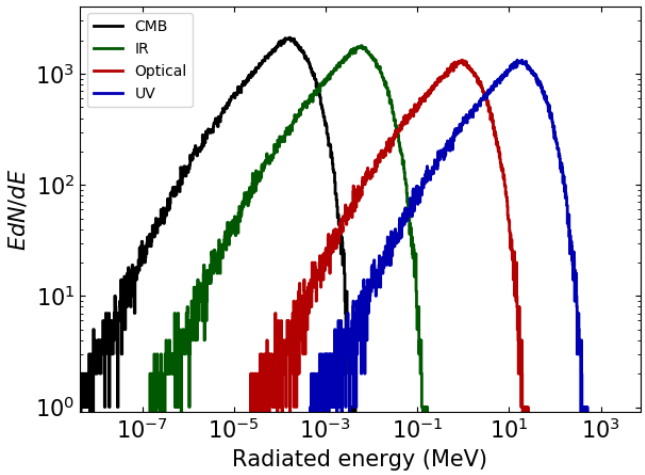

(a)

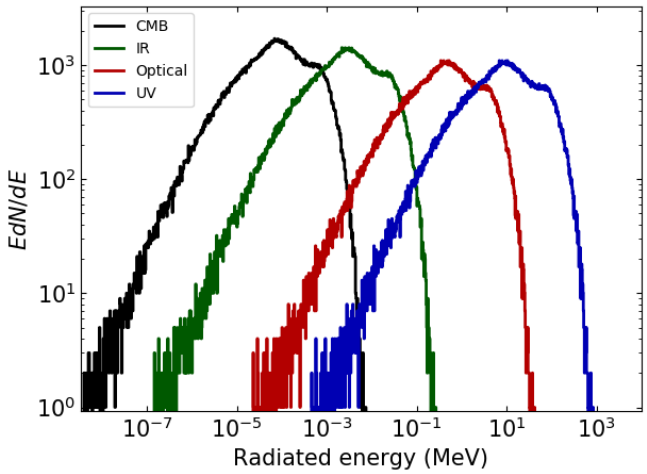

(b)

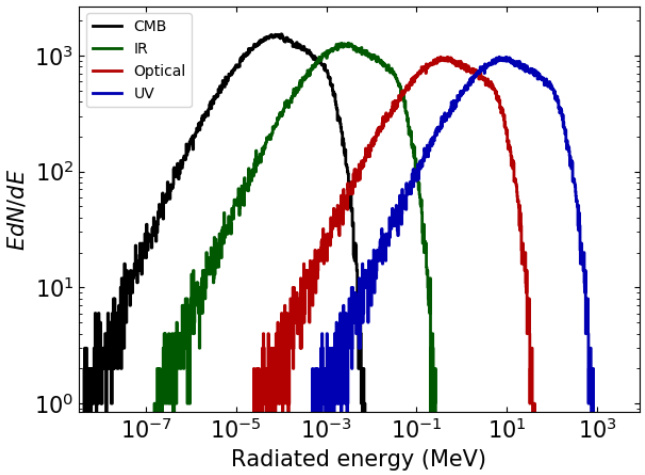

(c)

Figure 6.3: Time-integrated angle-averaged Compton spectra in the sheath frame obtained from simulations conducted for different radiation temperatures of angle-averaged blackbody photon fields: the spectra correspond to three distinct phases: (a) early phase of the simulations at t = 1500 $\omega_{\rm p,e}^{-1}$, (b) intermediate phase at t = 2500 $\omega_{\rm p,e}^{-1}$, and (c) later steady state at t = 3000 $\omega_{\rm p,e}^{-1}$. Adopted from Chand and Böttcher (2024).

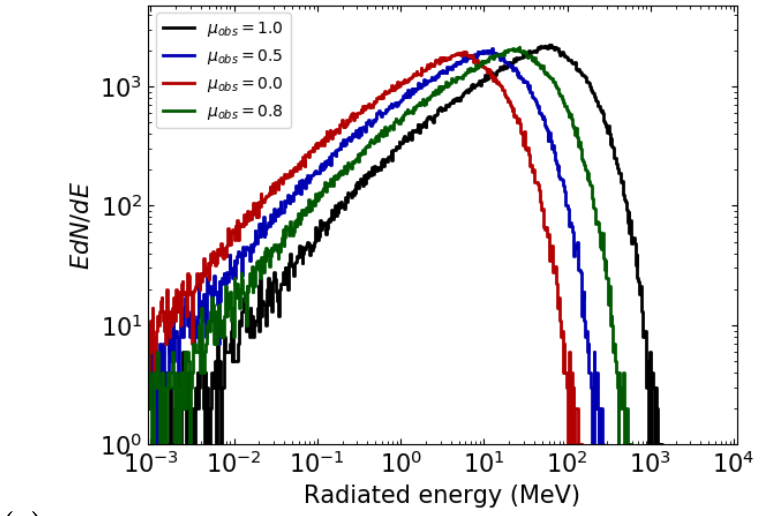

(a)

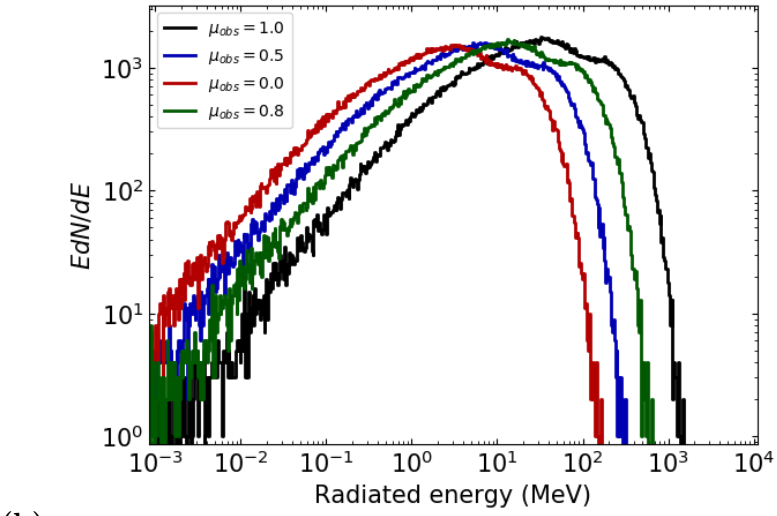

(b)

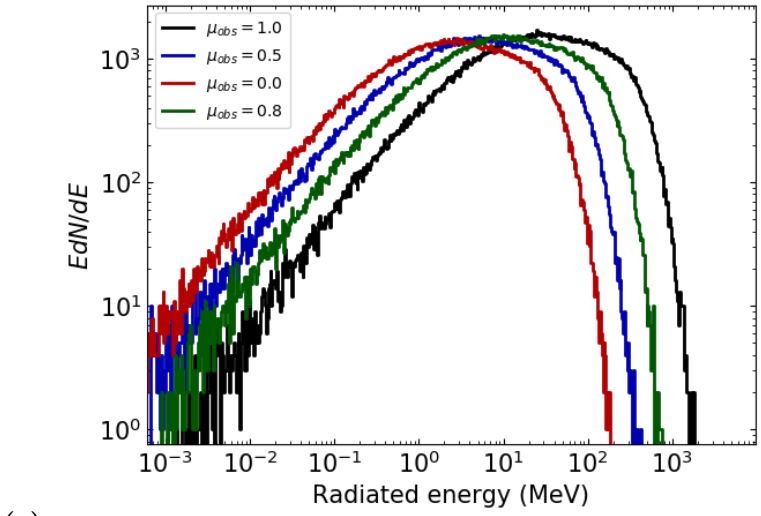

(c)

Figure 6.4: Time-integrated angle-dependent Compton spectra in the sheath frame, resulting from simulations conducted at radiation temperature $\theta = 10^{-5}$ and different viewing angles: spectra are obtained at simulation time of (a) t = 2000 $\omega_{p,e}^{-1}$, (b) t = 4000 $\omega_{p,e}^{-1}$, and (c) t = 5000 $\omega_{p,e}^{-1}$. Adopted from Chand and Böttcher (2024).

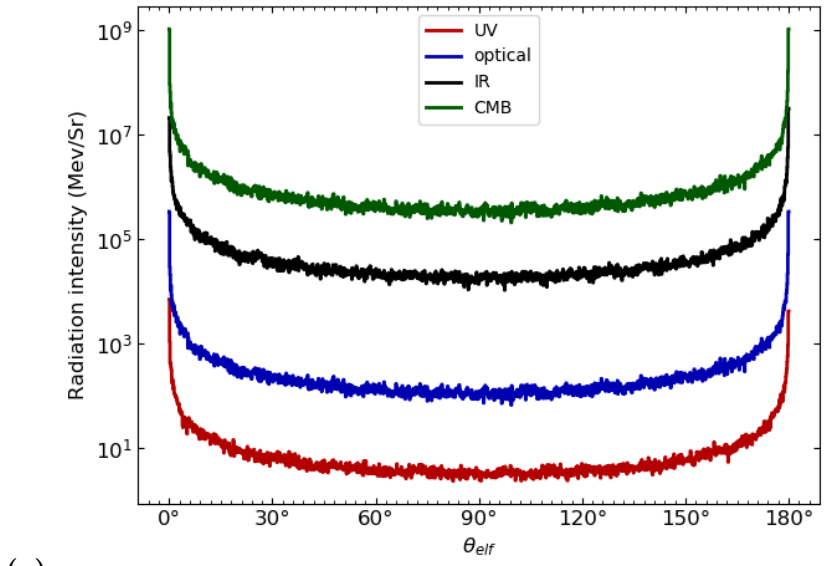

(a)

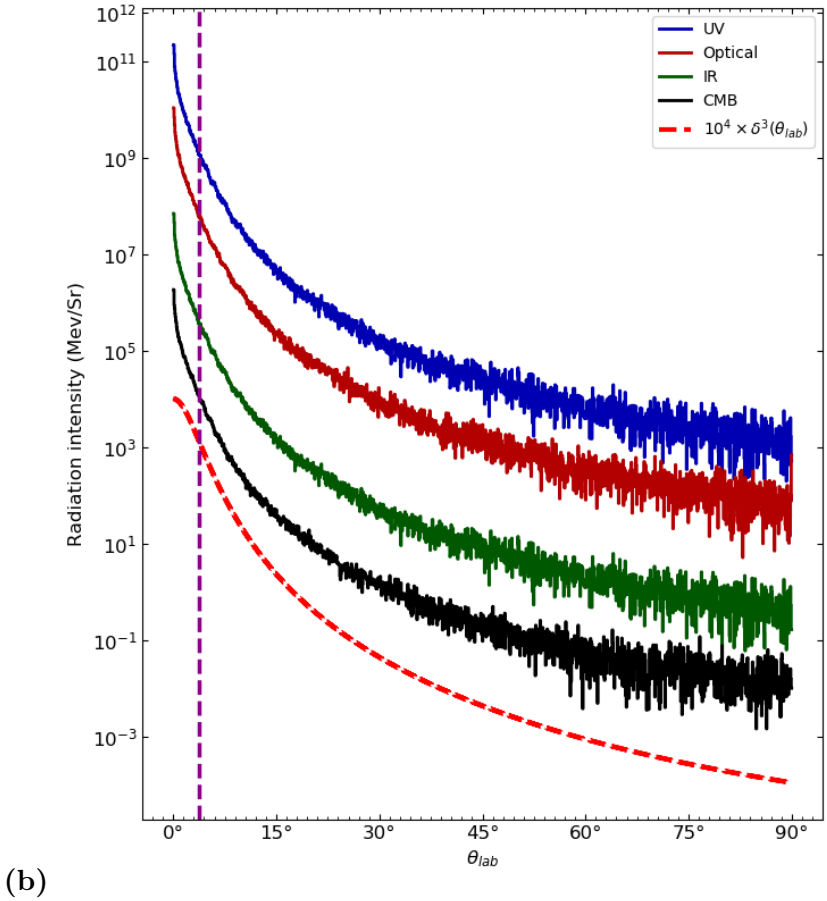

(b)

Figure 6.5: Radiation intensity resulting from Compton scattering of an angle-averaged photon field with varying temperatures as a function of the viewing angle of the jet at a simulation time of t = $3000\omega_{p,e}^{-1}$: panel (a) displays the global radiative energy distribution per unit solid angle in the ELF, while panel (b) shows the same distribution in the laboratory frame (sheath). The dashed curve represents the δ^3 boosting pattern, characteristic of co-moving isotropic photon emission. The violet dashed line represents $1/\Gamma$. Adopted from Chand and Böttcher (2024).

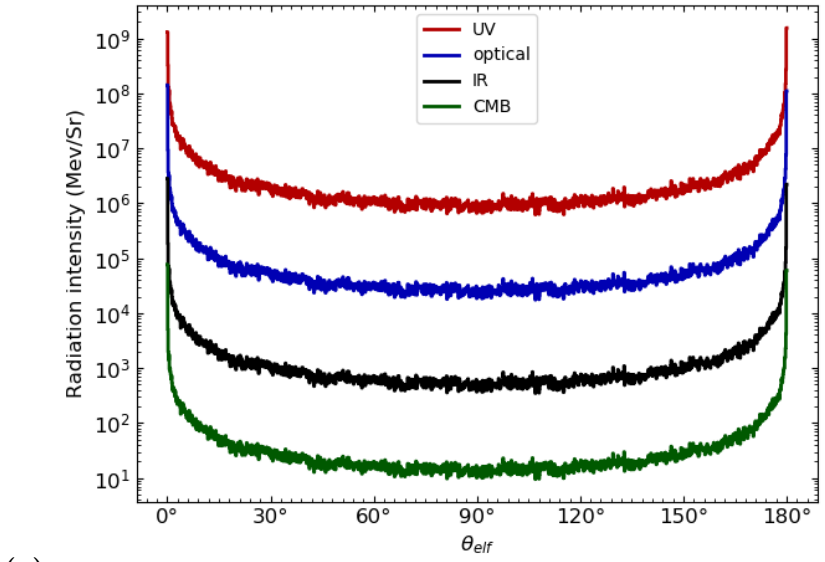

(a)

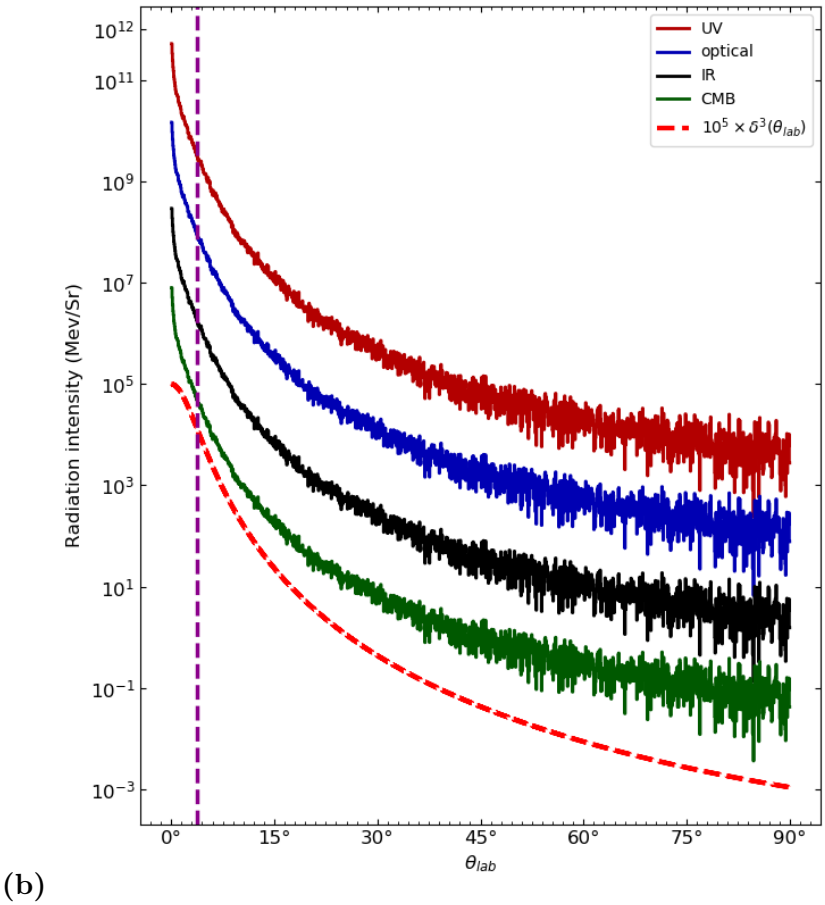

(b)

Figure 6.6: Radiation intensity of an angle-dependent photon field, subject to Compton upscattering by relativistic electrons as a function of the viewing angle of the jet at a simulation time of t = $5000\omega_{\mathrm{p,e}}^{-1}$ for varying radiation temperatures: panel (a) exhibits the global radiative energy distribution per unit solid angle in the ELF. Panel (b) shows the corresponding distribution in the laboratory frame. The dashed curve represents the δ^3 boosting pattern. Adopted from Chand and Böttcher (2024).

The broader and flatter spectral peak observed in the angle-dependent Compton spectra signifies a greater number of scattering events, indicating a more intricate interplay between photons and particles in this scenario. This difference in spectral characteristics further contributes to the increased time required to attain a steady state in the angle-dependent case.

6.2.1 Observable Features of Radiation Spectra

To establish a connection between the radiative output obtained from the simulations and the observational data, we can plot the radiation intensity ($\mathrm{dE/d\Omega}$) as a function of the viewing angle. Here, dE represents the radiation energy and $\mathrm{d\Omega}$ denotes the differential solid angle, defined as $\mathrm{d\Omega} = \sin\theta_{\mathrm{ph}}\mathrm{d}\theta_{\mathrm{ph}}\mathrm{d}\phi_{\mathrm{ph}}$. The angle θ_{ph} represents the angle between the final direction of radiation and the axis of the jet (i.e., the viewing angle), while ϕ_{ph} represents the azimuthal angle. The system is azimuthally symmetric in ϕ, so we may set $\mathrm{d}\phi_{\mathrm{ph}} = 2\pi$. In the ELF, as depicted in Figures 6.5(a) and 6.6(a), the spine electrons emit the highest radiation intensities along the jet axis (i.e. at $\theta_{\mathrm{ph}} = \theta_{\mathrm{elf}} = 0°$).

In order to determine the radiation intensity as observed by an observer, we apply a Lorentz transformation into the sheath frame. Figures 6.5 and 6.6 show plots of the radiation intensity versus viewing angle and demonstrate that the inverse Compton radiation emitted from the jet's SBL experiences a strong boost in the forward direction, with a characteristic angle much smaller than $1/\Gamma$. This is indicated by the violet dashed lines in Figures 6.5(b) and 6.6(b).

In the case of isotropic photon emission in the co-moving frame of an emission region moving with Lorentz factor Γ along the jet viewed at an angle θ_{lab}, the radiative energy flux $\mathrm{dF/dE}$ is boosted by a factor δ^3, with $\delta = 1/\Gamma(1 - \beta_\Gamma \cos\theta_{\mathrm{lab}})$ being the Doppler factor. The dashed curve depicted in Figures 6.5(b) and 6.6(b) illustrate the comparison of the simulated beaming characteristic to this δ^3 pattern. The simulated beaming characteristics show that the radiation is strongly boosted in a forward direction and this boosting is more powerful than what would be expected from Doppler boosting of an isotropic radiation field in the co-moving frame of the spine.

6.3 Discussion and Outlook

We employed the monochromatic approximation to compute radiation spectra, motivated by the distinct spectral peaks in emissivity arising from Compton scattering of blackbody photons by monoenergetic relativistic electrons, as illustrated in Figure 3.8. The difference between the monochromatic approximation and a full integration over emission profiles is expected to be minimal, as the spectral shape is primarily governed by the broader thermal+non-thermal electron spectra rather than the emissivity profiles of monoenergetic electrons. Recent work by Del Gaudio et al. (2020) introduces a promising numerical

approach for investigating radiative processes, such as inverse Compton emission. Their benchmarked algorithm seamlessly integrates with the standard PiC loop, enhancing computational efficiency–a potential avenue for future exploration in our research. The radiative output in our study is directly obtained from the PiC simulation, providing a basis for calculating radiation intensity and studying angle-dependent inverse-Compton spectra while self-consistently considering the inverse-Compton cooling of relativistic electrons.

Chapter 7

Conclusions and Future Prospects

This thesis encompasses the presentation of findings derived from an investigation into the self-generated electric and magnetic fields, as well as particle acceleration phenomena occurring within SBLs of relativistic jets associated with AGNs and GRBs, and the subsequent inverse-Compton radiation output. Our PiC simulations reveal that in radially stratified, relativistic jets, relativistic shear layers can effectively generate well-organized magnetic fields. This process results in highly anisotropic particle acceleration. High energy particles are accelerated along the magnetic field lines, resulting in an anisotropic momentum distribution. This anisotropic particle distribution contributes effectively to the radiative output, along with the exchange of particles between the spine and sheath regions. Due to the significant anisotropy in the particle distribution, Compton emission becomes highly directional, further contributing to the Doppler boosting attributed to the relativistic bulk motion of the jet. The pronounced dependence of the angular distribution of relativistic leptons on energy in spine-sheath jets holds significant implications for the high-energy emissions from relativistic jet sources like blazars and GRB. Existing efforts in modeling the spectral energy distributions of blazars, using scenarios involving leptonic radiation, typically presume an isotropic relativistic electron distribution in the co-moving frame of the jet's bulk motion (e.g., Ghisellini et al., 2010; Böttcher et al., 2013). In these models, there is a frequent reliance on relatively high minimum Lorentz factors for the relativistic electron distribution. My findings suggest that the radiative interaction between the spine and sheath serves to enhance radiative efficiency. This enhancement is attributed to the relative Doppler boosting of radiation fields generated in these two distinct components of the jet.

The monochromatic approximation was employed to compute the radiation spectra, motivated by the sharp spectral peaks in the emissivity resulting from the Compton scattering of blackbody photons by monoenergetic relativistic electrons, as illustrated in Figure 3.8. The difference between the monochromatic approximation and a full integration over the emission profiles is expected to be very small, as the spectral shape is dominated by the shape of the broad, thermal+non-thermal electron spectra and not the emissivity profiles of mono-energetic electrons. The recent work by Del Gaudio et al. (2020) has

introduced a promising numerical prospect to investigate radiative processes like inverse Compton emission. Their benchmarked algorithm seamlessly integrates with the standard PiC loop, improving computational efficiency. In future investigations, experimentation with this scheme is planned as part of the ongoing research efforts. The radiative output in this study has been directly obtained from the PiC simulation, from which the radiation intensity is calculated to investigate angle-dependent inverse-Compton spectra, while self-consistently accounting for inverse-Compton cooling of relativistic electrons. To our knowledge, investigations into the angular dependence of radiative emissions from shear boundary layers (SBLs) within relativistic jets have not been conducted previously. Our research marks the pioneering effort to explore particle acceleration, the ensuing inverse Compton spectra, and the impact of inverse Compton cooling on the dynamics of relativistic electrons, while considering the impact of angular variations within these shear layers. Both angle-averaged and angle-dependent distributions of target photons were examined, utilizing a δ-function approximation for the target photon field. The findings showed that IC cooling can have a non-negligible impact on the acceleration of relativistic particles at SBLs, causing high-energy electrons to cool down to slightly lower energies. As expected, the inverse-Compton cooling effect becomes more pronounced for higher target-photon blackbody temperatures. In the early stages of simulations, both angle-integrated and angle-dependent inverse Compton radiation spectra exhibit a single component, quasi-thermal radiation spectrum. As the simulations progress, the spectrum evolves into a two-component spectrum, which eventually becomes a quasi-thermal low-frequency spectrum with a cut-off power-law tail.

The radiation emitted is strongly boosted along the jet axis, with a characteristic opening angle much less than $1/\Gamma$. This boosting is more powerful than what would be expected from Doppler boosting of an isotropic radiation field in the co-moving frame of the spine. The Doppler factor estimates for TeV blazars using one-zone models are inconsistent with VLBI observations. Our findings suggest that the extreme beaming patterns of particles accelerated at SBLs could resolve the long-standing problem of the Doppler factor crisis (e.g., Lyutikov and Lister, 2010).

In future work, the effects of a non-zero initial magnetic field on the plasma in relativistic jets will be explored, which could involve investigating a relativistic magnetically dominated electron-positron jet interacting with a weakly magnetized electron-ion ambient plasma. Recent work by Sironi et al. (2021) has shown that such systems can develop Kelvin-Helmholtz instabilities and kinetic-scale reconnection layers, which provide a first-principles mechanism for particle injection into shear-driven acceleration. This could offer valuable insights into the complex dynamics of these shear-structured jets. Our research focused on initially unmagnetized plasma within SBLs of relativistic jets. The extension of the study to encompass weakly magnetized plasma is anticipated in the future. An initially magnetized plasma can provide a seed magnetic field, possibly amplified through processes like relativistic turbulence, leading to stronger fields within the jet. This, in comparison to an initially unmagnetized plasma, may enhance jet stability, facilitate particle acceleration, and result in non-thermal emissions. Moreover, the initial magnetic field's presence may

increase the efficiency of synchrotron radiation production and lead to more pronounced relativistic beaming, impacting radiation characteristics. In magnetically dominated plasmas, a common phenomenon is the presence of pitch-angle anisotropy. To gain a comprehensive understanding of radiative emissions from accelerated particles in relativistic jets, it is crucial to explore both their energy spectrum and pitch-angle anisotropy. The study conducted by Comisso and Jiang (2023) has provided a first-principles description of how reconnection-driven acceleration leads particles to non-thermal energies, covering both the energy spectrum of particles and their energy-dependent pitch-angle anisotropy. In future research endeavors, it is intended to enhance this understanding by implementing pitch-angle anisotropy into the radiative model, employing PiC simulations. This extension seeks to improve the predictive capability for the radiation signatures produced by these particles, thus advancing insights into the intricate physics governing magnetically dominated plasmas and their radiative behavior. Comprehensive insights into these scenarios require extensive kinetic simulations to unveil the complete picture.

Bibliography

Abbott, B. P. & others, L. S. C., Collaboration, V., ray Burst Monitor, F. G., and INTEGRAL (2017). Gravitational Waves and Gamma-Rays from a Binary Neutron Star Merger: GW170817 and GRB 170817A. *The Astrophysical Journal Letters*, 848(2):L13.

Alston, W., Giustini, M., and Petrucci, P. O. (2022). The super-massive black hole close environment in active galactic nuclei.

Alves, E. P., Grismayer, T., Fonseca, R. A., and Silva, L. O. (2014). Electron-scale shear instabilities: magnetic field generation and particle acceleration in astrophysical jets. *New Journal of Physics*, 16(3):035007.

Alves, E. P., Grismayer, T., Martins, S. F., Fiúza, F., Fonseca, R. A., and Silva, L. O. (2012). Large-Scale Magnetic Field Generation via the Kinetic Kelvin-Helmholtz Instability in Unmagnetized Scenarios. 746(2):L14.

Angel, J. R. P. and Stockman, H. S. (1980). Optical and infrared polarization of active extragalactic objects. *Annual Review of Astronomy and Astrophysics*, 18:321–361.

Axford, W. I., Leer, E., and Skadron, G. (1977). The Acceleration of Cosmic Rays by Shock Waves. In *International Cosmic Ray Conference*, volume 11 of *International Cosmic Ray Conference*, page 132.

Baade, W. and Minkowski, R. (1954). On the Identification of Radio Sources. *The Astrophysical Journal*, 119:215.

Baring, M. G., Böttcher, M., and Summerlin, E. J. (2016). Probing acceleration and turbulence at relativistic shocks in blazar jets. *Monthly Notices of the Royal Astronomical Society*, 464(4):4875–4894.

Beckmann, V. and Shrader, C. R. (2012). *Active Galactic Nuclei*.

Bell, A. R. (1978). The acceleration of cosmic rays in shock fronts - I. *Monthly Notices of the Royal Astronomical Society*, 182:147–156.

Birdsall, C. (1991). Particle-in-cell charged-particle simulations, plus monte carlo collisions with neutral atoms, pic-mcc. *IEEE Transactions on Plasma Science*, 19(2):65–85.

Blandford, R., Meier, D., and Readhead, A. (2019). Relativistic Jets from Active Galactic Nuclei. *Annual Review of Astronomy and Astrophysics*, 57:467–509.

Blandford, R., Rees, M., and Wolfe, A. (1978). Pittsburgh conference on BL Lac objects. *AM Wolfe, Ed*, 328.

Blandford, R. D. and Ostriker, J. P. (1978). Particle acceleration by astrophysical shocks. *The Astrophysical Journal Letters*, 221:L29–L32.

Blandford, R. D. and Payne, D. G. (1982). Hydromagnetic flows from accretion disks and the production of radio jets. *Monthly Notices of the Royal Astronomical Society*, 199:883–903.

Blandford, R. D. and Rees, M. J. (1974). A "twin-exhaust" model for double radio sources. *Monthly Notices of the Royal Astronomical Society*, 169:395–415.

Blandford, R. D. and Znajek, R. L. (1977). Electromagnetic extraction of energy from Kerr black holes. *Monthly Notices of the Royal Astronomical Society*, 179:433–456.

Boccardi, B., Krichbaum, T., Bach, U., Mertens, F., Ros, E., Alef, W., and Zensus, J. A. (2016). The stratified two-sided jet of cygnus a-acceleration and collimation. *Astronomy & Astrophysics*, 585:A33.

Boris, J. P. (1970). Relativistic plasma simulation-optimization of a hybrid code. *Proceeding of Fourth Conference on Numerical Simulations of Plasmas*.

Böttcher, M. (2007). Modeling the emission processes in blazars. In *The Multi-Messenger Approach to High-Energy Gamma-Ray Sources*, pages 95–104. Springer.

Böttcher, M., Harris, D. E., and Krawczynski, H. (2012). *Relativistic Jets from Active Galactic Nuclei*.

Böttcher, M., Reimer, A., Sweeney, K., and Prakash, A. (2013). Leptonic and Hadronic Modeling of Fermi-detected Blazars. *The Astrophysical Journal*, 768(1):54.

Boyd, T. J. M. and Sanderson, J. J. (2003). *The Physics of Plasmas*. Cambridge University Press.

Bruni, G., Gómez, J. L., Vega-García, L., Lobanov, A. P., Fuentes, A., Savolainen, T., Kovalev, Y. Y., Perucho, M., Martí, J. M., Anderson, J. M., Edwards, P. G., Gurvits, L. I., Lisakov, M. M., Pushkarev, A. B., Sokolovsky, K. V., and Zensus, J. A. (2021). RadioAstron reveals a spine-sheath jet structure in 3C 273. *Astronomy & Astrophysics*, 654:A27.

Carilli, C., Perley, R., Bartel, N., and Dreher, J. (1996). The jets in Cygnus A: from pc- to kpc-scales. In Carilli, C. L. and Harris, D. E., editors, *Cygnus A – Studay of a Radio Galaxy*, page 76.

Celotti, A. and Fabian, A. C. (1993). The kinetic power and luminosity of parsec-scale radio jets - an argument for heavy jets. *Monthly Notices of the Royal Astronomical Society*, 264:228–236.

Cerutti, B. and Giacinti, G. (2023). Extreme ion acceleration at extragalactic jet termination shocks. *arXiv e-prints*, page arXiv:2303.12636.

Cerutti, B., Uzdensky, D. A., and Begelman, M. C. (2012). Extreme Particle Acceleration via Magnetic Reconnection in the Crab Nebula. In *American Astronomical Society Meeting Abstracts #219*, volume 219 of *American Astronomical Society Meeting Abstracts*, page 217.03.

Cerutti, B., Werner, G. R., Uzdensky, D. A., and Begelman, M. C. (2014). Three-dimensional Relativistic Pair Plasma Reconnection with Radiative Feedback in the Crab Nebula. *The Astrophysical Journal*, 782(2):104.

Chand, T. and Böttcher, M. (2022). Effect of inverse compton cooling on relativistic particles accelerated at shear boundary layers in relativistic jets. *Proceedings of the International Astronomical Union*, 17(S375):4953.

Chand, T. and Böttcher, M. (2023). Particle acceleration and inverse Compton emission from shear boundary layers in relativistic jets. *PoS*, HEASA2022:034.

Chand, T. and Böttcher, M. (2024). Inverse compton emission and cooling of relativistic particles accelerated at shear boundary layers in relativistic jets. *The Astrophysical Journal*, 962(1):31.

Chand, T. B., Böttcher, M., and Kilian, P. (2019). Particle-in-cell simulations of shear boundary layers in relativistic jets. *PoS*, HEASA2018:046.

Chandrasekhar, S. (1961). *Hydrodynamic and hydromagnetic stability*.

Comisso, L. and Jiang, B. (2023). Pitch-angle Anisotropy Imprinted by Relativistic Magnetic Reconnection. *The Astrophysical Journal*, 959(2):137.

Curtis, H. D. (1918). Descriptions of 762 Nebulae and Clusters Photographed with the Crossley Reflector. *Publications of Lick Observatory*, 13:9–42.

Dawson, J. M. (1983). Particle simulation of plasmas. *Rev. Mod. Phys.*, 55:403–447.

Del Gaudio, F., Grismayer, T., Fonseca, R. A., and Silva, L. O. (2020). Compton scattering in particle-in-cell codes. *Journal of Plasma Physics*, 86(5):905860516.

Dermer, C. D. and Giebels, B. (2016). Active galactic nuclei at gamma-ray energies. *Comptes Rendus Physique*, 17(6):594–616. Gamma-ray astronomy / Astronomie des rayons gamma - Volume 2.

Dermer, C. D. and Menon, G. (2009). *High Energy Radiation from Black Holes: Gamma Rays, Cosmic Rays, and Neutrinos*. Princeton University Press.

Drake, J. F., Swisdak, M., Che, H., and Shay, M. A. (2006). Electron acceleration from contracting magnetic islands during reconnection. *Nature*, 443(7111):553–556.

Esirkepov, T. (2001). Exact charge conservation scheme for particle-in-cell simulation with an arbitrary form-factor. *Computer Physics Communications*, 135(2):144–153.

Fabian, A. C. (1999). Active galactic nuclei. *Proceedings of the National Academy of Sciences of the United States of America*, 96(9):4749–4751.

Fath, E. A. (1909). The Spectra of Some Spiral Nebulæ and Globular Star Clusters. *Publications of the Astronomical Society of the Pacific*, 21(126):138–143.

Fermi, E. (1949). On the Origin of the Cosmic Radiation. *Physical Review*, 75(8):1169–1174.

Gallant, Y. A. (2002). Particle Acceleration at Relativistic Shocks. In Guthmann, A. W., Georganopoulos, M., Marcowith, A., and Manolakou, K., editors, *Relativistic Flows in Astrophysics*, volume 589, page 24.

Gehrels, N., Norris, J. P., Barthelmy, S. D., Granot, J., Kaneko, Y., Kouveliotou, C., Markwardt, C. B., Mészáros, P., Nakar, E., Nousek, J. A., O'Brien, P. T., Page, M., Palmer, D. M., Parsons, A. M., Roming, P. W. A., Sakamoto, T., Sarazin, C. L., Schady, P., Stamatikos, M., and Woosley, S. E. (2006). A new γ-ray burst classification scheme from GRB060614. *Nature*, 444(7122):1044–1046.

Ghisellini, G., Tavecchio, F., and Chiaberge, M. (2005). Structured jets in TeV BL Lac objects and radiogalaxies. Implications for the observed properties. *Astronomy & Astrophysics*, 432(2):401–410.

Ghisellini, G., Tavecchio, F., Foschini, L., Ghirlanda, G., Maraschi, L., and Celotti, A. (2010). General physical properties of bright Fermi blazars. *Monthly Notices of the Royal Astronomical Society*, 402(1):497–518.

Giroletti, M., Giovannini, G., Feretti, L., Cotton, W. D., Edwards, P. G., Lara, L., Marscher, A. P., Mattox, J. R., Piner, B. G., and Venturi, T. (2004). Parsec-Scale Properties of Markarian 501. *Astrophysical Journal*, 600(1):127–140.

Godfrey, B. B. (1974). Numerical cherenkov instabilities in electromagnetic particle codes. *Journal of Computational Physics*, 15(4):504–521.

Greenwood, A. D., Cartwright, K. L., Luginsland, J. W., and Baca, E. A. (2004). On the elimination of numerical Cerenkov radiation in PIC simulations. *Journal of Computational Physics*, 201(2):665–684.

Grismayer, T., Alves, E. P., Fonseca, R. A., and Silva, L. O. (2013a). dc-Magnetic-Field Generation in Unmagnetized Shear Flows. *Physical Review Letters*, 111(1):015005.

Grismayer, T., Alves, E. P., Fonseca, R. A., and Silva, L. O. (2013b). Theory of multidimensional electron-scale instabilities in unmagnetized shear flows. *Plasma Physics and Controlled Fusion*, 55(12):124031.

Gruzinov, A. (2008). Grb: magnetic fields, cosmic rays, and emission from first principles?

Guo, F., Li, H., Daughton, W., Li, X., and Liu, Y.-H. (2016). Particle acceleration during magnetic reconnection in a low-beta pair plasma. *Physics of Plasmas*, 23(5):055708.

Hadi, M. F. and Piket-May, M. (1997). A modified FDTD (2, 4) scheme for modeling electrically large structures with high-phase accuracy. *IEEE Transactions on Antennas and Propagation*, 45(2):254–264.

Hakobyan, H., Philippov, A., and Spitkovsky, A. (2019). Effects of synchrotron cooling and pair production on collisionless relativistic reconnection. *The Astrophysical Journal*, 877(1):53.

Hazard, C., Mackey, M. B., and Shimmins, A. J. (1963). Investigation of the Radio Source 3C 273 By The Method of Lunar Occultations. *Nature*, 197(4872):1037–1039.

Hockney, R. W. and Eastwood, J. W. (1981). *Computer Simulation Using Particles*.

Iwamoto, M., Amano, T., Hoshino, M., Matsumoto, Y., Niemiec, J., Ligorini, A., Kobzar, O., and Pohl, M. (2019). Precursor wave amplification by ionelectron coupling through wakefield in relativistic shocks. *The Astrophysical Journal*, 883(2):L35.

Jansky, K. G. (1933). Radio Waves from Outside the Solar System. *Nature*, 132(3323):66.

Jennison, R. and Das Gupta, M. (1953). Fine structure of the extra-terrestrial radio source cygnus i. *Nature*, 172(4387):996–997.

Jester, S., Röser, H.-J., Meisenheimer, K., Perley, R., and Conway, R. (2001). Hst optical spectral index map of the jet of 3c 273. *Astronomy & Astrophysics*, 373(2):447–458.

Junor, W. and Biretta, J. A. (1999). Structure of the M87 Jet on Light-week Scales. In *American Astronomical Society Meeting Abstracts #194*, volume 194 of *American Astronomical Society Meeting Abstracts*, page 50.17.

Kaaz, N., Murguia-Berthier, A., Chatterjee, K., Liska, M. T. P., and Tchekhovskoy, A. (2023). Jet Formation in 3D GRMHD Simulations of Bondi-Hoyle-Lyttleton Accretion. *The Astrophysical Journal*, 950(1):31.

Kagan, D., Sironi, L., Cerutti, B., and Giannios, D. (2015). Relativistic Magnetic Reconnection in Pair Plasmas and Its Astrophysical Applications. *Space Science Reviews*, 191(1-4):545–573.

Keel, W. C. (1983). Spectroscopic evidence for activity in the nuclei of normal spiral galaxies. *The Astrophysical Journal*, 269:466–486.

Kilian, P., Burkart, T., and Spanier, F. (2012). The Influence of the Mass Ratio on Particle Acceleration by the Filamentation Instability. In *High Performance Computing in Science and Engineering '11*, pages 5–13.

Kilian, P., Ganse, U., and Spanier, F. (2013). Different Choices of the Form Factor in Particle-in-Cell Simulations. In Pogorelov, N. V., Audit, E., and Zank, G. P., editors, *Numerical Modeling of Space Plasma Flows (ASTRONUM2012)*, volume 474 of *Astronomical Society of the Pacific Conference Series*, page 208.

Krymskii, G. F. (1977). A regular mechanism for the acceleration of charged particles on the front of a shock wave. *Akademiia Nauk SSSR Doklady*, 234:1306–1308.

Laing, R. A. (1980). A model for the magnetic-field structure in extended radio sources. *Monthly Notices of the Royal Astronomical Society*, 193:439–449.

Lense, J. and Thirring, H. (1918). Über den Einfluß der Eigenrotation der Zentralkörper auf die Bewegung der Planeten und Monde nach der Einsteinschen Gravitationstheorie. *Physikalische Zeitschrift*, 19:156.

Liang, E., Boettcher, M., and Smith, I. (2013a). Magnetic field generation and particle energization at relativistic shear boundaries in collisionless electron-positron plasmas. *The Astrophysical Journal*, 766(2):L19.

Liang, E., Fu, W., Boettcher, M., Smith, I., and Roustazadeh, P. (2013b). Relativistic positron-electron-ion shear flows and application to gamma-ray bursts. *The Astrophysical Journal*, 779(2):L27.

Liang, E., Fu, W., Böttcher, M., and Roustazadeh, P. (2018). Scaling of Relativistic Shear Flows with the Bulk Lorentz Factor. *The Astrophysical Journal*, 854(2):129.

Liang, E., Fu, W., and Bttcher, M. (2017). Relativistic shear flow between electron–ion and electron–positron plasmas and astrophysical applications. 847(2):90.

Lifshitz, E. M. and Pitaevskii, L. P. (1981). *Physical kinetics*.

Liska, M. T. P. (2019). *Exploring black hole accretion in unexplored regimes using GRMHD simulations*. PhD thesis, University of Amsterdam, Netherlands.

Liu, R.-Y., Rieger, F. M., and Aharonian, F. A. (2017). Particle acceleration in mildly relativistic shearing flows: The interplay of systematic and stochastic effects, and the origin of the extended high-energy emission in AGN jets. 842(1):39.

Longair, M. S. (2011). *High Energy Astrophysics*.

Lyubarsky, Y. (2006). Electron-ion coupling upstream of relativistic collisionless shocks. *Astrophys. J.*, 652:1297–1305.

Lyutikov, M. and Lister, M. (2010). Resolving Doppler-factor Crisis in Active Galactic Nuclei: Non-steady Magnetized Outflows. *Astrophysical Journal*, 722(1):197–203.

Marcowith, A., Ferrand, G., Grech, M., Meliani, Z., Plotnikov, I., and Walder, R. (2020). Multi-scale simulations of particle acceleration in astrophysical systems. *Living Reviews in Computational Astrophysics*, 6(1):1.

Martí, J.-M. (2019). Numerical Simulations of Jets from Active Galactic Nuclei. *Galaxies*, 7(1):24.

McKinney, J. C. (2006). General relativistic magnetohydrodynamic simulations of the jet formation and large-scale propagation from black hole accretion systems. *Monthly Notices of the Royal Astronomical Society*, 368(4):1561–1582.

McKinney, J. C. and Narayan, R. (2007). Disc-jet coupling in black hole accretion systems - I. General relativistic magnetohydrodynamical models. *Monthly Notices of the Royal Astronomical Society*, 375(2):513–530.

Medina-Torrejón, T. E., de Gouveia Dal Pino, E. M., and Kowal, G. (2023). Particle Acceleration by Magnetic Reconnection in Relativistic Jets: The Transition from Small to Large Scales. *The Astrophysical Journal*, 952(2):168.

Meliani, Z. and Keppens, R. (2009). Decelerating Relativistic Two-Component Jets. *Astrophysical Journal*, 705(2):1594–1606.

Melzani, M. (2014). *Collisionless magnetic reconnection in relativistic plasmas with particle-in-cell simulations*. Theses, Ecole normale supérieure de lyon - ENS LYON.

Mertens, F., Lobanov, A., Walker, R., and Hardee, P. (2016). Kinematics of the jet in M 87 on scales of 100–1000 schwarzschild radii. *Astronomy & Astrophysics*, 595:A54.

Micono, M., Zurlo, N., Massaglia, S., Ferrari, A., and Melrose, D. B. (1999). Diffusive shock acceleration in extragalactic jets.

Mirabel, I. F. (2003). Microquasars as Sources of High Energy Phenomena. In Li, X. D., Trimble, V., and Wang, Z. R., editors, *High Energy Processes and Phenomena in Astrophysics*, volume 214, page 201.

Mizuno, Y., Hardee, P. E., and Nishikawa, K.-I. (2014). Spatial Growth of the Current-driven Instability in Relativistic Jets. *The Astrophysical Journal*, 784(2):167.

Nagai, H., Haga, T., Giovannini, G., Doi, A., Orienti, M., D'Ammando, F., Kino, M., Nakamura, M., Asada, K., Hada, K., and Giroletti, M. (2014). Limb-brightened Jet of 3C 84 Revealed by the 43 GHz Very-Long-Baseline-Array Observation. *Astrophysical Journal*, 785(1):53.

Nalewajko, K. (2009). Polarization of synchrotron emission from relativistic reconfinement shocks. *Monthly Notices of the Royal Astronomical Society*, 395(1):524–530.

Nalewajko, K., Yuan, Y., and Chruliska, M. (2018). Kinetic simulations of relativistic magnetic reconnection with synchrotron and inverse compton cooling. *Journal of Plasma Physics*, 84(3):755840301.

Nishikawa, K. I., Hardee, P. E., Duţan, I., Niemiec, J., Medvedev, M., Mizuno, Y., Meli, A., Sol, H., Zhang, B., Pohl, M., and Hartmann, D. H. (2014). Magnetic Field Generation in Core-sheath Jets via the Kinetic Kelvin-Helmholtz Instability. *The Astrophysical Journal*, 793(1):60.

Ostrowski, M. (1990). Diffusive acceleration of cosmic ray particles at tangential discontinuity of velocity field. *Astronomy and Astrophysics (ISSN 0004-6361), vol. 238, no. 1-2, Nov. 1990, p. 435-438.*, 238:435–438.

Ostrowski, M. (1998). Acceleration of ultra-high energy cosmic ray particles in relativistic jets in extragalactic radio sources. *A & A*, 335:134–144.

Padovani, P. (2017). Active galactic nuclei at all wavelengths and from all angles. *Frontiers in Astronomy and Space Sciences*, 4.

Parker, E. N. (1957). Sweet's Mechanism for Merging Magnetic Fields in Conducting Fluids. *Journal of Geophysical Research*, 62(4):509–520.

Penn, G., Stoltz, P. H., Cary, J. R., and Wurtele, J. (2003). Boris push with spatial stepping. *Journal of Physics G: Nuclear and Particle Physics*, 29(8):1719.

Perlman, E., Sparks, W., Biretta, J., Macchetto, D., and Leahy, J. P. (2001). Optical structure and physics of the m87 jet.

Petschek, H. E. (1964). Magnetic Field Annihilation. In *NASA Special Publication*, volume 50, page 425.

Piran, T. (2000). Gamma-ray bursts a puzzle being resolved. *Physics Reports*, 333-334:529553.

Reber, G. (1940). Notes: Cosmic Static. *The Astrophysical Journal*, 91:621–624.

Rees, M. J. (1966). Appearance of Relativistically Expanding Radio Sources. *Nature*, 211(5048):468–470.

Rieger, F. M. (2019). An introduction to particle acceleration in shearing flows. *Galaxies*, 7(3).

Rieger, F. M., Bosch-Ramon, V., and Duffy, P. (2007). Fermi acceleration in astrophysical jets. *Astrophysics and Space Science*, 309(1-4):119–125.

Rieger, F. M. and Duffy, P. (2004). Shear Acceleration in Relativistic Astrophysical Jets. *The Astrophysical Journal*, 617(1):155–161.

Rieger, F. M. and Duffy, P. (2005). Particle Acceleration in Astrophysical Shear Flows. *Chinese Journal of Astronomy and Astrophysics Supplement*, 5:195–200.

Rieger, F. M. and Duffy, P. (2006). Cosmic particle acceleration in astrophysical shear flows. *Proceedings of the International Astronomical Union*, 2(14):103103.

Rieger, F. M. and Duffy, P. (2006). Cosmic particle acceleration in astrophysical shear flows. In *IAU Joint Discussion*, volume 26 of *IAU Joint Discussion*, page 18.

Romero, G. E., Boettcher, M., Markoff, S., and Tavecchio, F. (2017). Relativistic jets in active galactic nuclei and microquasars. *Space Science Reviews*, 207(1-4):561.

Rybicki, G. B. and Lightman, A. P. (1979). *Radiative processes in astrophysics.*

Sahayanathan, S. (2009). Boundary shear acceleration in the jet of MKN501. *Monthly Notices of the Royal Astronomical Society: Letters*, 398(1):L49–L53.

Seyfert, C. K. (1943). Nuclear Emission in Spiral Nebulae. *The Astrophysical Journal*, 97:28.

Shen, Y. (2013). The mass of quasars. *Bulletin of the Astronomical Society of India*, 41(1):61–115.

Shklovsky, I. S. (1955). Possible Observation of Monochromatic Radioemission from Interstellar Molecules. In *Liege International Astrophysical Colloquia*, volume 6 of *Liege International Astrophysical Colloquia*, pages 675–677.

Sikora, M. and Madejski, G. (2000). On Pair Content and Variability of Subparsec Jets in Quasars. *The Astrophysical Journal*, 534(1):109–113.

Sikora, M., Rutkowski, M., and Begelman, M. C. (2015). A spinesheath model for strong-line blazars. *Monthly Notices of the Royal Astronomical Society*, 457:1352–1358.

Sironi, L. (2022). Nonideal Fields Solve the Injection Problem in Relativistic Reconnection. *prl*, 128(14):145102.

Sironi, L., Petropoulou, M., and Giannios, D. (2015). Relativistic jets shine through shocks or magnetic reconnection? *Monthly Notices of the Royal Astronomical Society*, 450(1):183–191.

Sironi, L., Rowan, M. E., and Narayan, R. (2021). Reconnection-driven particle acceleration in relativistic shear flows. *The Astrophysical Journal Letters*, 907(2):L44.

Sironi, L. and Spitkovsky, A. (2009). Particle acceleration in relativistic magnetized collisionless pair shocks: Dependence of shock acceleration on magnetic obliquity. *The Astrophysical Journal*, 698(2):1523–1549.

Sironi, L. and Spitkovsky, A. (2014). Relativistic Reconnection: An Efficient Source of Non-thermal Particles. *The Astrophysical Journal Letters*, 783(1):L21.

Sol, H., Pelletier, G., and Asso, E. (1989). Two-flow model for extragalactic radio jets. *Monthly Notices of the Royal Astronomical Society*, 237(2):411–429.

Spitkovsky, A. (2005). Simulations of relativistic collisionless shocks: shock structure and particle acceleration. *AIP Conference Proceedings*.

Spitkovsky, A. (2007). On the structure of relativistic collisionless shocks in electron-ion plasmas. *The Astrophysical Journal*, 673(1):L39L42.

Stawarz, . and Ostrowski, M. (2002). High energy radiation generated at boundary shear layers of relativistic jets. *Publications of the Astronomical Society of Australia*, 19(1):2225.

Summerlin, E. J. and Baring, M. G. (2012). Diffusive Acceleration of Particles at Oblique, Relativistic, Magnetohydrodynamic Shocks. *The Astrophysical Journal*, 745(1):63.

Swain, M. R., Bridle, A. H., and Baum, S. A. (1998). Internal Structure of the Jets in 3C 353. *The Astrophysical Journal Letters*, 507(1):L29–L33.

Swain, M. R., Bridle, A. H., and Baum, S. A. (1998). Internal structure of the jets in 3c 353. *The Astrophysical Journal*, 507(1):L29.

Sweet, P. A. (1958). The Neutral Point Theory of Solar Flares. In Lehnert, B., editor, *Electromagnetic Phenomena in Cosmical Physics*, volume 6, page 123.

Trippe, S. (2014). Polarization and Polarimetry: a Review. *Journal of Korean Astronomical Society*, 47(1):15–39.

Vay, J. L., Geddes, C. G. R., Cormier-Michel, E., and Grote, D. P. (2011). Numerical methods for instability mitigation in the modeling of laser wakefield accelerators in a Lorentz-boosted frame. *Journal of Computational Physics*, 230(15):5908–5929.

Villasenor, J. and Buneman, O. (1992). Rigorous charge conservation for local electromagnetic field solvers. *Computer Physics Communications*, 69(2):306–316.

Vlasov, A. A. (1968). Reviews of Topical Problems: the Vibrational Properties of AN Electron Gas. *Soviet Physics Uspekhi*, 10(6):721–733.

Vourellis, C. and Fendt, C. (2021). Relativistic Outflows from a GRMHD Mean-field Disk Dynamo. *The Astrophysical Journal*, 911(2):85.

Wang, J.-S., Reville, B., Mizuno, Y., Rieger, F. M., and Aharonian, F. A. (2023). Particle acceleration in shearing flows: the self-generation of turbulent spine-sheath structures in relativistic magnetohydrodynamic jet simulations. *mnras*, 519(2):1872–1880.

Wardzinski, G. and Zdziarski, A. A. (2000). Thermal synchrotron radiation and its Comptonization in compact X-ray sources. *Monthly Notices of the Royal Astronomical Society*, 314(1):183–198.

Webb, G. M. (1989). The Diffusion Approximation and Transport Theory for Cosmic Rays in Relativistic Flows. *The Astrophysical Journal*, 340:1112.

Webb, G. M., Barghouty, A. F., Hu, Q., and le Roux, J. A. (2018). Particle acceleration due to cosmic-ray viscosity and fluid shear in astrophysical jets. *The Astrophysical Journal*, 855(1):31.

Weibel, E. S. (1959). Spontaneously growing transverse waves in a plasma due to an anisotropic velocity distribution. *Phys. Rev. Lett.*, 2:83–84.

Werner, G. R., Philippov, A. A., and Uzdensky, D. A. (2018a). Particle acceleration in relativistic magnetic reconnection with strong inverse-Compton cooling in pair plasmas. *Monthly Notices of the Royal Astronomical Society: Letters*, 482(1):L60–L64.

Werner, G. R., Philippov, A. A., and Uzdensky, D. A. (2018b). Particle acceleration in relativistic magnetic reconnection with strong inverse-Compton cooling in pair plasmas. *Monthly Notices of the Royal Astronomical Society: Letters*, 482(1):L60–L64.

Woosley, S. E. and Bloom, J. S. (2006). The Supernova Gamma-Ray Burst Connection. *Annual Review of Astronomy and Astrophysics*, 44(1):507–556.

Yang, Y.-P. and Zhang, B. (2018). Synchrotron Radiation from Electrons with a Pitch-angle Distribution. *The Astrophysical Journal Letters*, 864(1):L16.

Yee, K. (1966). Numerical solution of initial boundary value problems involving maxwell's equations in isotropic media. *IEEE Transactions on Antennas and Propagation*, 14(3):302–307.

Zenitani, S., Hesse, M., and Klimas, A. (2010). Resistive Magnetohydrodynamic Simulations of Relativistic Magnetic Reconnection. *The Astrophysical Journal Letters*, 716(2):L214–L218.

Zenitani, S. and Hoshino, M. (2001). The generation of nonthermal particles in the relativistic magnetic reconnection of pair plasmas. *The Astrophysical Journal*, 562(1):L63.

Zhang, W., MacFadyen, A., and Wang, P. (2009). Three-Dimensional Relativistic Magnetohydrodynamic Simulations of the Kelvin-Helmholtz Instability: Magnetic Field Amplification by a Turbulent Dynamo. *The Astrophysical Journal Letters*, 692(1):L40–L44.